Long-term water balance of a combined capillary barrier-methane oxidising landfill cover system

Long-term water balance of a combined capillary barrier-methane oxidising landfill cover system

By

J.M. van den Brink

in partial fulfilment of the requirements for the degree of

Master of Science
in Civil Engineering

at the Delft University of Technology,
to be defended publicly on September 27th, 2023.

Supervisor:	Dr. habil. J. Gebert	TU Delft, Geo-Engineering
Thesis committee:	Prof. Dr. Ir. T.J. Heimovaara	TU Delft, Geo-Engineering
	Dr. habil. Markus Hrachowitz	TU Delft, Water Resources
	Ir. H. Scharff	N.V. Afvalzorg Holding

Acknowledgements

If there is one thing that I have learned about environmental engineering, it is that our environment is always more complex than you think. Or, in the words of my supervisor Julia: *"We can fly to the moon, but accurately measuring rainfall on the other hand…"* This statement is not meant to trivialise the numerous scientific advancement in this field, it is quite the reverse: I am grateful for all that I have learned to understand in the past years and especially during this master thesis.

I have had the privilege to work on this thesis from my home in the forest of Zeist most of the time, where there is ample opportunity to observe everything I learned about (soil) hydrology in the field. That was the place where I worked my way through fist-thick German soil excavation reports that I received from Heijo during his warm welcome at Afvalzorg, or the other information that he would send me almost before I could ask for it. It was there, where I broke my head about confusing precipitation and outflow measurements while remembering wise and encouraging words from Markus about the difficulties of being a hydrologist. It was at that desk where at one moment I would wonder if I would ever get my model working and in the next would be surprised by the many new insights that Timo had provided me with. It was at a different desk somewhere at the faculty of Geo-engineering where Julia would take the time to discuss the many different and sometimes frustrating results that emerged over time. Moreover, it was in a warm lecture room and also on a windy and cold landfill where she sparked my interest in soil and waste, initially.

While sitting or standing behind all those different desks, I could always count on the support of my family and friends. I would remember that best when sitting behind a more comfortable dining table in Zeist, Utrecht, Hoofddorp, Enschede or Delft. Especially the one in Zeist would often offer much joy and relief, as I could always find Lisa there, sharing another joke and willingly listening to exciting stories of new discoveries or the tragedies of finding another dead end. This thesis period coincided with our first year as a married couple and I hope we continue to live happily ever after.

The end of this thesis also marks the end of my time being a full-time student. Although I do not know what new kind of desks lie ahead, I hope they will remain places of wonder and exploration of the fascinating world around us.

List of abbreviations

AEV	Air entry value
CARS	Centraal Alarmering en Registratie Systeem; data monitoring computer on site.
CB	Capillary block
CBE	Capillary barrier effect
CBS	Capillary barrier system, consisting of a CL and a CB
CL	Capillary layer
GDL	Gas distribution layer
GSD	Grain size distribution
KNMI	Koninklijk Nederlands Meteorologisch Instituut; Dutch national weather service
LFG	Landfill gas
MMOS	Microbial methane oxidation system
MOL	Methane oxidation layer
PSD	Pore size distribution
SWRC	Soil water retention curve
SHCC	Soil hydraulic conductivity curve
SS	Subsoil
TS	Topsoil
VG	Van Genuchten
WEV	Water entry value

Equation characters in **bold** denote vectors.

Table of Contents

Abstract

Capillary barrier systems (CBSs) have been demonstrated to be effective in deviating infiltration in a landfill cover. However, their performance when combined with a cover soil optimised for methane oxidation had not been tested in the field yet. This study aimed to describe the water balance of a test field where such a configuration was built, located on the landfill in the Wieringermeer area, the Netherlands, over the period from 2009 to 2023.

During that time period breakthrough and deviated infiltration were measured. A one-dimensional finite difference model was built to model evapotranspiration and storage in the cover soil as well as the moisture retaining layer (capillary layer; CL). This model performed well in describing overall seasonal trends but generally overestimated evapotranspiration in spring and outflow in autumn, consequently underestimating the storage in these seasons.

The results show that the annual precipitation ranges between 770 and 990 mm. On average, 59% (494 mm) of this precipitation is evaporated, 33% (281 mm) is diverted by the CBS and 7% (63 mm) breaks through. Compared to other test fields and design standards, this breakthrough is high. A weakened functioning of the CBS by construction errors or the ingress of sand could be a reason for that. Another factor might be the coarse grain size distribution of cover soil, necessary for the efficient oxidation of methane. This type of soil has a relatively high hydraulic conductivity which does not control infiltration rates into the CBS as well as cover soils in other studies.

Furthermore, the results suggest that storage in the cover soil and CL is the main determinant for breakthrough to occur. Major breakthrough only occurred at a storage larger than the storage in the soil associated with field capacity, both on a seasonal and daily time scale. The available storage is mainly affected by the evapotranspiration which shows a seasonal cycle. Consequently, outflows for the CL and breakthrough occur mostly when evapotranspiration is low (autumn, winter). The relation of breakthrough with precipitation is less straightforward as a high rainfall does not necessarily lead to breakthrough on a seasonal or daily scale, depending on the available storage in the system. The distribution of precipitation can matter however. On a seasonal scale, precipitation in late summer can result in high storage in the beginning of autumn, potentially leading to breakthrough. Furthermore, a precipitation amount uniformly distributed over a day leads to less breakthrough than more concentrated precipitation.

Overall, with some adjustments regarding the design of the CBS and the cover soil, this landfill cover design is a promising alternative for the current standard.

1. Introduction

In the Netherlands, just as in the rest of the European Union, the landfilling of waste is the least preferred option in the treatment of solid waste. Among other reasons, it can result in hazardous emissions to the groundwater and the atmosphere (Council Directive 1999/31/EC on the Landfill of Waste, 1999). To prevent those, the current Dutch standards prescribe that landfills should be completely isolated from its environment (Stortbesluit Bodembescherming, 1993).

One of the components of the isolation infrastructure of a landfill is the surface sealing. The purpose of this sealing is to limit landfill gas emissions and prevent infiltration of precipitation. Landfill gas contains high concentrations of methane which is a strong greenhouse gas. Moreover, percolating rain water, called leachate, mobilises contaminants which endangers the groundwater quality. Even when a bottom sealing is constructed to prevent leachate from leaving the landfill, its quality deteriorates over time. On top of that, a bottom sealing cannot be accessed and maintained after construction of the landfill, which makes a surface sealing necessary (Ministerie van VROM, 1991).

The current design of such a surface sealing, also called landfill cover system, consists of liner system and a cover soil (Figure 1). The cover soil primarily facilitates the growth of vegetation. The liner system on the other hand isolates the waste body from the environment. It consists of a synthetic and a mineral component. These are usually implemented as a High Density Polyethylene (HDPE) foil and a sand-bentonite mixture, respectively (Uitvoeringsregeling Stortbesluit Bodembescherming, 1993).

Maintaining complete isolation for a long time, however, proves difficult (Johnson & Panders, 2003). For example, the HDPE foil deteriorates over time and needs to be periodically replaced. The high costs of such an operation combined with the (theoretically) eternally lasting aftercare of a landfill result in high financial risks for the landfill operator (Brand et al., 2016).

This stimulates the search for an alternative and more durable liner system. One of the alternatives is a so-called capillary barrier system (CBS). In this study this liner system is combined with a cover soil where the methane in the landfill gas is biologically oxidised.

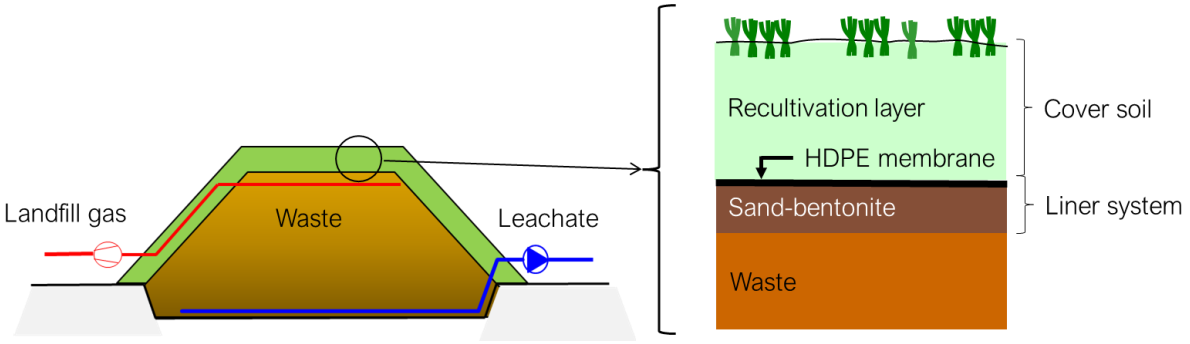

Figure 1: Left: Schematisation of a landfill where leachate and landfill gas are collected. Right: Simplification of the current design of a landfill cover system or surface sealing, consisting of a cover soil and a liner system. For simplicity the drainage layer on top of the liner system and the foundation layer were left out.

1.1. Capillary barriers

Capillary barrier systems (CBS) have been studied extensively in the last 30 years. This system is a combination of a relatively fine soil on top of a relatively coarse soil layer. The fine and coarse soil layers are called the capillary layer (CL) and the capillary block (CB), respectively. It can limit infiltration into the waste because of a difference in capillary forces between the two layers which are much stronger in the CL than in the CB material. Consequently, the moisture retention in the CL is higher than in the CB. Under unsaturated conditions this results in a much higher hydraulic conductivity in the CL as compared to the CB. When built on a slope, the water is diverted downslope under the influence of gravity instead of percolating into the CB. Hence it does not enter the waste body but can be collected separately. This capillary barrier effect (CBE) exists only up to a certain water content of the CL. Any additional water will lead to water entering the CB and the waste, which is called breakthrough. The maximum flow through the CL is defined as the diversion capacity of a CBS and the maximum length before breakthrough occurs the diversion length (Figure 2).

Since the 1970s, CBSs have been studied in many different climates and configurations, with different methods and for a range of purposes. The term 'capillary barrier' was coined by a French engineer D. Rançon (1972) in the context of sealing radioactive waste disposals. Between 1980 and 1990 the concept became more widely known and was studied in France, Denmark, Germany, Canada and the USA, where its potential as liner system for landfills and as oxygen barrier for mine waste heaps to prevent the formation of acid was assessed (Steinert, 1999; Zornberg et al., 2010). Also, during this period the concept of a CBS was already applied on landfill covers of three landfills in Switzerland (Steinert, 1999).

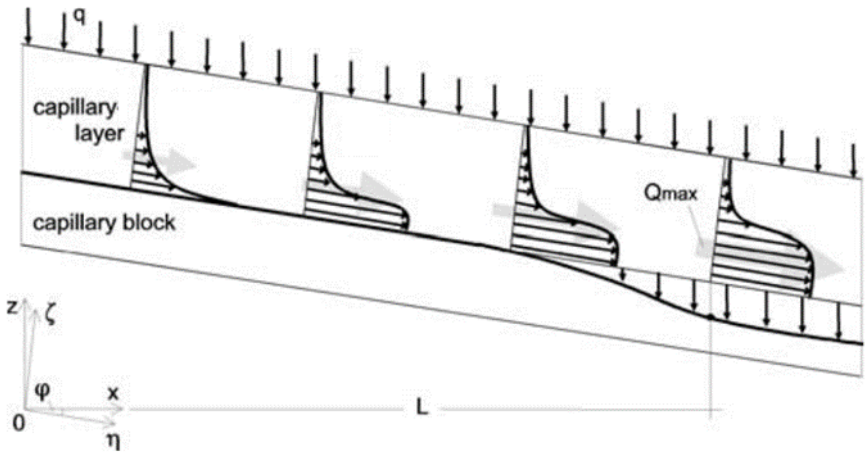

Figure 2: Principle of a capillary barrier system (CBS) with the relatively fine-grained capillary layer (CL), the relatively coarse grained capillary block (CB), ϕ the inclination angle, q the infiltration, Q_{max} the diversion capacity and L the diversion length. Figure adopted from Kämpf et al. (2003).

In 1990, Ross (1990) formulated an analytical equation to calculate the lateral drainage capacity and the diversion length of a capillary barrier. His equations were an important step for understanding and designing CBSs and were further generalized by Steenhuis et al. (1991).

Until 2000 the main research activities on CBS remained located in Germany, Canada and the USA (Melchior et al., 2010; Nyhan et al., 1990; Steinert, 1999; Stormont, 1996; Yanful, 1993). From 2004 onwards, CBSs were also tested under tropical conditions in Singapore and some years later also in the south of China (Rahardjo et al., 2013; Tami et al., 2004; Zhan et al., 2014). The concept was originally studied for its potential to seal landfills but was later also applied for slope stabilisation. In this context the latest research has been performed in Scotland (Scarfone et al., 2023).

The climates in all these studies where CBS were applied differ greatly. The studies in the USA were done in a semi-arid climate. Under these conditions CBSs showed very good performance because most of the precipitation can be retained and evaporated (Khire et al., 1999, 2000; Scarfone et al., 2023). In regions with more precipitation and low evaporation like the cold climate in Canada (Quebec) or the temperate climate in Germany, lateral drainage is more important for the performance of a CBS (Abdolahzadeh et al., 2011b; Kämpf & Montenegro, 1997). In tropical climates, the challenge for CBS is to store and divert high amounts of precipitation (Rahardjo et al., 2012; Zhan et al., 2014).

The behaviour of a CBS has been investigated using three different methodologies: physical experiments in a laboratory (e.g. Kämpf et al., 2003; Steinert, 1999; Stormont, 1996; Stormont & Anderson, 1999; Yang et al., 2004), experiments using a numerical model (e.g. Aubertin et al., 2009; Berger, 2018; Ho & Webb, 1998; Khire et al., 2000; Oldenburg & Pruess, 1993; Scarfone et al., 2023; Vachon et al., 2015) and field studies using test fields (e.g. Abdolahzadeh et al., 2011a; Giurgea et al., 2003; Kämpf & Montenegro, 1997; Khire et al., 1999; Melchior et al., 2010; Rahardjo et al., 2012).

The focus of the laboratory and numerical modelling studies was mainly to identify the flow processes and important design parameters of a CBS. These studies have stressed, among other major determinants (Section 2.2.2), the importance of the seepage into and the antecedent moisture of the CBS for its diversion length (Aubertin et al., 2009; Berger, 2018; Kämpf et al., 2003; Khire et al., 2000; Stormont, 1996).

However, field tests were needed to test the CBS performance in practice in conditions with no control over the precipitation input. Also, hydraulic properties of the materials used for the cover soil on top of the CBS might also change over time due to for example settlement (Abdolahzadeh et al., 2011a) or soil cracking (Giurgea et al., 2003). The studies that tested a CBS in the field showed a performance of the CBS that can comply with local liner system regulations (Abdolahzadeh et al., 2011b; Giurgea et al., 2003; Kämpf & Montenegro, 1997; Melchior et al., 2010). Most of these studies performed measurements up to a few years. One study measured for 9 years (Giurgea et al., 2003) and another for 18 years (Melchior et al., 2010). Long-term measurements are valuable because the systems response to a larger range of hydrological conditions and any change in the system can be observed.

1.2. Methane oxidation

Besides potential emissions to the groundwater, landfills can also be a major source of greenhouse gas emissions. Due to anaerobic degradation of organic matter in the landfill, landfill gas (LFG) is produced. This gas consists of approximately 60% methane (CH_4) and 40%

carbon dioxide (CO_2). Methane, however, is a strong greenhouse gas. The global warming potential of methane, defined as the time-integrated radiative forcing of an emission amount relative to the same emission amount of carbon dioxide, over a period of 100 years is estimated to be 28 (Myhre et al., 2013). Therefore, the collection and treatment of methane is part of operating a landfill in the European Union to reduce emissions (Council Directive 1999/31/EC on the Landfill of Waste, 1999).

One of the options for doing so is to implement a microbial methane oxidation system (MMOS). The principle of MMOS is that naturally present methanotrophic bacteria oxidise methane to less hazardous carbon dioxide. One of the designs in which this idea is implemented is a so-called biocover. This concept is part of the final or interim cover of the landfill where methane can be oxidised over large areas. This technology can be useful and cost-effective on landfills where emissions are relatively low or active gas extraction and treatment is no longer economically or technically viable. Alternatively, it can also be used as complementary measure to active gas extraction (Gebert et al., 2022; Scheutz et al., 2009).

A biocover consists of at least two layers: a gas distribution layer (GDL) below and a methane oxidation layer (MOL) on top (Figure 3). Landfill gas leaves the waste in certain hotspots due to the waste's heterogeneity. The GDL has the principal purpose to distribute this landfill gas evenly to the overlying MOL to prevent overloading. Furthermore, among others, the MOL needs to permit advective and diffusive transport of landfill gas upwards and the downward diffusion of oxygen. It should also offer a suitable living environment for the methanotrophs by providing adequate moisture and nutrients. Material selection should also observe the requirement of methanotrophic bacteria on, for example, pH and salinity. (Gebert et al., 2022).

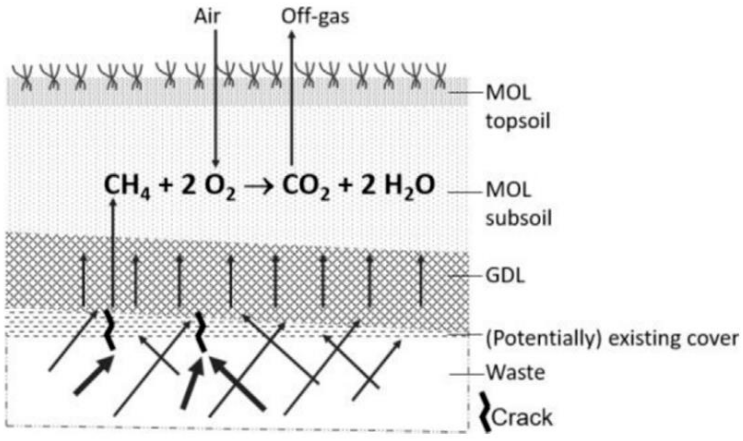

Figure 3: Basic design of a methane oxidising biocover: the gas distribution layer (GDL) lies on top of the waste. The methane oxidation layer (MOL) can be divided into a topsoil and a subsoil. Figure adopted from Gebert et al. (2022)

1.3. Problem description

In 2009 N.V. Afvalzorg Holding (Afvalzorg) started the construction of a two test fields at the landfill in the Wieringermeer. One test field contained a CBS and the other a stormwater drainage mat as liner system to divert infiltrating precipitation. Both liner systems were covered with a soil optimised for methane oxidation. The purpose of these test fields was to

investigate the performance of these systems in diverting infiltrating precipitation and oxidation of methane. This study focuses on the field containing the CBS, where the CB of the CBS served as GDL simultaneously. In this way the two functionalities of minimising infiltration of precipitation and minimising methane emissions to the atmosphere were combined (Melchior+Wittpohl, 2011).

The performance of this cover system concerning methane oxidation has been extensively investigated. One of the main findings was that there is a potential conflict between the diversion of infiltration in the CBS and the uniform distribution of LFG in the CB (Geck et al., 2016; Röwer et al., 2016).

When pores become filled with water, air flow is progressively restricted. In general, the gas diffusivity of a soil decreases linearly with decreasing air-filled porosity caused by, for example, an increasing water content. The gas conductivity on the other hand shows an exponential decrease and on top of that there is a certain water content where it suddenly drops sharply. At this water content the network of interconnected pores available for advective gas transport is obstructed by moisture (Gebert et al., 2022; van Verseveld & Gebert, 2020; Wawra & Holfelder, 2003).

Therefore, as moisture accumulates downslope in the CL due to the CBE, gas flow from the GDL to the MOL is obstructed progressively. This induces upslope gas migration resulting in a higher methane load upslope. Depending on the methane oxidation capacity of the MOL this area could be overloaded leading to the emission of methane (Ahoughalandari et al., 2018; Geck et al., 2016). The study of Röwer et al. (2016) showed that, based on the calculated up- and downslope gradient in gas conductivity, upslope emissions could be 10% higher than downslope.

Hence, more insight is needed into the water transport and retention in the test field. In other words, the water balance of the test field should be quantified. The water balance is based on the principle of mass conservation and states that the inflow of water should be equal to the outflow plus the change in storage in a system. In case of the test field , the main inflow is precipitation and the main outflows are evapotranspiration and discharge from the CBS. Additionally, there is storage of water in the soil.

1.4. Research aim

This study aims to quantify the water balance of the test field containing a CBS at the Wieringermeer landfill. The principal goal with this is to assess the performance of the CBS under different hydrological conditions. Precipitation and outflows have been measured since 2009, comprising a valuable dataset including a wide range of local climatic conditions and hence of the hydraulic load to the CBS. Moreover, this study could form the basis for further research on the consequences of the water retention for the distribution of LFG. So, the main question of this study is:

- How is the water balance of the test field at the Wieringermeer landfill composed between 2009 and 2023?

This main question can be divided in two subquestions:

1. How is the water balance composed on an annual and seasonal time scale?
2. What are the hydrological boundary conditions that lead to a breakthrough event?

The hydrological boundary conditions in the second subquestion imply the magnitude of the different components of the water balance that lead to breakthrough. These will be analysed on a seasonal and daily time scale.

To arrive to answers to these questions, this study analysed the measurements made between October 2009 and June 2023. The components missing from the water balance (evapotranspiration and storage) were modelled using a one dimensional simulation. Although gas- and water flow through the unsaturated zone are strongly coupled, this research considers only water flow and retention.

Internationally, this research can add to the knowledge of CBSs because it yields a long timeseries of measurements on a CBS configuration which has not been tested in the field yet. Similar long-term studies on a CBS in a comparable climate were performed by Melchior et al. (2010) and Giurgea et al. (2003), but both studies used CBS configurations with a different type of cover soil.

1.5. Report structure

This report has the following structure: First the background of water flow in unsaturated soils and in particular in capillary barriers will be explained (Chapter 2). The next chapter presents more information of the test field. Chapter 4 describes the processing of the measurements and the setup of the model for estimating evaporation and soil water storage. Chapter 5 shows the results, after which they will be discussed in Chapter 6. The conclusion and recommendations are given in Chapter 7 and 8.

2. Theoretical background: CBS water storage and flow

Defining the water balance of a test field containing a CBS requires understanding of the storage and flow of unsaturated water in such a system as both outflow and evapotranspiration depend on it. Therefore, this chapter will first establish the basic physical definitions of soil water storage and unsaturated flow. Secondly, the flow of water through a CBS is described using these mechanisms.

2.1. Soil water flow and storage[1]

Soil water potential is a crucial concept for describing the storage and flow of moisture in an unsaturated soil. It is the thermodynamic state of water in the soil compared to a reference state of free water (water without influences of other substances). In soil science, this potential is commonly expressed as energy per unit volume, or pressure (Pa). For consistency, this study expresses potential as energy per unit weight, or head (m). These two units are related by Equation 1.

$$p = \rho_w g h \qquad \text{Equation 1}$$

With p the soil water potential in units of pressure [Pa], ρ_w the density of water [kg m^{-3}], g the gravitational acceleration [9.81 m s^{-2}] and h the soil water potential in units of head [m].

The soil water potential is the sum of many components which are explained in more detail in Appendix A.1. The components considered in this study are only the gravimetric- and suction head:

$$h_t = h_z + h_m \qquad \text{Equation 2}$$

With h_t, h_z and h_m the total, gravimetric and suction head, respectively [m]. The latter is the result of adhesive and capillary forces exerted by the soil matrix on the soil water. As this is a binding force, suction head is commonly defined negatively. However, to avoid confusion and remain consistent, the absolute value is used in the remainder of this thesis. For example, when stated *'increasing suction head'*, it is meant that the suction head becomes more negative.

Capillary forces are the most dominant mechanism contributing to the suction head relevant for explaining water storage and flow in a CBS. When modelling the pores in a soil as tubes with an effective radius r_e, the capillary force can be calculated using the Young-Laplace equation:

$$h_m = \frac{2T_s \cos\alpha}{r_e \rho_w g} \qquad \text{Equation 3}$$

With h_m the suction head, or height of capillary rise [m], T_s the surface tension of the air-water interface [N/m], α the contact angle between the tube and the water surface and r_e the effective pore size. A more detailed explanation of soil water potential and capillarity is given in Appendix A.1.

[1] The theory in this section comes from Blume et al. (2016, Chapter 6.4) and Lu & Likos (2004, Chapters 1–5, 8, 9 and 12).

2.1.1. Soil water retention curve

Soils typically have a range of pores which is defined as their pore size distribution (PSD). These different pore sizes enact a range of capillary forces. Accordingly, the water content in a soil varies with the suction head of the water in a soil. This relationship is defined as the soil water retention curve (SWRC) of which an example of the CBS in this study is shown in Figure 4. The volumetric water content is defined as:

$$\theta_w = \frac{V_w}{V_t} \qquad \text{Equation 4}$$

With θ_w the volumetric water content [$cm^3\ cm^{-3}$], V_w the volume of water [cm^3] and V_t the total volume of the soil [cm^3]. It is also possible to use the effective saturation for the definition of the SWRC of a soil. This is a dimensionless measure of the water content relative to the soils' residual and saturation water content (van Genuchten, 1980):

$$S_e = \frac{\theta_w - \theta_r}{\theta_s - \theta_r} \qquad \text{Equation 5}$$

With S_e the effective saturation [-], θ_r the residual water content [m^3m^{-3}] and θ_s the saturation water content [m^3m^{-3}].

Two important suction head levels are the air-entry value (AEV) and the water-entry value (WEV). The first is defined as the suction head at which desaturation starts. Just before that point, the soil is saturated and has a volumetric water content defined as the saturated water content (θ_s). Conversely, the WEV is the matric head at which water starts to enter a completely dry soil (Baker & Hillel, 1990). Furthermore, the residual water content (θ_r) can be defined as the volumetric water content at permanent wilting point (PWP) at a suction head of approximately 15,000 cm , which is theoretically the maximum suction head plant roots can exert on the soil water. Lastly, the field capacity of a soil (FC) is defined as the water content at (approximate) hydraulic equilibrium after prolonged precipitation. Depending on the equilibrium conditions the suction head of this situation lies between 60 and 300 cm, but can be 30 cm for a sandy soil as well. This study uses the lower boundary suction head of 300 cm.

The shape of the SWRC depends on the PSD which depends on the grain size distribution (GSD) and the bulk density of a soil. As shown in Figure 4, a coarse soil like the gravel of the CB has a low AEV and drains over a smaller range of suction head. Conversely, a soil with smaller pores like the sand in the CL has a higher AEV and drains over a larger range of suction.

Additionally, soil hysteresis causes the SWRC to be resisting the direction of change in water content. In other words, if the soil is drying it contains more water than a wetting soil at the same suction as a wetting. More explanation of this phenomenon is given in Appendix A.2.

2.1.2. Soil hydraulic conductivity curve

The hydraulic conductivity of a soil depends on both the properties of the fluid (density and viscosity) and of the soil matrix (e.g. porosity, pore diameter and pore geometry). Similar to the SWRC, it is also dependent on the water content in a soil. With decreasing saturation, the amount of pores available for water transport decreases as well, starting in the largest pores. As the hydraulic conductivity is proportional to the square of the diameter of the pores, it declines fast when desaturating (Figure 4). Mathematically, the soil hydraulic conductivity

curve (SHCC) is often expressed as the saturated hydraulic conductivity multiplied by the relative hydraulic conductivity which is a function of the suction head:

$$k = k_s k_r(h_m) \qquad \text{Equation 6}$$

With k_s the saturated hydraulic conductivity [m s^{-1}] and k_r the relative hydraulic conductivity ranging between 0 and 1.

Similar to the SWRC, the SHCC is also subject to soil hysteresis. Generally, because the water content is higher for a drying soil than for a wetting soil at the same suction head, its relative hydraulic conductivity is also higher.

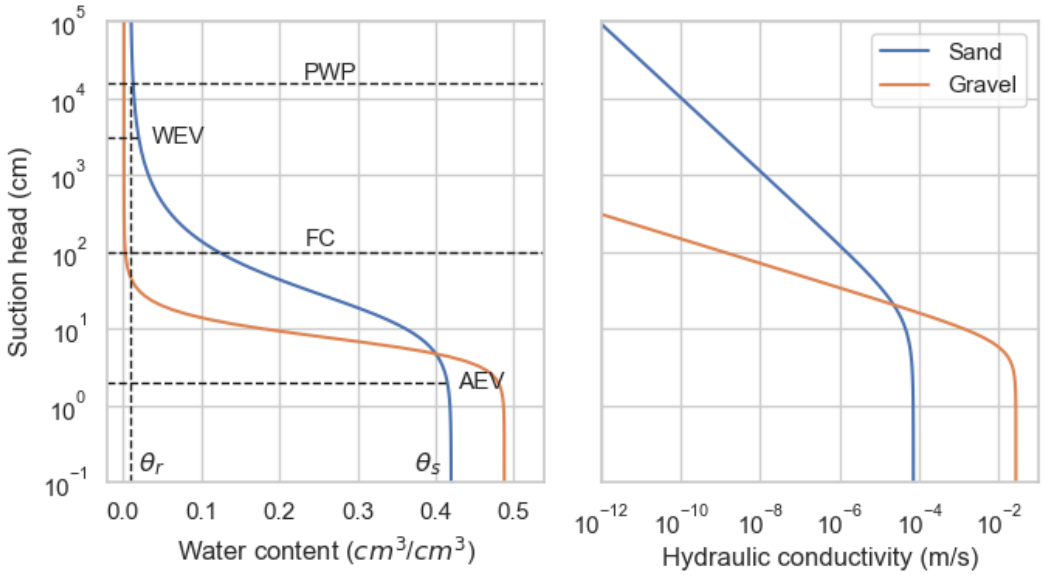

Figure 4: Fitted SWRC and SHCC of the sand and a gravel used for the CL and CB of the test field, respectively. A suction head of 100 cm is used here for the field capacity (FC) as an example but can range betweeen 30-300 cm.

2.2. Water flow in capillary barriers

2.2.1. The capillary barrier effect

Building upon the explanation by Anderson & Madsen (1983), who were among the first researchers on CBSs, Lu & Likos (2004, Chapter 8.4) explain the capillary barrier effect (CBE) using a conceptual model of a tube. A full explanation can be found in Appendix A.3, but in short, breakthrough happens at the moment when the buildup of hydraulic head is more than the difference between the suction head (Equation 3) exerted by the pores of the fine and coarse layer.

A second explanation of the CBE, which is most common in literature, involves the SWRC and the SWCC of the CB and CL (Figure 4). Continuity enforces that the pressure head at the interface between the CL and the CB is equal. In the case of infiltration entering a soil which has a uniform suction head of 10^2 cm for example, the suction head at the interface decreases. Consequently, the water content in the CL increases as well, while the water content in the CB remains virtually the same. The water content in the CB will only start to increase when the suction head has reached the WEV. At that point the capillary forces of the CB are similar to that of the CL and water starts to enter the CB. That point is called breakthrough. In this example the CL is almost at saturation at that point (Khire et al., 1999).

Alternatively, we could explain the same concept using the SHCC. In the same situation of a wetting soil, the hydraulic conductivity of the CB is negligible in the case of suction heads higher than its WEV. The order of magnitude of the difference between the hydraulic conductivity of the CL and the CB can be up to 10^5. Therefore, the CB essentially serves as an impermeable layer, preventing water to flow downwards. As water accumulates in the CL, the suction head decreases until the WEV of the CB is reached. At this point of breakthrough, water starts to enter the CB, increasing its hydraulic conductivity even more, promoting downward water flow (Aubertin et al., 2009; Rahardjo et al., 2016).

2.2.2. Tilted capillary barrier system

In a tilted CBS the accumulated the water above the capillary break starts to flow downslope under the influence of gravity as shown in Figure 2. This lateral flow increases along the slope as more infiltration accumulates, until the suction head decreases to the WEV of the CB and breakthrough occurs. The horizontal length from the top of the slope to the point of breakthrough is called the diversion length (L). The flow in the CL at the point of breakthrough is called the diversion capacity (Q_{max}), which is equal to the infiltration rate multiplied by the diversion length (Aubertin et al., 2009; Lu & Likos, 2004).

Although breakthrough is shown as a uniform flow in Figure 2, in reality breakthrough happens as preferential or fingered flow (Kämpf et al., 2003) which might be induced by soil heterogeneities (Ho & Webb, 1998). Also, breakthrough doesn't happen at a single point but over a zone (Aubertin et al., 2009). Moreover, when breakthrough happens it increases the suction head in the CL again leading to a temporary recovery of the CBE (Ho & Webb, 1998; Kämpf et al., 2003; Stormont, 1996; Stormont & Anderson, 1999). Breakthrough is thus a non-steady and uniform flow.

Figure 2 also shows the flow profile in the CL. This profile is related to the SWRC of the CL. Stormont (1998) found that the pressure at the bottom of the CL is approximately equal to the WEV of the CB and that the suction head profile is approximately a unit gradient when infiltration is relatively low. Consequently, the hydraulic conductivity will be highest at the bottom of the CL. Accordingly, most CL flow happens in an almost saturated fringe just above the capillary break (Kämpf et al., 2003; Stormont, 1996).

In contrast to arid regions where moisture in the CL or overlying layers is removed by high evapotranspiration, the main means to remove water from the CL in humid climate with low evapotranspiration is lateral drainage (Khire et al., 1999). Important design parameters for the drainage capacity of a CBS are the difference between the WEV of the CL and CB, the absolute WEV of the CB and the (un)saturated permeability of the CL (Abdolahzadeh et al., 2011a; Kämpf et al., 2003; Khire et al., 2000; Rahardjo et al., 2013, 2016; Steinert, 1999; Stormont & Anderson, 1999; Yang et al., 2004). Other important parameters are the slope of the system (Abdolahzadeh et al., 2011a; Aubertin et al., 2009; Berger, 2018; Bussière et al., 2003; Steinert, 1999), the thickness of the CL (Abdolahzadeh et al., 2011a; Aubertin et al., 2009; Khire et al., 2000; Steinert, 1999) and the infiltration rate into the CL and its antecedent soil moisture (Aubertin et al., 2009; Berger, 2018; Khire et al., 2000; Stormont, 1996).

3. Field experimental site

This chapter presents the test field that was constructed on the Wieringermeer landfill. The first section covers its design and measurement setup. The second section presents the soil properties of the different soil layers over time.

3.1. Test field design

In the summer of 2009 the construction of the test field at the Wieringermeer landfill took place, contracted by Afvalzorg. The planning, design and control measurements were carried out by the company Melchior + Wittpohl Beratende Ingenieure PartmbB stationed in Hamburg. The goal was to construct a landfill cover system where a CBS and a MOL were combined.

3.1.1. Layout and construction

The location of the landfill and a top view of the test field are shown in Figure 5. A cross section of the soil is shown in Figure 6 and the full construction plan cross section is presented in Appendix B.3. The cover system consisted of four layers: a topsoil (TS), a subsoil (SS) a capillary layer (CL) and a capillary block (CB). A buffer zone with identical soil layering was constructed around area of the test field. Some photos of the construction can be found in Appendix B.1.

The field was constructed using a long reach excavator to prevent high compaction of the soils of the MOL. This was necessary to satisfy requirements for the permeability of the MOL for gas flow as compaction would lead to a decrease in effective permeability of a soil (van Verseveld & Gebert, 2020).

To investigate the influence of the construction method on the soil properties and the resulting effect on the gas distribution patterns, the top 60 cm of the soil was excavated and redistributed in 2013. This time a bulldozer was used for the distribution of the soil after which the soil was loosened again with spades behind a tractor (Appendix B.2). The compaction of the soil increased and the proportion of pores that drain under gravity was decreased (Melchior+Wittpohl, 2014a). This led to a more uniform landfill gas distribution as was observed by Geck et al. (2016).

3.1.2. Measurement setup

Three different water fluxes were measured at the test field: precipitation and outflow from the CL and CB. Additionally, there is also a weather station measuring atmospheric pressure, temperature and relative humidity. Photos of the devices are shown in Appendix B.4. A flowchart describing the registration and data storage process is given in Appendix B.5. A list of all available timeseries is given in Table 1.

The precipitation was measured by three devices: an automatic rain gauge (Pluvio-2) measuring at 5 min interval, and two manual rain gauges (Hellmann) at two heights: ground level and 1 meter height.

The outflow from the CL and CB flows through a tipping bucket into an IBM tank which is drained by a pump. The amount of switches of both the tipping buckets and the

pumps are registered on hourly basis. The volumes of the tipping buckets were measured approximately monthly.

Additionally, water contents upslope, mid-slope and downslope were measured at 5, 15, 40 and 80 cm depth at hourly resolution between May 2010 and November 2013.

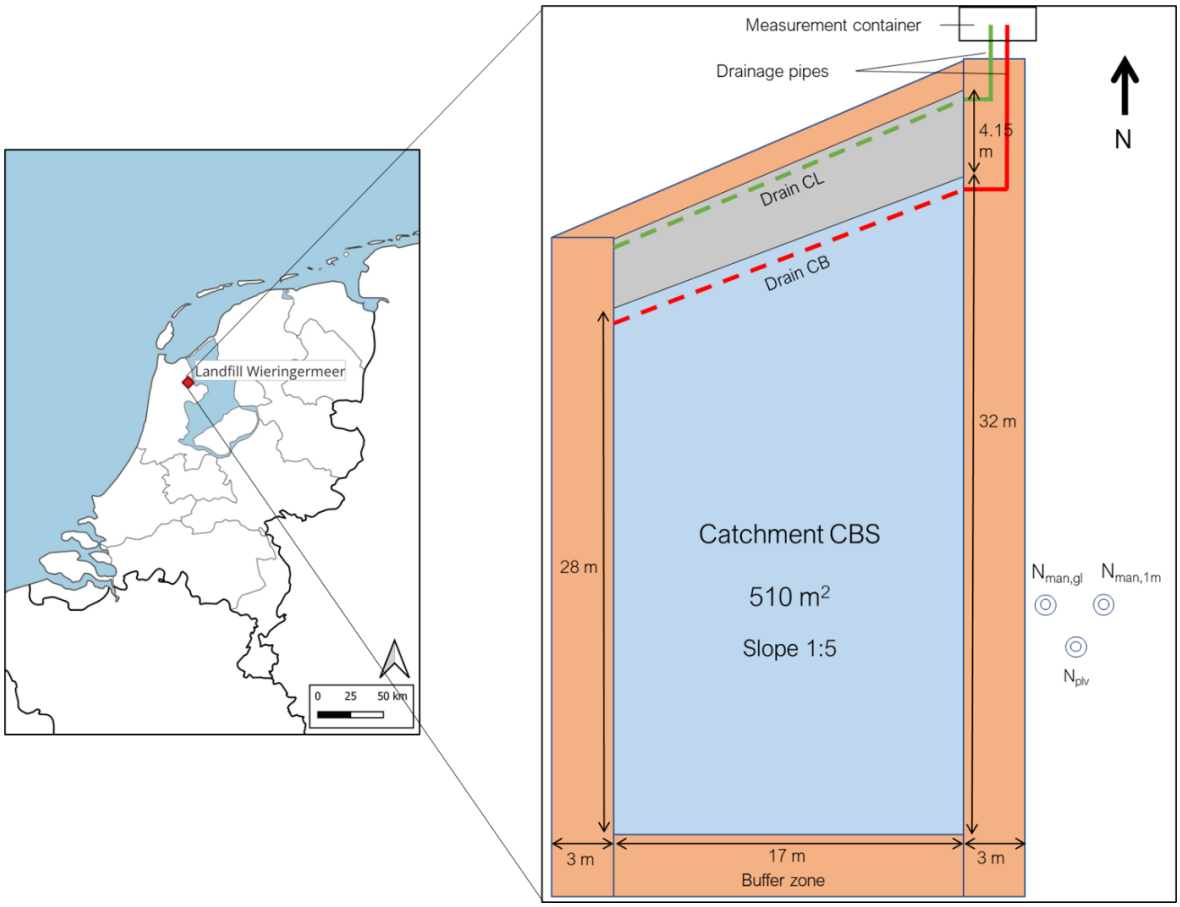

Figure 5: Location of landfill in the Netherlands (left; Made with Natural Earth) and a top view of the test field. Given distances are measured along the slope. The CL and CB drain separately. The precipitation falling in the drainage area of the CL (grey) is drained away by a drainage mat on top to prevent the collection of extra infiltration. Three rain gauges were installed besides the field: Two manually measured gauges at ground level ($N_{man,gl}$) and 1 m height ($N_{man,1m}$) and one automatic Pluvio-2 rain gauge (N_{plv}) (Melchior+Wittpohl, 2009)

Table 1: List of available data (: Before replacement of the computer at the measurement container (23-11-2015) the data is on 5/15 min scale and afterwards the time scale is 1 hour. **: Measurements were not regular)*

Time series	**Period**	**Time scale**
Cumulative precipitation automatic rain gauge Pluvio-2	Nov 2009 – June 2023	5 min – 1 hr*
Precipitation manual rain gauge at 1 m height & ground level	Nov 2009 – June 2023	1 week - 1 month**
Cumulative switches pump CB & CL	Nov 2009 – June 2023	15 min - 1 hr*
Cumulative switches tipping bucket CB & CL	Nov 2009 – June 2023	15 min - 1 hr*
Tipping bucket clean & dirty volume CB & CL	Nov 2009 – June 2023	~ 1 month**
Water content up-, mid- and downslope at 5, 15, 40 & 80 cm depth	May 2010 – Nov 2013	1 hr

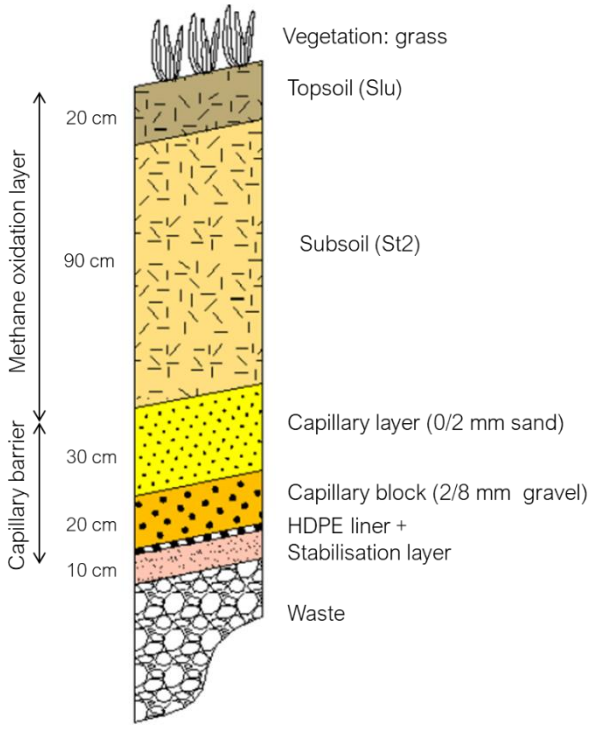

Figure 6: Cross section of the cover soil (Melchior+Wittpohl, 2009). *Slu and St2 are German soil texture classes which stand for a silty clayey sand and a slightly clayey sand, respectively* (Blume et al., 2016).

3.2. Soil properties

During construction, the soil properties of all soil layers were measured at multiple, unknown locations. Additionally, during the four years after that the soil properties of the MOL were measured three times: in April 2011, August 2013 and September 2013. The last two measurements were done before and after the reconstruction of the topsoil of the field, both up- and downslope.

The soil properties relevant for water flow that were measured were the grain size distribution (GSD), the measurements for the SWRC and saturated and unsaturated hydraulic conductivity measurements. Full tables of these measurements and an explanation on how they were executed can be found in Appendix B.7.

The locations of excavations and soil sampling were located in the buffer zone surrounding the test field. They are shown in Appendix B.6 together with photos taken during these excavations and a qualitative measurement of the root density during the April 2011 excavation.

These pictures show, for example, that in August 2013, right before the reconstruction, the top 40 cm of the soil had aggregated. Also, most rooting seems to happen in the top 20 cm which is approximately the depth of the TS. Furthermore, at the bottom 3-4 cm of the CL there were iron precipitates observed. As these were also present in the outflow of the CL and CB, it is most likely that most CL flow happened in the bottom 3-4 cm, which is a phenomenon which was also observed by other studies (Kämpf et al., 2003; Stormont, 1996). Lastly, the excavation

in 2011 observed that the topsoil had a depth of 0.45 m, which could be due to inaccurate construction.

3.2.1. Grain size distribution

The GSD of the different soil layers is shown in Figure 7. These measurements were performed in 2009 after the construction of the field and an additional sampling of the CB was done in 2017.

In general, the grain sizes increase with depth. The original gravel used for the CB had grain sizes of 2-8 mm. In the years after construction, ingress of sand particles between 0.06 and 2 mm size happened, as it makes up for 30% of the total weight in 2017. The sand particles used for the CL have sizes between approximately 0.1 and 3 mm. The material with which the SS was constructed consisted for 10% of clay, 10% of silt and the remaining particles had mainly a size between 0.1 and 0.5 mm. Additionally, it contained 2.3 mass-% of organic substances. Lastly, the TS consisted for approximately 14% of clay, 40% silt and 50% sand particles and had an organic fraction of 4.4 mass-%.

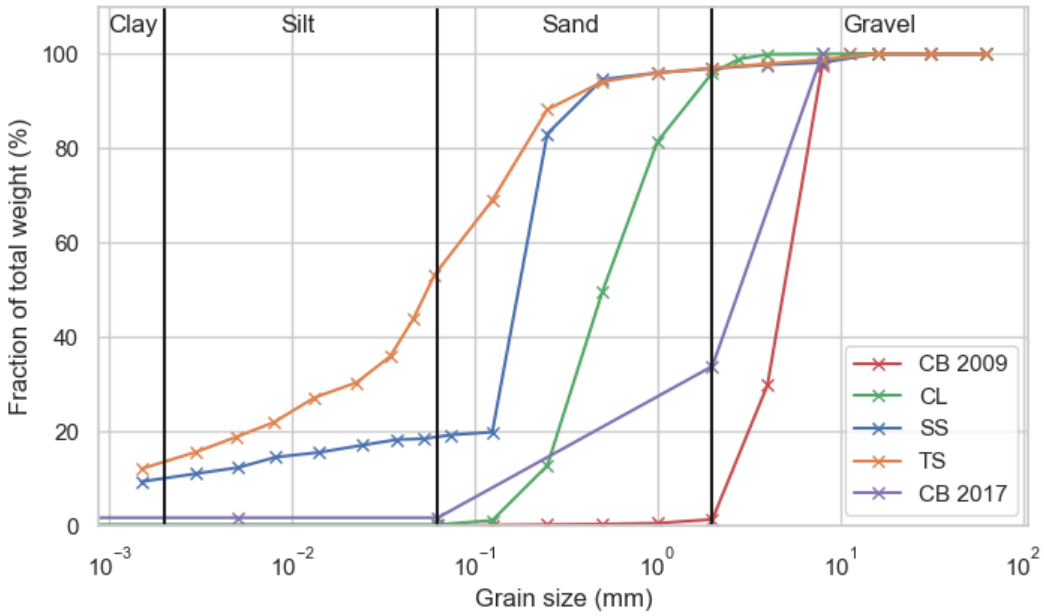

Figure 7: Grain size distribution (GSD) for the four soil layers, measured after construction in 2009. The CB was measured again in 2017 (Melchior+Wittpohl, 2009; Verseveld, 2018).

3.2.2. Water retention

The measurements of the water retention and unsaturated hydraulic conductivity of at different depths over time are shown in Figure 8. Tables with their exact values as well as the porosities are presented in Appendix B.7.2.

In 2017 more than 200 measurements were made with small differences in suction head between each measurement, so only a representative subset is shown here. The depth at which these soil samples were taken was estimated as 0.3 m based on photos of the excavation.

In general, the water retention measurements of depths of 0.3-0.35, 0.5 and 0.68-0.8 m (SS) are similar. The water retention in the TS at 0.05 m depth is generally higher at higher suction head, which can be explained by its higher silt and organic matter content. Contrarily,

the CL shows a drastic decrease with increasing suction head which can be explained by its narrow GSD.

The water retention measurements at each depth show a range of approximately 10 vol.-% at each suction head level. However, at a depth of 0.3-0.35 this spread in observations is larger, even up to 20 vol.-%, mainly originating from the measurement done in 2011. These might also be outliers, however. The differences between the measurements of each depth are the least for a depth of 0.68-0.8 m, especially at higher suction heads. This is plausible because physical and biological influences on the soils structure are less pronounced at that depth.

A different response in water retention behaviour can be seen between the depths 0.05, 0.3-0.35 and 0.5 m on the one hand and 0.68-0.8 m on the other hand. The first group of depths shows a difference between up- and downslope measurements at higher suction head before the reconstruction in 2013 and a more uniform up- and downslope behaviour afterwards. As these soils were excavated and build up again, a more uniform behaviour is reasonable. In contrast, at a depth of 0.68 m the difference in up- and downslope measurements increased after the reconstruction in 2013. As the soil at this depth was not excavated and redistributed, it might have happened that some parts were more compacted than others.

The development of pore sizes derived from these suction measurements is shown in Appendix B.7.4. Generally, the share in volume of each pore size category remained stable except for the wide coarse pores. However, their decrease is most likely of little influence on the unsaturated flow of water as the medium and fine-coarse pores are the most important for that (Blume et al., 2016).

3.2.3. Hydraulic conductivity

The saturated hydraulic conductivities are presented in Appendix B.7.3. The order of magnitude of the TS, SS and CL is the same (10^5 m/s) and is typical for sandy soils (van Genuchten et al., 1991). Only the TS has a lower conductivity after the reconstruction but it is likely that this value increased again afterwards by bioturbation and soil aggregation (Melchior+Wittpohl, 2014a).

However, the measured saturated hydraulic conductivities of the CL and the September 2013 measurements at 0.05 m depth are lower than the measured hydraulic conductivity at 10 cm suction head. This difference might be explained by that the unsaturated hydraulic conductivity measurements were performed in the field, while the saturated hydraulic conductivities were measured on soil samples in the laboratory.

3.2.4. Design diversion capacity

Lastly, during the design phase of the test field, the diversion capacity of the CBS was estimated to be approximately 20 mm/d based on the properties of the soils used for the CL and CB. Furthermore, it was assumed that the infiltration entering the CL would be around 10 mm/d in general and 25 mm/d during precipitation peaks. Thus, the diversion capacity was estimated to be sufficient to divert most of the flows, but would also be overloaded in cases of extreme precipitation. In this way the limits of the CBS on field scale could be determined (B. Steinert, personal communication, July 24th 2023).

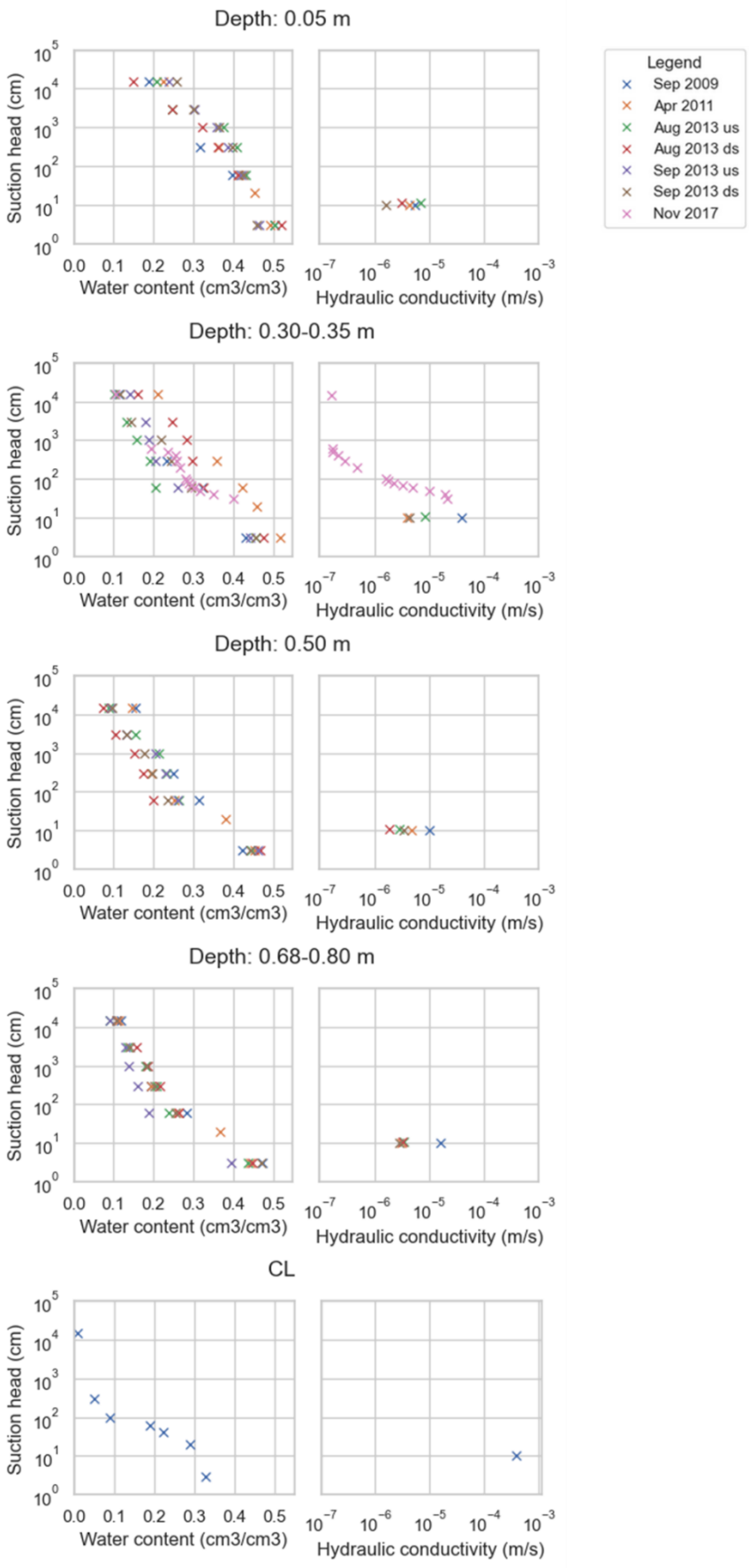

Figure 8: Measured water contents and hydraulic conductivities against suction head (Melchior+Wittpohl, 2009, 2011, 2014a; Verseveld, 2018).

4. Methodology

4.1. Conceptual model water balance

Figure 9 shows a preliminary conceptual model of the test field with all possible water flows coming in and going out of the system (based partly on Melchior+Wittpohl (2014b), assuming no flow passes the HDPE borders.

The water fluxes that were assumed to be negligible are incoming and outgoing runoff and subsurface flow in the MOL. Runoff coming in the cell (R_{in}) is likely to be zero as an infiltration ditch was build upslope of the test field in order to infiltrate any possible runoff. Additionally, upslope subsurface inflow is also estimated to be negligible because a drain was placed just before the start of the test field in order to divert incoming subsurface flow.

Furthermore, outgoing runoff is expected to be zero as well as this was not observed during field visits. Also, the saturated hydraulic conductivity of the TS is sufficiently high (> $1*10^{-5}$ m/s) to accommodate for the largest precipitation event in the dataset (23.2 mm/h).

Lastly, the outgoing subsurface flow from the MOL was also assumed to be zero, although this might be invalid because it is likely that a CBE exists between the SS and the CL. The WEV and the shape of the SWRC of both soils is similar, but the MOL always contains approximately 10 vol.-% more water at suction heads larger than 100 cm. The hydraulic conductivity in the SS could range 10^{-8} to 10^{-7} m/s, based on estimates using the Averjanov model as explained later in this chapter. The subsurface outflow from the MOL might therefore be considerable. However, quantifying this outflow was not considered feasible in the time given for this research, so the flux was assumed to be negligible, introducing a potential error in the water balance.

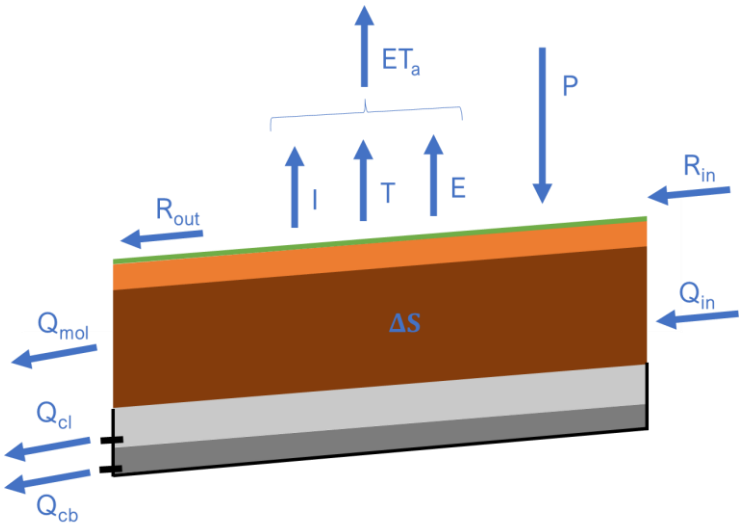

Figure 9: Conceptual model of all water flows in a cover consisting of a methane oxidation layer and a capillary barrier at Wieringermeer landfill: precipitation (P), interception (I), transpiration (T), evaporation (E), actual evaporation (ET_a), incoming and outgoing runoff (R_{in} and R_{out}), outflow from the capillary layer (Q_{cl}) and the capillary block (Q_{cb}), subsurface in- and outflow of the methane oxidation layer (Q_{in} , Q_{mol}), storage in the TS, SS and CL (ΔS).

The remaining water fluxes were either measured (P, Q_{cl}, Q_{cb}) or modelled (evapotranspiration). The actual evapotranspiration (ET_a) is comprised of interception (I), transpiration (T) and soil evaporation (E). This flux is the largest in this model given that the

yearly average evaporation of a well-watered field in the Netherlands lies between 500 and 600 mm (KNMI, 2022). Modelling this flux will also give an estimate of the water storage in the CBS and MOL combined (ΔS).

The final water balance can then be described as:

$$\Delta S = P - ET_a - Q_{cl} - Q_{cb} \qquad \text{Equation 7}$$

4.2. Data analysis

4.2.1. Data preparation

The raw data of tipping bucket and pump switches, water content and precipitation needed to be processed as these datasets contained unreliable data and outliers. For example, measurements with a temporary offset, unrealistic high amounts of precipitation or switches, zero readings while other devices registered precipitation or flow and maintenance periods were omitted. The details of this process are described in Appendix C.1. Furthermore, switches and precipitation data was gathered cumulatively which was converted to discrete data by taking the difference between consecutive measurements.

Data gaps

The dataset has many gaps ranging from a few hours to half a year (2015). Some of them are the result of the cleaning of the data, but most were caused by power cuts of the data monitoring system in the measurement container (CARS). However, in case of a power shortage of CARS, the tipping buckets and pump switches and the precipitation amounts were continued to be counted cumulatively, preserving the total flow over that power shortage period.

However, when calculating discrete data of a certain scale, a no-data period stretching two or more of these discrete data periods will distort their values. For example, when calculating daily precipitation data, the day on which the no-data period starts misses some rainfall (provided that it falls in the no-data period). Conversely, the day at which the no-data period ends receives all the precipitation of the no-data period because of the cumulative registration.

The timescale of any analysis determines if these data gaps are distorting the results. For example, on a yearly time scale data gaps all fall within the analysis time scale and do not cause issues. On a daily time scale, however, the effect of data gaps might be more noticeable. Therefore, this study handled these distortions using the following approach: For a certain analysis on a time scale Δt, an aggregate discrete data point q_i is discarded when the difference between the time of the last measurement m_i in its time interval and the end of this time interval is larger than a factor ϵ times the time scale of the analysis (Equation 8).

$$t_{q_i,end} - t_{m_i} > \epsilon * \Delta t \qquad \text{Equation 8}$$

With $t_{q_i,end}$ the end of the time interval of aggregate data point q_i, t_{m_i} the time of the last measurement m_i in the time interval of data aggregate point q_i, ϵ an arbitrary value and Δt the time scale of the analysis (day, season, year).

In other words, an aggregate discrete data point is omitted from a certain analysis once a no-data period of a minimum length of $\epsilon\Delta t$ starts but not ends within its time interval. Additionally, aggregate data points containing the end of a no-data period are also omitted.

ϵ should be chosen such that only data aggregate points that are severely decreased because of missing data at the end are omitted from the analysis. This research used a ϵ- value of 0.08 for each time scale which is approximately equal to 2 hours, 1 week and 1 month with an aggregate time scale of a day, season (three months) and a year, respectively.

Calculation of outflows

The outflows from the CL and the CB were calculated in duplicate using tipping bucket and pump data. The pump data served as backup in case the measurements of the tipping buckets failed. The outflows of both the tipping buckets and the pumps can be calculated by multiplying their datasets on switches over time with a discharge volume per switch.

The volume of the tipping buckets was measured indirectly by weighing the amount of water fitting in the bucket until it tips. The volume was then obtained by dividing this weight by the density of the water at 15 °C (0.999 kg/L). However, the monthly measurements are prone to relatively large (systematic) errors (as explained under Appendix C.3.1). Therefore, these measurements cannot be used as a reliable estimate of the volume at their time. Instead, the mean of all measurements was used as tipping bucket volume for the whole measurement period. The mean tipping bucket volume was 2.90 and 2.86 L for the CL and CB, respectively.

The volume per pump switch was estimated as 0.5 m^3 for both the CL and the CB, based on its switch on and off water level, which span approximately half of the 1 m^3 IBM tank.

The discharge normalised to the catchment area was then calculated as:

$$Q_{d,l}(\mathrm{t}) = \frac{S_{d,l}(t)V_{d,l}}{A} * 1000\frac{mm}{m} \qquad \text{Equation 9}$$

In which $Q_{d,l}$ is the outflow [mm h^{-1}], $S_{d,l}$ the amount of switches [h^{-1}] and $V_{d,l}$ the volume per switch [m^3] for device d (tipping bucket or pump) and layer l (CL or CB) and A the area of the test field parallel to sea level (500 m^2).

The final discharge timeseries used in the analysis consists of tipping bucket data where pump data has been inserted when tipping bucket data were unreliable (Appendix C.2).

4.2.2. Validity of data

As mentioned before, the mean value of the tipping bucket volume over the whole period was used instead of the measurement of the volume at each different time. This could potentially introduce an error of 4%. However, comparing the outflow calculated from the tipping bucket and pump switches showed that both were in good agreement in general (Appendix C.3.2). Although both outflow estimates contain systematic biases their agreement reinforced the trust in the tipping bucket measurement estimates.

Furthermore, the three different local precipitation observations were highly different from each other and from measurements done by the two stations of the national Dutch weather service (KNMI) at Medemblik (daily manual measurements, ~1 km away) and Berkhout

(Hourly automatic measurements, ~16 km away) (Appendix C.3.3). Therefore, the KNMI data from Berkhout were used instead for calculating the water balance on a daily time scale as these measurements are of high quality and showed sufficient correlation with the Medemblik and local measurements. The Pluvio-2 dataset was used as a reference or when modelling on hourly level.

4.2.3. Effect of changing grain size distribution of the CB

As observed in the excavation of 2017, the grain size distribution of the CB had changed. The share in particles smaller than 2 mm had increased from 1% to 34%, which affects the SWRC and SHCC of the CB significantly. In order to make an estimate of the impact of this change, a method to derive the SWRC based on the GSD proposed by Zhai et al. (2020) was used. This method was derived specifically for coarse grained soils. It evolves around geometrical relationships between particle diameters and the radii of menisci between these particles and uses the Young-Laplace equation (Equation 3) and Decartes' theorem of circles. A contact angle of 0° was assumed.

4.3. Modelling evaporation and storage

4.3.1. Scope

The goal of developing a model was to quantify evapotranspiration and soil water storage in the complete soil cover in the test field on a daily scale. As there were only outflow and water content data available, the model was kept as simple as possible to reduce the amount of assumptions and parameters.

Therefore, a one-dimensional finite difference model was built simulating the upper three layers (RL, SS, CL) of the test field (Figure 10). Flow in these soil layers is assumed to be vertical. As there is lateral flow between the CL and the CB which the model cannot accommodate for, the CB was not included. Therefore, the sum of both outflows was used to calibrate the model. Also, the measured outflows are also the result of three- instead of dimensional flow. Thus, the properties of the CL in the 1D model were a combination of the properties of the both the CL and CB and also included their lateral flow properties. (Appendix B.6.3).

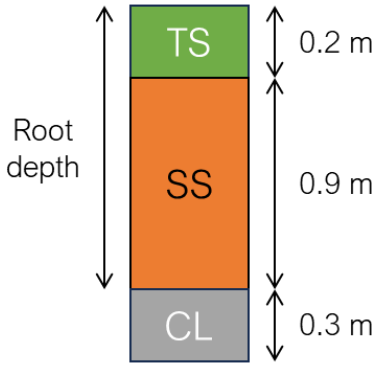

Figure 10: Geometry of modelled soil layers

The model only takes water flow into account. Gas flow and influences of entrapped air were not accounted for. Moreover, soil hysteresis and the influence of temperature on water viscosity and the type of precipitation were not included.

Lastly, only transpiration is simulated. Evaporation is not calculated separately because it would make the model more complex and would require more non-available input data or assumptions. Also, evaporation typically happens at the top of the soil. As the transpiration uses an exponential root density model and thus takes place mostly in the topsoil like evaporation, it was assumed that evaporation is lumped into the transpiration calculation.

4.3.2. Governing equations and parameters

The finite difference model solves Richards' equation with root water uptake for the suction head. The equation is modified such that the compressibility of the soil and water is taken into account as well. By doing so, sudden changes in suction head can be accommodated for. A full derivation of this modified Richards' equation is presented in Appendix C.4 and yields:

$$(C(h_m) + S_e S_s)\frac{\partial h_m}{\partial t} = -k_s k_r(h_m)\left(\frac{\partial h_m}{\partial z} + 1\right) + S_r \qquad \text{Equation 10}$$

With $C(h_m) = \frac{\partial \theta_w}{\partial h_m}$ the differential water capacity [m^{-1}], $S_s = C_v + n\beta_w$ the specific storage [m^{-1}] (with C_v and β_w the compressibility of the soil matrix and water [m^{-1}], respectively) and S_r the source term used to model root water uptake [m^3 water m^{-3} soil d^{-1}] [2].

SWRC and SHCC model

Many of the terms in Equation 10 depend on the SWRC and the SHCC of a soil. Different models have been developed to describe these relationships. This study uses the model of Van Genuchten (VG) for the SWRC because of the smoothness of its function (van Genuchten, 1980):

$$S_e = \left[\frac{1}{1 + (\alpha\,|h_m|)^n}\right]^m \qquad \text{Equation 11}$$

With α [m^{-1}] m, and n fitting parameters.

It is common in literature to use the Mualem model in combination with the VG model to describe the SHCC. This study tried this initially as well, but the solver could not find a solution as a result. Most probably this was due to the strong decrease in hydraulic conductivity in this model. Therefore, the simpler and less steeply decreasing model of Averjanov (1950) was adopted, which is suitable for coarse grained soils (Lu & Likos, 2004, Chapter 12):

$$k_r(S_e) = S_e^n \qquad \text{Equation 12}$$

Where a value of n of 3 was taken as this is valid for most soils (Lu & Likos, 2004).

[2] Source term can also have the unit of h^{-1}, depending on the time resolution of the model run.

Root water uptake

The sink term in Richards' equation changes over time and depth. It is dependent on the available soil moisture and the root length or mass density at a certain depth and the potential transpiration at a given time (T_p [m d^{-1}]). The latter is the rate of transpiration of a certain crop on a well-watered and fertile soil (Feddes & Raats, 2004). Li et al. (2001) developed a model which can be used in a finite difference study which is slightly modified in this study. The soil profile is divided in N layers. For every layer i with a depth of Δz_i [m] and elevation at its centre z_i [m] the root water uptake is calculated.

Their model consists of two parts. Firstly, the total potential transpiration is distributed over the total root zone which gives the maximum root water uptake at each depth. Secondly, the actual root water uptake at each depth is then calculated by correcting the maximum root water uptake with the moisture availability reduction factor.

The distribution of the maximum root water uptake is calculated using a combination of the available moisture reduction and relative root density factors. Considering the first, a simplified version of the function showed in Figure 11 is used. For suction heads smaller than h_1 and larger than h_4 the value of α_w is zero. In the first case this is the result of the non-availability of oxygen and in the second case the plants are no longer able to extract water from the soil (PWP). Furthermore, the value of h_3 depends on the non-limited transpiration rate but for simplicity a single constant value was used.

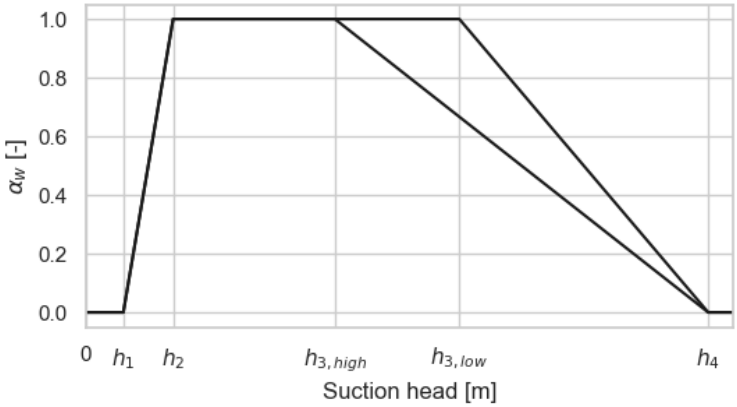

Figure 11: Linear model of transpiration reduction because of limited soil moisture availability (Feddes & Raats, 2004)

Considering the root length density function, a simple exponential density model was selected, different from what Li et al. (2001) used:

$$L_r(z_i) = L_{r,z_0} e^{bz_i} \qquad \text{Equation 13}$$

With L_r the root length density [m m^{-3}], L_{r,z_0} the root length density at z=0 [m m^{-3}] and b [m^{-1}] an empirical extinction coefficient. As z is negatively defined, the root length density will decrease with depth as well.

Using a discretised version of the equation provided by Feddes & Raats (2004) and Equation 13, the relative root density can be calculated:

$$\beta_r(z_i) = \frac{L_r(z_i)\Delta z_i}{\sum_{i=0}^{N} L_r(z_i)\Delta z_i} = \frac{e^{bz_i}\Delta z_i}{\sum_{i=0}^{N} e^{bz_i}\Delta z_i} \qquad \text{Equation 14}$$

Next, the function determining the distribution of maximum root water uptake over depth returns the product of the relative root density and the water stress reduction factors at z_i as a fraction of the sum of the same product over the entire soil profile:

$$\gamma(z_i) = \frac{\alpha_w(h_{m,z_i})\beta_r(z_i)}{\sum_{i=0}^{N}\alpha_w(h_{m,z_i})\beta_r(z_i)} \quad \text{Equation 15}$$

With γ the stress-weighted distribution factor [m], α_w the moisture reduction factor [-] and β_r the relative root length density [-].

Subsequently the maximum water uptake at depth z_i over the soil layer Δz then becomes:

$$S_{r,max}(z_i) = \frac{\gamma(z_i)}{\Delta z}T_p \quad \text{Equation 16}$$

With $S_{r,max}$ the potential root water uptake [$m^3\,m^{-3}\,d^{-1}$] and T_p the potential transpiration at a given time [md^{-1}].

The actual root water uptake at each depth is then calculated by multiplying this maximum root water uptake with the moisture availability reduction factor:

$$S_r(z_i) = \alpha_w(h_{m,z_i})S_{r,max}(z_i) \quad \text{Equation 17}$$

With S_r the actual root water uptake [$m^3m^{-3}d^{-1}$], α_w the moisture availability reduction factor [-], h_{m,z_i} the suction head at depth z_i [m] and $S_{r,max}$ the maximum root water uptake [$m^3m^{-3}d^{-1}$].

The total actual transpiration then becomes the sum of the actual water uptake over the entire root zone:

$$T_a = \sum_{z_r}^{0} S_r(z_i) \quad \text{Equation 18}$$

Solving algorithm

The method of solving a linearised Richards' equation is described in detail in Appendix C.5. The equation was linearised in space over elements of 0.01 m size. The linearisation in time was done with a time step of an hour and 15 minutes when the model is run for daily and hourly scale results, respectively. All the equations above were implemented in Python and converted to a system of linear equations. The latter was solved using the *solve_ivp* function of the *scipy* library (Virtanen et al., 2020) using the *BDF* method (Shampine & Reichelt, 1997) with a relative tolerance of $1*10^{-4}$.

4.3.3. Geometry, boundary and initial conditions

The boundary condition at the top of the soil column was Neumann, where the inflow rate was equal to the precipitation. In case the precipitation amount exceeds the hydraulic conductivity of the top layer, the inflow is converted to a change in suction head by changing the differential water capacity to $\frac{1}{\Delta z_N}$ such that $\frac{\Delta h_m}{\Delta t} = q_{w,N+1} - q_{w,N} - S_{r,N}$.

The bottom boundary condition was defined as gravity outflow with a unit head gradient. Accordingly, the outflow is equal to the hydraulic conductivity of the soil in the lowest layer. In reality this is not valid since there exist CBEs at the bottom of the CL. However,

it was still chosen as this 1D model uses outflows which are the result of a 3D situation in which the outflow is likely to be under atmospheric pressure. Also, Kämpf et al (2003) observed that unit gradient flow conditions prevail in the CB.

As initial condition an uniform initial pressure of -1 m was used. This is a situation close to saturation which is valid for winter conditions. Furthermore, every model run includes a warmup period. The length of this period was chosen such that extending it did not have noticeable effects on the outflow and water content at the start of the period of interest. Concerning the final results which commenced in October 2009, the start of the warmup period was at March 2009.

4.3.4. Data used

The precipitation data used as input into the model differed per time scale. When run on an hourly level, the local Pluvio-2 measurements were used. On the other hand, on a daily time scale the daily precipitation data from the Berkhout KNMI weather station was used (KNMI, 2023b).

The potential evaporation dataset consisted of the daily estimations of the Makkink evapotranspiration values at the KNMI station of Berkhout (KNMI, 2023a). These are estimates of the total evaporation from a well-watered grassland. This includes evaporation from the soil, evaporation of the intercepted precipitation by vegetation and transpiration (Spieksma et al., 1995). This can be used as potential evaporation by multiplying its estimations with a crop factor which includes the effect of the different vegetation type at the test field. As this vegetation is also grass, a crop factor of 1 was assumed.

Lastly, both precipitation and evaporation data were distributed uniformly over their time scale (day or hour).

4.3.5. Model calibration and testing procedure

There are in total 20 parameters in the model. For each of the three soil layers there are two VG parameters (α and n, as m was assumed to be $1-\frac{1}{n}$), a saturated hydraulic conductivity (k_s) and a saturated and residual water content (θ_s and θ_r, respectively). Additionally, there are the parameters from the transpiration model. The moisture reduction factor function requires four parameters (h_1, h_2, h_3, h_4) and the relative root density function one (b). The total root depth z_r was set as a constant 1.1 m based the maximum root depth found during the excavations (Appendix B.6.3). Furthermore, the compressibility of water was assumed to be $4.5*10^{-6}$ m^{-1}. The compressibility of the soils was assumed to be the same for all layers. As all layers consisted of sandy soils, a value of $1*10^{-4}$ m^{-1} was used (Kuang et al., 2020).

Calibration goals

For each of these model parameters an initial estimate was made based on measurements (Appendix C.6.2). Subsequently these were adjusted based on the comparison of model outcomes with the measured mid-slope water contents at 5, 15, 40 and 80 cm depth and the combined outflow of the CL and CB. The measurements of the mid-slope water contents were chosen because it was assumed that they would represent average conditions for the whole

slope and they also showed little unexpected behaviour. The calibration was done manually as optimising using a computational algorithm resulted in parameter values which did not reproduce the observed patterns in outflow and water content correctly.

The parameter adjustments were done to achieve the following goals (in order of priority):

1. The ratio of the sum of simulated outflows over the sum of observed outflows should be one.
2. The timing of the start of an outflow event and the timing of its peak should be similar for the simulated and observed outflows.
3. The simulated and observed water contents should be fluctuating around the same level.
4. The timing of a peak in water content and the rate of decrease afterwards should be similar for the observed and simulated water contents.
5. The sum of transpiration should be comparable to the sum of precipitation minus the sum of outflow from March 2011 to March 2012.

These goals were derived from the overall model goal. To quantify storage and evapotranspiration the first priority is to match the measured outflow quantity to close the water balance. Secondly, as the third research question is to quantify storage during a breakthrough event, the timing of the start and the peak of the combined CL and CB should be simulated appropriately.

Thirdly, to model the storage and the transpiration well, the water content at different depths should have a similar behaviour as observed, which is aimed for with the third and fourth goal. However, the difficulty with the third goal was that the average measured water contents mid-slope decreased with depth which is likely due to a difference in soil properties. On the other hand, the assumption in the model is that the cover soil consists of two uniform soil layers. Within a uniform soil layer the water content increases with depth under hydrostatic conditions as a result of a decrease in total and consequently suction head. Therefore, the approach was taken to strike a balance between fitting to the observations at 80 and 40 cm for the parameters concerning the SS and the observations at 5 and 15 cm for the TS parameters.

Lastly, the main estimate available for calibrating transpiration parameters is the yearly residual precipitation. However, there is uncertainty in the assumption that the transpiration should be equal to this residual. The assumption that the storage in March is similar each year is reasonable as evaporation is low and the soil is likely to be at hydrostatic equilibrium. However, the yearly residual precipitation is not necessarily equal to yearly evapotranspiration. Firstly, part of this residual consists of flow leaving the system through subsurface flow in the MOL. It contains also the error in the outflow measurements which can be 4%. Secondly, there is a time lag between a precipitation event and its outflow. For example, there is 20 mm precipitation event in February 2011 that causes an outflow wave in March 2011 (Figure 20). This doesn't happen at March 2012. Accordingly, the precipitation causing the outflow between March 2011 and 2012 is slightly higher, which results in an underestimation of the residual (455 mm) of maximum 5%. Therefore, the goal was to match the yearly transpiration within 5% of the yearly residual precipitation.

Calibration procedure

The soil hydraulic parameters can be best adjusted in a period with little evaporation where drainage is the main factor determining outflow and water contents. Similarly, the transpiration parameters together with θ_r can be best calibrated in a period with high potential evaporation when the soil dries out. The water content measurements spanned three and a half year (May 2010 – November 2013). The period between May 2010 and March 2012 was used for calibrating the model whereas the period between March 2012 and November 2013 was used for testing the model. Both subsets of data contain two period where the soil dries out. The warmup period for calibrating data subset started in March 2010. The testing data were run in combination with the calibration data. Additionally, a single drainage event during winter (01-01-2012 to 05-01-2012)[3] at hourly time scale was used to see if the model could accurately reproduce the soil moisture and outflow dynamics. The warmup period for the event started 15 days earlier at 15-12-2011.

The initial values of each of the parameters and a full description of the calibration process are presented in Appendix C.6. The final values are presented in Table 2. The initial soil hydraulic parameters were determined from the soil measurements as described in Appendix B.7. A VG model was fitted using the RETC-software (van Genuchten et al., 1991), where the water content at 15,000 hPa was used as θ_r and the (wet) porosity as θ_s. The resulting curves are shown in Appendix C.6.2. The SHCC, which was not fitted but is based on the fitted SWRC, overestimates the conductivity measurements at 10 cm suction head with a factor 10. Finally, the arithmetic mean was taken for θ_r, θ_s and n and the geometric mean for lognormally distributed α and k_s over all measurements[4] (Ogorzalek et al., 2008).

The parameter b determining the shape of the root density function was estimated based on pictures of the several excavations and the classification in April 2011 (Appendix B.6.2). These showed that the majority of the roots were located in the TS. The initial value of b was chosen such that the sum of the relative root density β_r of the top 20 cm was 85%.

Table 2: Final values of model parameters. Underlined values are different from the values derived from measurements.

Transpiration model					
α_w **thresholds [m]** (Feddes & Raats, 2004)	h_1	h_2	h_3	h_4	
	-0.1	-0.25	-5	-80	
***b* [-]**			10		
Soil hydraulic parameters					
	θ_r	θ_s	α [m^{-1}]	n	k_s [md^{-1}]
TS	**<u>0.15</u>**	**<u>0.45</u>**	5.0	**<u>1.3</u>**	3.88
SS	**<u>0.10</u>**	0.47	13.4	**<u>1.42</u>**	2.93
CL	0.01	**<u>0.30</u>**	**<u>10.0</u>**	**<u>2.0</u>**	**<u>1.0</u>**

[3] This was the only drainage event in winter in the dataset with no gaps in the Pluvio-2 precipitation measurements, which is required for the model to run on hourly basis.

[4] The measurements of the TS of September 2009 and 2013 were omitted because the highly compacted state of the topsoil after (re)construction was not seen as representative for the state from 2009 to 2023.

4.4. Water balance analysis

Finally, the water balance on a yearly scale was calculated by summing all measured and simulated water fluxes over the period between June and June the year after. This definition of the hydrological year was used to minimise carry-over effects due to precipitation from the year before that flowed out in the next year. In most years the flow from the CL and CB was negligible in June.

Furthermore, the four seasons within a hydrological year were defined as summer (June to September), autumn (September to December), winter (December to March) and spring (March to June).

The storage in the cover soil was calculated by integrating the water contents over the entire model length, thus including the TS, SS and CL. To put the estimated storage into perspective, also the storage at FC and the PWP was estimated. Concerning the latter, it was assumed that a the soil would be uniformly at the maximum suction plants can exert found during the calibration (h_4: 80 m).

Regarding the storage at FC, the main difficulty is to determine the suction head over the soil profile. There is no stable reference level given the soils are located on a slope and can drain freely. Stormont & Anderson (1999) observed a hydrostatic suction head profile in the CL when infiltration rates were low compared to the soils' conductivity. When these were higher, an infiltration suction head profile developed, where the suction head remains constant with height. Moreover, Yang et al. (2004) observed that after an infiltration event, the suction profile moves to a situation where there is a hydrostatic profile up to a certain maximum matric suction head, defined by two times the residual matric suction head in Fredlung and Xing SWRC model (Fredlund & Xing, 1994). Above that level there is a constant suction head (Figure 12). However, a detailed determination of the maximum storage in the soil profile using this model was not possible due to time constraints. Instead, a simplification was made by assuming a constant suction head over the entire soil profile. To be conservative, the lower limit of the range in commonly possible suctions at which soils are at FC was used (300 cm).

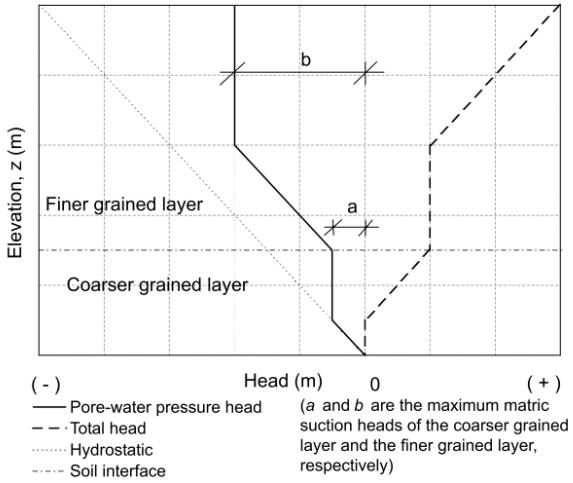

Figure 12: Conceptual equilibrium suction head profile in a CBS. Pore-water pressure head refers to suction head. Adopted from Yang et al. (2004).

Lastly, for each of the time scales where the water balance was calculated for, there is also an error between the modelled and observed outflows. This is equal to the error in the simulated change in storage and evapotranspiration, which can be derived by the equations of the observed and simulated water balance:

$$\Delta S_{sim} = P_{obs} - ET_{sim} - Q_{sim} \quad \text{Equation 19}$$

$$\Delta S_{obs} = P_{obs} - ET_{obs} - Q_{cl} - Q_{cb} \quad \text{Equation 20}$$

The error in the simulated outflow is defined as:

$$Q_{err} = Q_{sim} - (Q_{CB} + Q_{CL}) \quad \text{Equation 21}$$

Rewriting and combining Equation 19, Equation 20 and Equation 21 yields:

$$\Delta S_{obs} + ET_{obs} = \Delta S_{sim} + ET_{sim} + Q_{err} \quad \text{Equation 22}$$

This means that if the error in the simulated outflow is positive, either ΔS_{sim}, ET_{sim} or a combination of both are underestimated. Reversely, if the error is negative, they are overestimated.

5. Results

5.1. Model calibration and testing

Figure 13 shows the observed and simulated outflows, water contents and the simulated and potential evapotranspiration for the calibration and testing period. Furthermore, the calibration result of the drainage event in January 2012 can be found in Appendix D.1.1. The cumulative mass balance error due to linearisation in the model did not exceed 3 mm.

The simulated outflow matches the general timing of outflow events and outflows have a similar order of magnitude. Moreover, for the calibration period the total simulated flow is similar to the observed total flow. However, for the testing period it is underestimated by 6%.

On the contrary, the outflow pattern is not adequately captured. Its simulated behaviour has relatively high peaks and fast receding flows when compared with the observed outflow.

This is also visible in error in the outflow error (simulated – observed) which follows a yearly pattern. Generally, it is overestimated between September and March where the error in the magnitude of the peaks can be up to 5 mm/d. Between March and September the flow is generally underestimated. The cumulative error at the end of the testing period before the highly overestimated peak in November 2013 was -80 mm.

The simulated water contents also follow the general behaviour of the observed mid-slope water contents. However, opposite to the observed dampening of fluctuations in water content with depth, the model shows similar behaviour at all depths. Close to the surface the model shows too little fluctuations and instead follows a more average behaviour.

On the contrary, the simulated water contents at 80 cm depth are too dynamic in comparison with the observed trend. This is also visible when the soil starts drying out. In general, the timing of drying out is approximately correct at 5 and 15 cm depth (except for 2013), but not at 40 and in particular 80 cm depth where the drying process starts too early.

Furthermore, the minimum water content in summer to which the soil dries out is overestimated at 5, 15 and 40 cm depths in 2011 and 2013. On the other hand, in 2012 it is underestimated at 15, 40 and 80 cm depths.

Lastly, the simulated evapotranspiration pattern follows the potential evapotranspiration until approximately May in 2011 and 2013, after which it sharply decreases because of limited soil water availability.

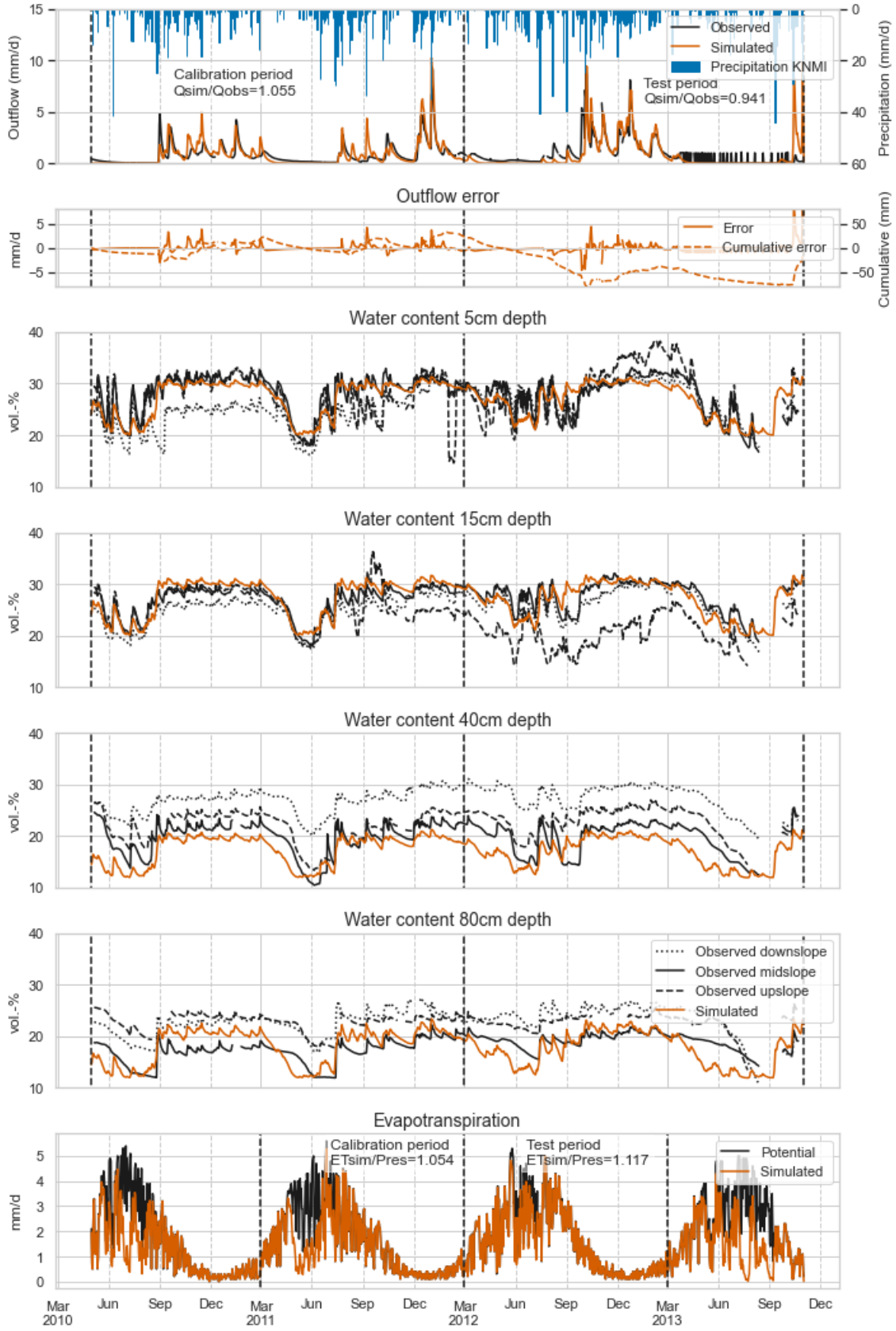

Figure 13: The daily observed and simulated outflow, water content at 5, 15, 40 and 80 cm depth and the simulated and potential evapotranspiration for the calibration and testing period. The outflow error is defined as the simulated minus the observed outflow.

5.2. Yearly water balance

Figure 14 shows the water balance for the test field on a yearly scale from 2010 to 2022. For each year the inflows are plotted besides the outflows. The storage change and error in the simulated outflow can be negative, compensating for a higher outflow than inflow. Figure 15 shows the different components of the balance relative to the yearly precipitation. A table with the exact values can be found in Appendix D.2.

Generally, the yearly precipitation comprises 770-970 mm with an average of 850 mm. In contrast, 2017 received almost 1100 mm. Moreover, 2010, 2016 and especially 2018 were exceptionally dry. In these years up to 75% of the precipitation was evaporated.

The storage change over a year is mostly negligible with a maximum magnitude of 50 mm per year.

The range in outflows from the CB is also relatively small with yearly amounts of 20-90 mm with an average of approximately 63 mm. This entails 5-10% of the yearly rainfall. Only 2012 has an exceptionally high CB outflow (165 mm). No strong correlation between precipitation and CB outflow can be inferred other than that years with low CB outflow were also dry years (Figure 16).

The CL generally discharges 30 to 35% of the yearly rainfall (250-320 mm, average 280 mm). In the wet year of 2017 this was more (400 mm) and in the dry year of 2016 it was less (170 mm). The yearly outflow correlates quite well with the yearly precipitation (Figure 16).

Furthermore, the evapotranspiration generally amounts to 450-550 mm per year. Depending on the precipitation amount this can be 50-70% of the total rainfall with an average of 60%.

Lastly, the error in the simulated outflow when compared to the observed outflow can be negligible (e.g. 2010, 2011) or considerable (2013, 2015) and yield up to 10% of the yearly precipitation.

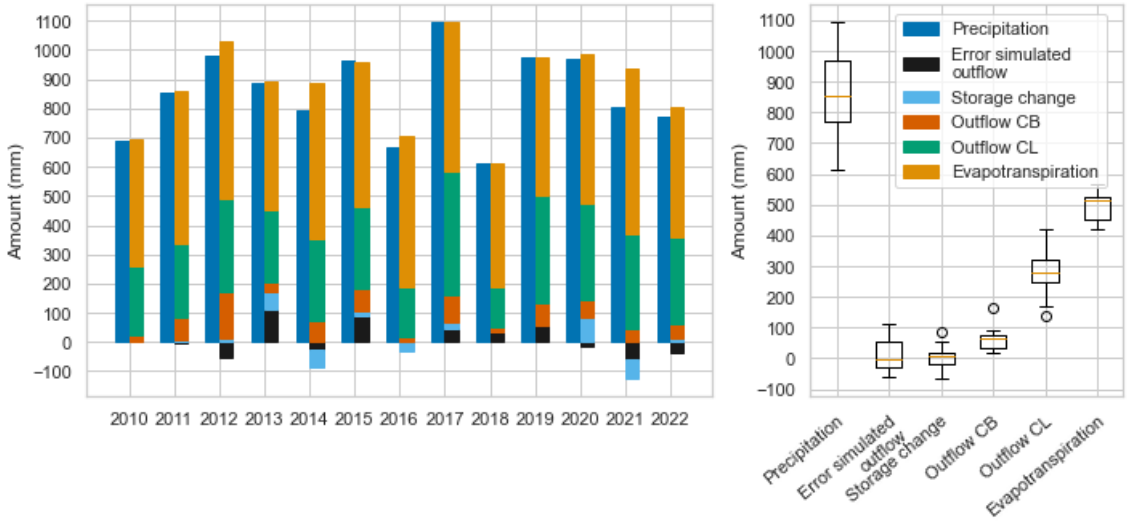

*Figure 14: Yearly absolute water balance. Left bar of each year are the inflows (precipitation), the right bar consists of the outflows. The right bar also contains the error in simulated outflow (defined as $Q_{sim} - Q_{obs}$) and storage change (defined as $S_{end} - S_{begin}$). These yearly values are summarised in boxplots on the right. Box spans first, second (orange) and third quartile which is the inter-quartile range (IQR). Whiskers extend to highest/lowest value within 1.5*IQR. Data beyond this range are plotted as points.*

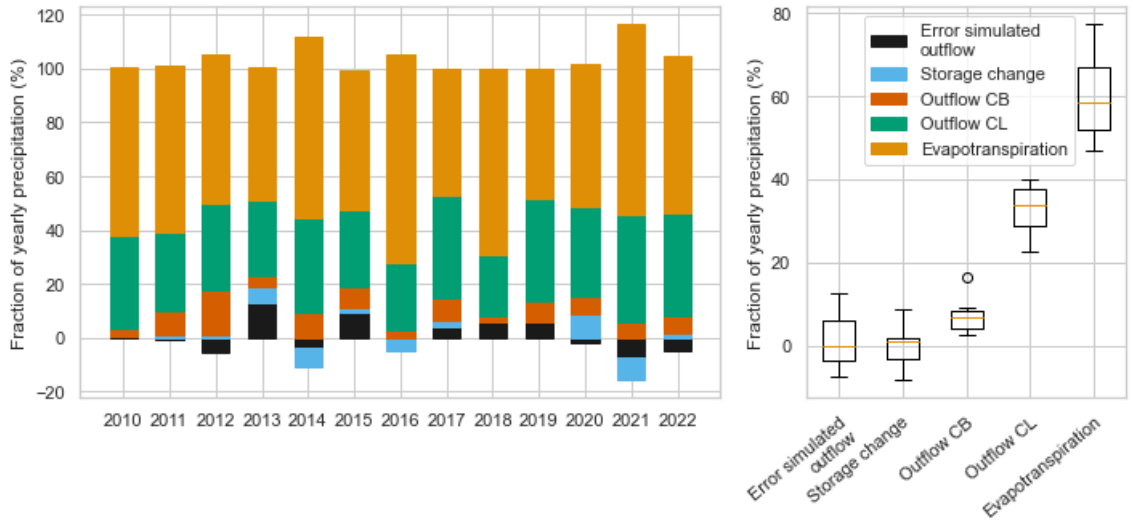

*Figure 15: Water balance relative to yearly precipitation. Box spans first, second (orange) and third quartile which is the inter-quartile range (IQR). Whiskers extend to highest/lowest value within 1.5*IQR. Data beyond this range are plotted as points.*

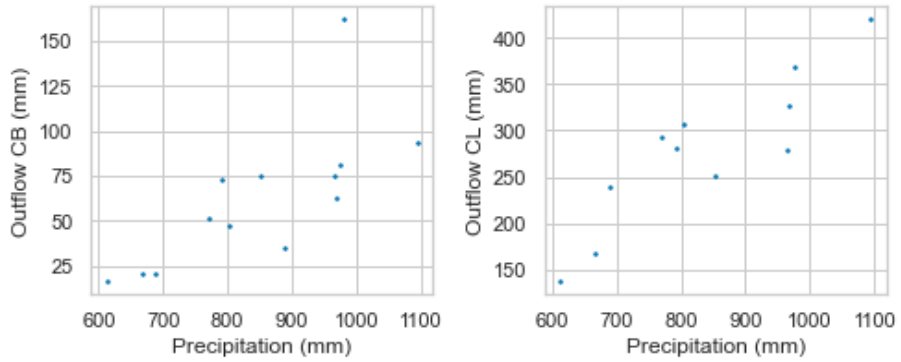

Figure 16: Scatter plot of yearly CB and CL outflow with yearly precipitation and average storage.

5.3. Seasonal water balance

The seasonal water balance over time is shown in Figure 13 of which exact values can be found in Appendix D.3. These are summarised in Figure 18. Spring receives the least precipitation compared to the other seasons. The spread in precipitation amount is the least in winter and the highest in autumn. Some years had exceptionally high and low precipitation in summer like 2012 (350 mm) and 2013 (100 mm), respectively.

A strong seasonal trend is visible in the evapotranspiration. It is highest in summer (approximately 200 mm) and lowest in winter (approximately 25 mm). In general, the variation within each season is less than 25 mm per season, except for summer where it is larger.

The estimated initial storage is generally close to the storage at PWP in summer and close to the storage at FC in winter and spring. In autumn it can range between the two options. The estimated change in storage is either stable or positive in summer, positive in autumn, stable in winter and negative in spring.

However, the error in simulated outflow is generally overestimated in autumn and winter, while in summer and spring it is underestimated. This means that the combination of estimated change in storage and evapotranspiration is too small in autumn and winter and too large in spring and summer. While this may be negligible for summer and winter, for autumn and spring it is a notable error.

Furthermore, the outflow from the CB happens mainly in winter (20-50 mm) and to a lesser extent in autumn (0-20 mm). The outflows from the CL follow a similar pattern but are higher overall with 110 to 180 mm in winter and 0 to 30 mm in summer.

Relation outflow to other water balance components

Figure 19 shows the scatter plots between seasonal CL and CB outflows with precipitation, initial storage, evaporation and the sum of these. The CB outflows show threshold behaviour with the other water balance components. Seasons with an outflow of more than 20 mm only happen when the seasonal precipitation is more than 150 mm, the seasonal evapotranspiration less than 100 mm and the initial storage is more than 220 mm, which is approximately the storage at FC. Combing those leads to the observation that for seasonal CB flows of more than 20 mm to happen, the sum of the initial storage and precipitation minus the evapotranspiration needs to exceed 400 mm. Generally, that happens in winter and autumn.

On the contrary, CL outflows do not show this threshold behaviour. Although high CL seasonal flows of more than 150 mm only happen with precipitation and initial storage higher than 150 mm, there is not a clear relation for lower precipitation and initial storage amounts. On the other hand, CL outflows decrease with increasing seasonal evapotranspiration. Furthermore, when plotting the sum of the initial storage, precipitation and negative evapotranspiration, a linear relationship with CL flows is apparent.

Figure 17: Seasonal water balance.

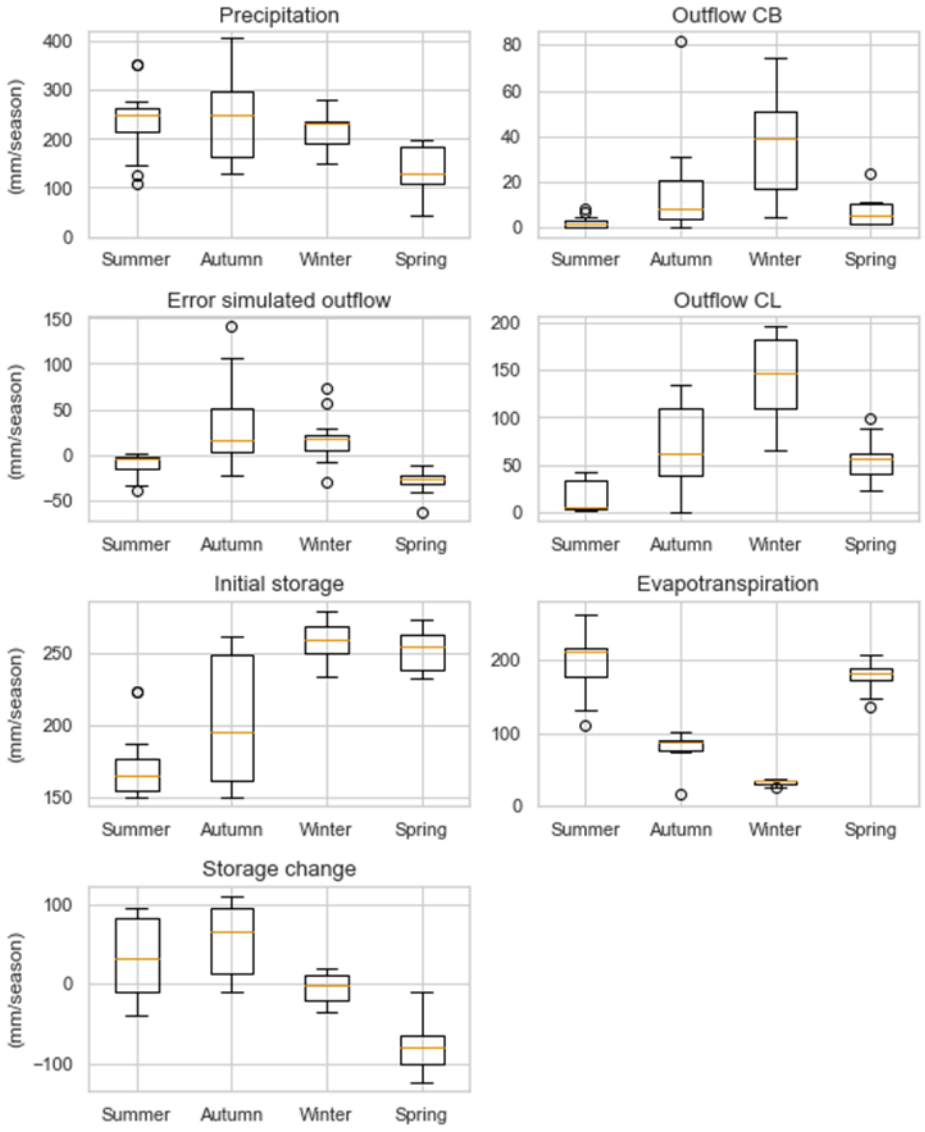

*Figure 18: Summary of magnitudes of components of the water balance on a seasonal time scale. Box spans first, second (orange) and third quartile which is the inter-quartile range (IQR). Whiskers extend to highest/lowest value within 1.5*IQR. Data beyond this range are plotted as points.*

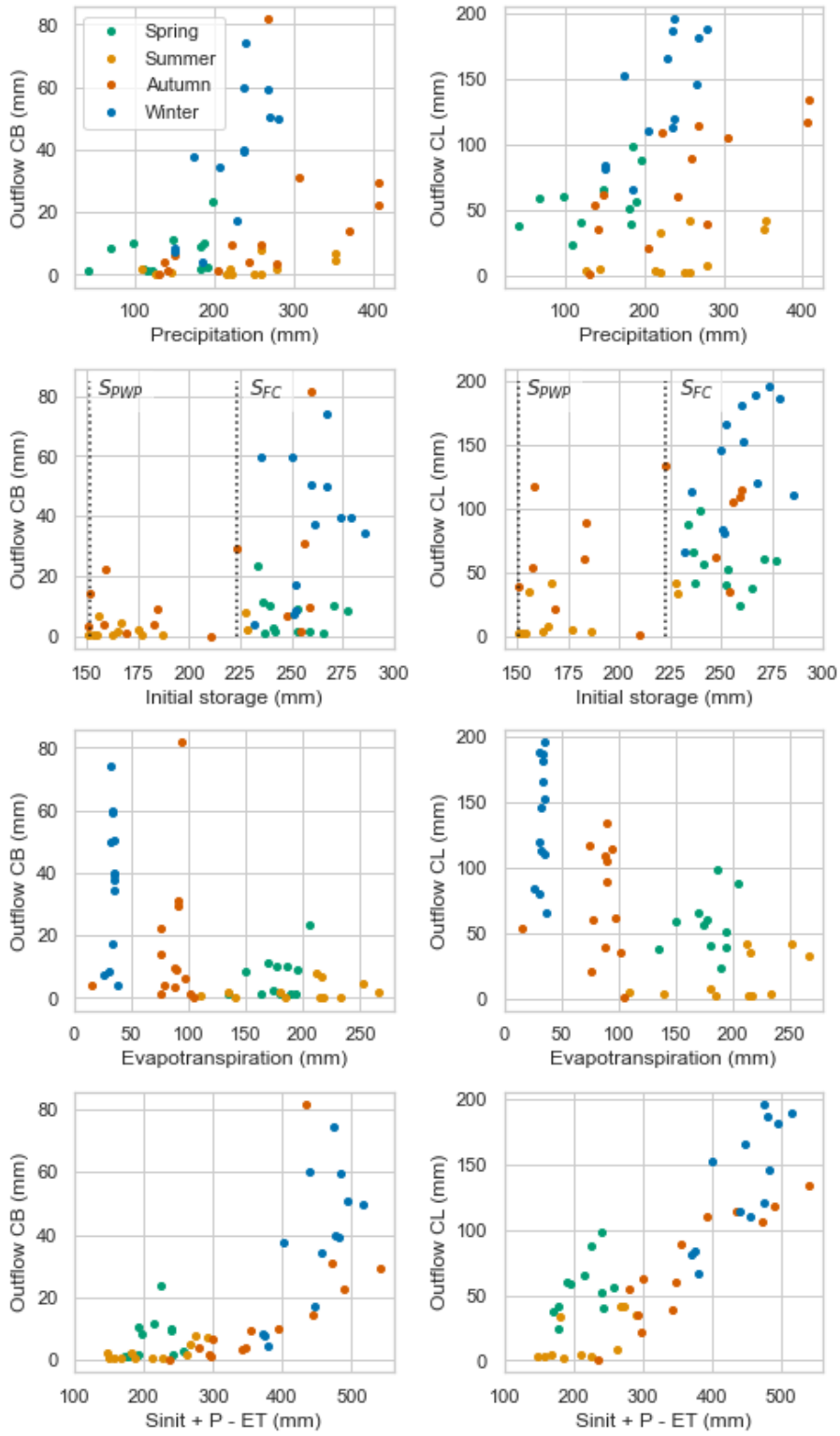

Figure 19: Scatter plot of the seasonal outflow from the CB and CL with seasonal precipitation, initial storage, evaporation and the sum of them.

5.4. Water balance at breakthrough

The water balance at breakthrough was analysed on a daily and seasonal scale. The daily water balance is shown in Figure 20. First of all, a similar pattern as for the calibration and testing period is observed, where the model outflows are underpredicted between March and September and overpredicted in the remaining period. This leads to a cumulative error in the simulated outflow of -180 mm in 2012 and 2013 and 150 mm in 2020 and 2021.

The storage pattern is similar each year with a storage of about 150 mm in the peak of summer and approximately 270 mm in winter.

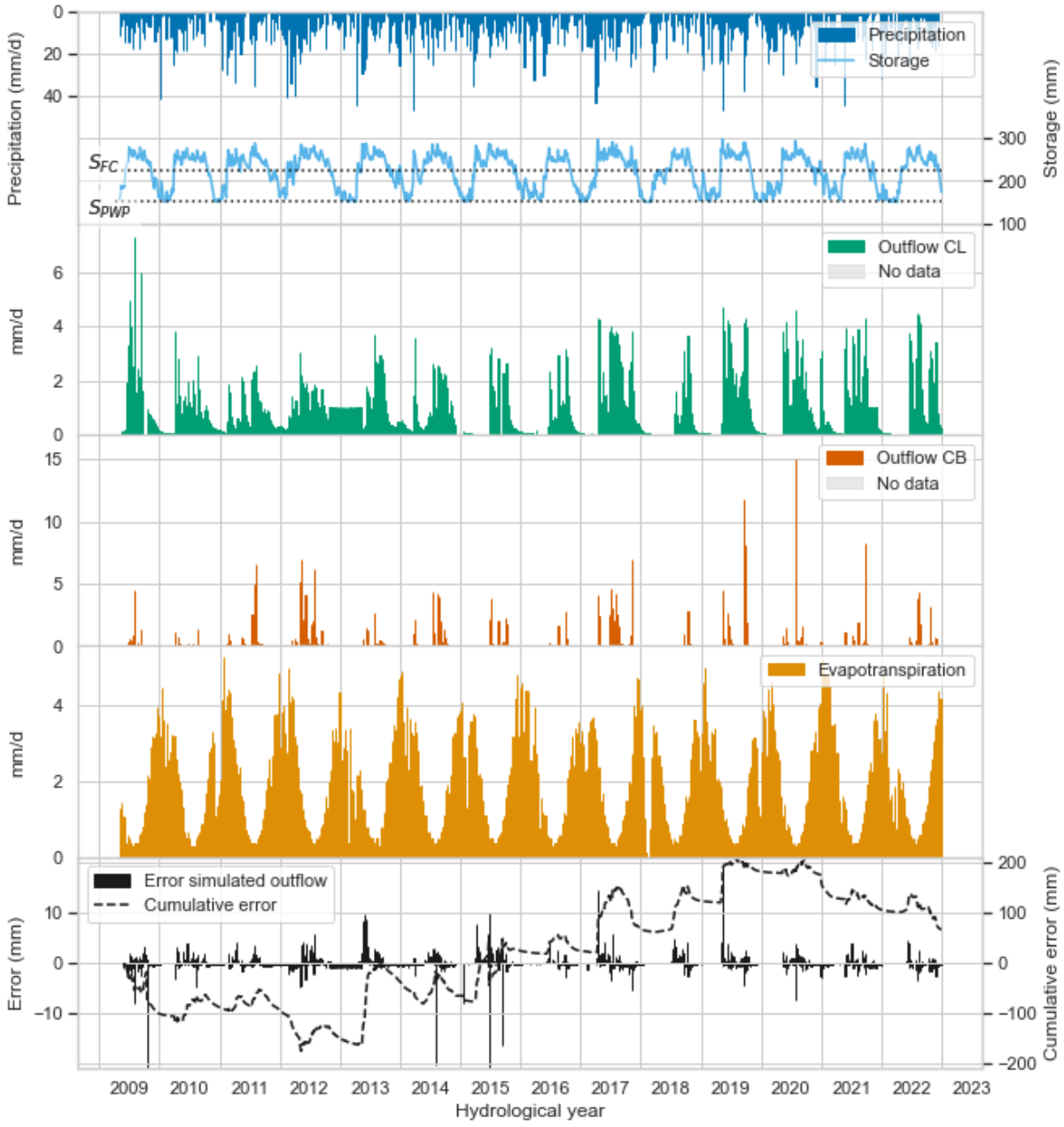

Figure 20: Daily water balance.

Moreover, the simulated evapotranspiration shows a similar unexpected pattern as in the calibration and testing period. The evapotranspiration is high in spring until the storage

reaches its minimum value after which the evapotranspiration decreases fast. 2018 is the most striking example of this behaviour.

CBS flow dynamics

The measurements of the CL and CB outflows show different dynamics. Generally, the peaks in the CB flow are higher. Also, the recession time afterwards is much shorter as compared to the CL outflows. Precipitation results in flow in both layers within 1 or 2 days, but recedes within a week for the CB whereas it takes more than 2 weeks for the CL flow to subside.

This effect is better visible in Figure 21 where the (cumulative) frequency and relative load functions for both outflows are plotted. The discharge from the CL has a maximum at approximately 4 mm/d and the flows lower and higher than 2 mm/d both make up for 45 and 55% of the total flow, respectively.

This is also true for the CB outflow but the relative importance of flows between 0 and 1 mm is higher (35% of the total flow). Also, flows larger than 1 mm/d occur only 5% of the time. However, flows of more than 4 mm/d contribute to 20% of the total flow and the maximum flow of CB is much higher (15 mm/d).

Apparently, the measured diversion capacity (4 mm/d) is much lower than it was designed for (20 mm/d). A possible reason for this is the observed change in GSD of the CB. The results of the estimation of the SWRC based on GSD following the method proposed by Zhai et al. (2020) using a 0° contact angle are shown in Figure 22. It shows that the estimated WEV of the CB in 2017 is a factor of 10 smaller than in 2009 and comparable to the WEV of the CL.

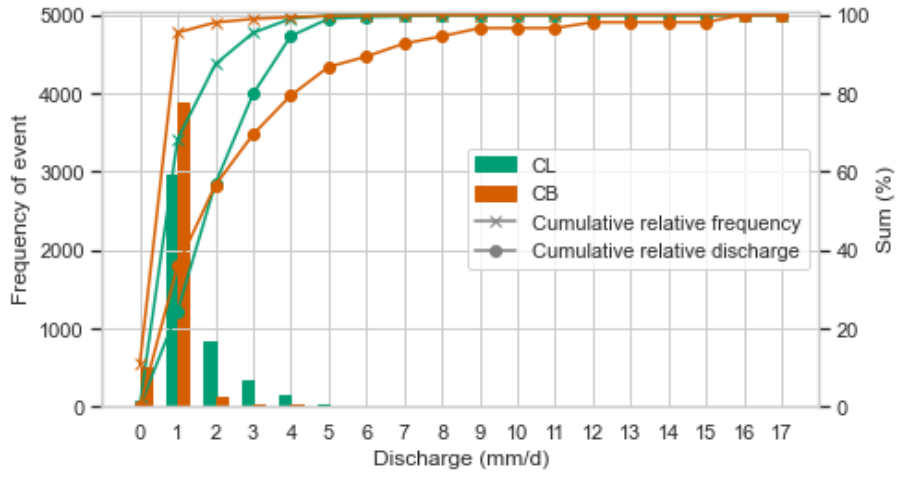

Figure 21: Frequency distribution and share of each outflow bin in total outflow. Bins hold all measurements within the previous bin value and its own value.

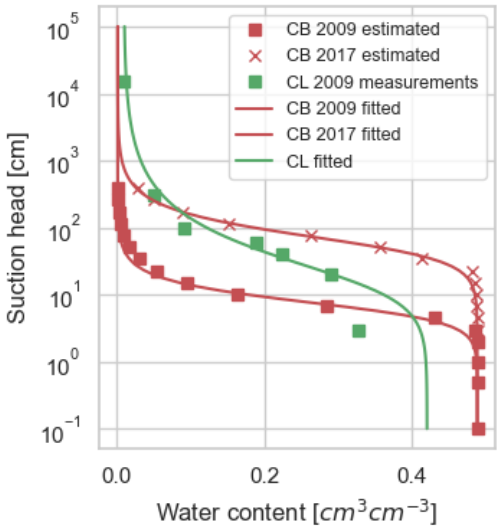

Figure 22: SWRC of the CL and CB in 2009 and of the CB in 2017. Estimated points were derived based on the method proposed by Zhai et al. (2020) *using a 0° contact angle. The estimations and measurements were subsequently fitted using the RETC software* (van Genuchten et al., 1991).

Relation outflows to other water balance components

The scatter plots of the CL and CB outflows with precipitation, initial storage and evapotranspiration on a day are presented in Figure 25. Appendix D.4 shows the same plots with the daily data filtered per season. Apparently, high precipitation does not lead to high outflow. It is even the reverse, as the highest outflows happen at relatively lower amounts of precipitation. Taking into account the precipitation of up to 7 preceding days did not change this result.

However, there seems to be a relationship between the initial storage and both the CL and CB outflow on a day. CB outflow starts generally when the initial storage is larger than 225 mm, which is in the range of the estimated FC, and becomes larger than 1 mm/d at approximately 250 mm of initial storage. The largest CB outflows happen at an initial storage of more than 270 mm. The CL outflow has similar pattern. There can be CL outflow even when the initial storage is at its lowest (150 mm). For higher initial storages of the storage at FC (230 mm), CL outflows are possible of more than 1 mm/d.

Figure 23 presents the outflows of the CL and CB plotted against each other. In general, CB outflows coincide CL outflows between 1 and 4 mm/d. However, there is no clear relationship between CL and CB flows within this range, although the highest CB flows of more than 8 mm/d only occurred when the CL was at its maximum capacity. It is also not possible to predict the outflows based on the initial storage itself as high storage can still coincide with low flows. Including precipitation and evaporation in the bottom two scatter plots in Figure 25 doesn't change this outcome.

To understand what might be reasons for this behaviour, the events for which the daily CL flow was more than 4 mm/d on the one hand and the events for which the CB flow is larger than 1 mm/d while CL flow is less than that on the other hand are shown in Figure 24 on hourly time scale. The daily precipitation on November 4th, 2012 is less than the precipitation on

December 25th, 2009 and February 2nd, 2010, but it is more concentrated. However, the storage is comparable between those dates. Therefore, the difference in CL and CB outflow might be attributed to the distribution of precipitation over the day. In these cases, intense rainfall resulted in high breakthrough, whereas a stable uniform precipitation pattern increases the CL flow.

On a side note, it was also analysed how the CL and CB flow reacted to short and intense precipitation events in summer when storage was below FC. It appeared that during such events there was no flow from the CBS (Appendix D.4).

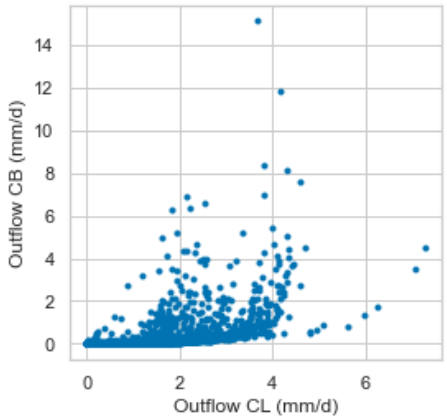

Figure 23: Scatter plot of daily CL and CB outflows.

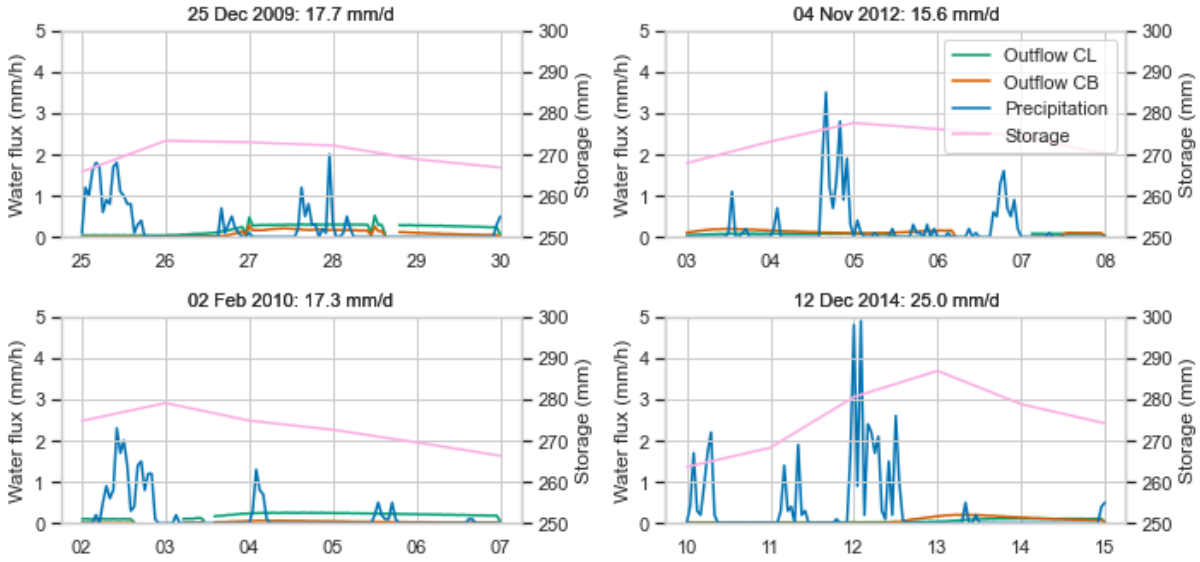

Figure 24: Four events showing two extreme situations. Two events on the left have high CL outflow (> 4 mm/d) but low CB outflow (< 5 mm/d). The two events on the right have high CB outflow (> 1 mm/d) while CL outflow is less than 1 mm/d.

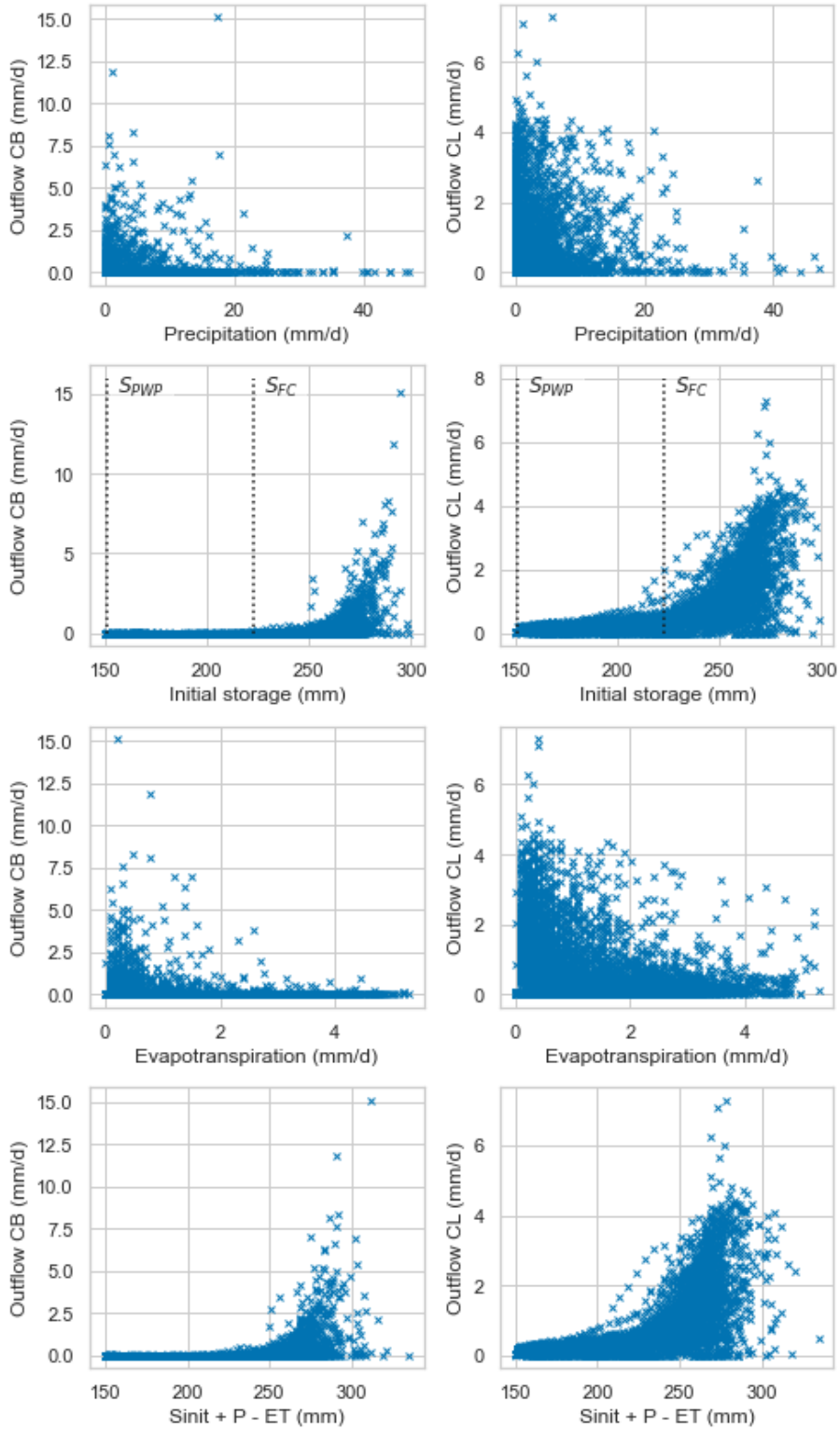

Figure 25: Scatter plots between daily CL and CB outflows on the one hand and storage, precipitation, evapotranspiration and their sum on the same day on the other hand.

6. Discussion

6.1. Model limitations and validity

6.1.1. Limitations

There are limitations in the calibration result. When assessing the final model parameter set it should first be noted that the soil properties are likely to be different along the slope and at each depth. As explained in Appendix C.6.4, the parameters of the TS and SS were chosen such that a balance could be found between the two measurements series in each of them, meaning that these parameters are describing more average behaviour. Ho & Webb (1998) stated that this might be a valid approach when aiming to model the average behaviour of a CBS system, but that the dynamics due to preferential flow are lost.

Moreover, these parameters were considered constant over time, whereas they vary within a year and over time. For example, soil properties are altered by biological and physical processes. An example of a systematic change in water content is visible in the difference in the mid-slope FC at 80 cm depth, between the of 2010 and 2012. After an infiltration peak, the water contents move back to a lower water content in the first period compared to the second period. This could be caused by an increase of organic matter over the years by the development of roots. Moreover, temperature, which varies over the year, affects the viscosity of water and consequently the hydraulic conductivity. Similarly, vegetation properties like root density change between different years and within a year (Feddes & Raats, 2004) and were significantly changed during the reconstruction in 2013.

Also, the adjustment of the CL soil properties to incorporate lateral flow dynamics of the CL and CB resulted in an increase in simulated water contents in the layers above. These were compensated for by changing the parameters of the concerned layers, which introduces a systematic bias.

Lastly, the used data from the KNMI station for potential evapotranspiration and in particular the precipitation data can distort the results because they are from a station located 16 km away from the test field. Moreover, there can be an error up to 20-40% in the calculation of Makkink potential evaporation data, rendering it only valid for use at the yearly timescale (Spieksma et al., 1995).

6.1.2. Model testing

Testing the model resulted in three major discussion points. First, the modelled outflow pattern was rising and receding too fast after the onset of a flow event when comparing with observed outflows. This resulted in a general overestimation of flow between September and March and underestimation between March and September. Also, the cumulative error in the simulated water balance can be up to 10% of the yearly rainfall. Secondly, the dynamics in the water content were uniform over the all soil layers, whereas the observed water contents show a dampening of fluctuations over depth. The more dynamic behaviour at the surface could not be replicated and the SS dries out earlier than observed. Thirdly, the simulated evapotranspiration shows a rather abrupt transition by going from potential rates to severely moisture limited rates.

Concerning the first point it should first be noted that the observed outflow is the sum of two outflows (CL and CB) which both have different dynamics. Secondly, this flow happens in a different direction than the flow in the one dimensional model. Flow distances and hydraulic properties of the CL are likely to be different in this direction (Zhan et al., 2014). Although it was tried to adjust the properties of the CL to reproduce the outflow better, it cannot mimic two different outflow regimes in a different dimension.

Furthermore, the difference in peak height can partly be explained by the difference between the local precipitation and the precipitation used for the model (Appendix D.1.2). For example, the modelled outflow at the end of the testing period (November 2013) was higher than the observed outflow due to higher precipitation at the KNMI Berkhout station than at the test field. Nonetheless, this was not always the case, as two events in in August 2012 with higher precipitation in Berkhout than measured by Pluvio-2 did not result in higher simulated outflows.

The second point is possibly caused by three model choices: the modelling of the soil as three homogenous soil layers, the choice of SHCC model and the assumption that there is only vertical flow in the MOL. The limitation of the first assumption is that this does not account for varying soil properties over depth and soil aggregation with associated preferential flow. Cracks ranging from the surface into the CBS are unlikely because no flow was observed during high intensity precipitation events in summer when the soil is dry. However, the excavation in 2013 showed that the soil had formed aggregates, possibly because of its relatively high organic matter content.

Secondly, the chosen SHCC model of Averjanov with $n = 3$ probably does not perform well at higher values of suction head. The measurements shown in Appendix C.6.1 also show that the unsaturated hydraulic conductivity is overestimated. Differences in suction head, caused by precipitation or root water uptake, are compensated by relatively quick infiltration or capillary rise and redistributed over the entire soil profile. This is also the reason why changing the root distribution function does not have an effect on the water contents at different depths (Appendix C.6.3). If the hydraulic conductivity would decrease faster with increasing suction head, differences in suction head would not dissipate fast. This would lead to more dynamic water contents in the TS and less drying out of the SS in Spring.

Thirdly, the assumption that there is no lateral flow in the MOL is likely to be false. The water content at 40 cm depth is higher downslope than mid- and upslope. Also, the water contents at 80 cm depth are more dynamic than mid- and upslope, which could indicate lateral flow.

The first two reasons given in the previous paragraph also possibly explain the transpiration behaviour of the model. The estimated transpiration is likely to be too high initially in spring and too little afterwards. Indicators for that statement are the premature drying of the SS, the unrealistic drop in transpiration in summer and the underestimation of outflow between March and June. Moreover, the model overestimates the minimum water content at various depths around June in a dry year, indicating that it underestimates the transpiration at that time. A SHCC should be chosen such that the root water uptake in the top layers cannot be

fully compensated by capillary rise. This would decrease the transpiration due to moisture limitations earlier and the SS would start to dry out later.
Moreover, given that the model overestimates outflow in autumn and potential evapotranspiration is low during this season, the model probably underestimates the storage. A possible reason for this could be that the model is calibrated to the mid-slope water contents. However, the observed water contents at 40 and 80 cm depth are higher up- and downslope than mid-slope. Using the mid-slope storage to estimate the storage of the complete test cell is therefore invalid and likely to be an underestimate.

6.1.3. Effect on results

To summarise, the model performs reasonably well concerning storage and outflow in summer and winter but is less reliable in its estimations of storage, evapotranspiration and outflow in spring and autumn. In spring the estimated storage and outflow should be higher and evapotranspiration lower. In autumn precipitation events should be reflected in more storage rather than outflows. Also, it is likely that the modelled storage is not representative of the storage in the complete test field. Additionally, evaporation estimates in summer are generally too low as well. As the uncertainty in the Makkink potential evaporation is also high, this means that the daily storage and evapotranspiration estimates cannot be trusted.

This influences the yearly and seasonal water balance because the storage in June might be different than currently simulated. As evapotranspiration should be less strong, the influence of the precipitation in spring should be higher, which could result in a larger variability in storage in June. This could lead to a different change in storage over a hydrological year. Also, the unexpected gap in seasonal initial storage between 180 and 225 mm in Figure 19 would likely not exist.

Furthermore, the correlations on daily scale between storage and CL and CB outflow are affected by the aforementioned uncertainty in storage in autumn and spring. The storage in these seasons determine the correlation as in these seasons the storage ranges between the storage at PWP and FC (Appendix D.4). As these storages are likely an underestimate, the relation between storage and outflows should be more shifted towards higher storages. However, it is unknown whether the shape of the correlation between storage and CBS outflows would be different, also considering that simulated flow dynamics behave too abruptly.

6.2. Yearly and seasonal water balance

On a yearly scale, approximately 60% (500 mm) of the precipitation evaporates, 30-35% (250-320 mm) is diverted by the CBS and 5-10% (20-90 mm) breaks through. Other test fields located in Germany under similar climatic conditions have similar evaporation (Giurgea et al., 2003; Melchior et al., 2010).

Moreover, the field situated in Hamburg had a cover design with an infiltration control layer (glacial marl) and drainage layer on top of the CBS. Consequently, the flows from the CL and CB were lower than observed at the test field in this study. Even after the formation of cracks in the infiltration control layer, the CL and CB flow amounted to 145 mm (17% of yearly

precipitation) and 16 mm (2% of yearly precipitation) per year on average, respectively (Melchior et al., 2010). Two test fields located in Karlsruhe showed similar performance. The first field also had an infiltration and drainage layer built on top of the CBS whereas at the second field the cover above the CBS consisted of a thick layer of soil (2 m) together with a drainage layer. The CL outflow for the first and second field yielded 13-19% and 12-30% of the yearly precipitation, respectively. Furthermore, the CB outflow amounted to 1-2% for the first field and 0.5% for the second field.

Additionally, a test field in Quebec, Canada, also showed relatively little breakthrough (7-36 mm per year) (Abdolahzadeh et al., 2011a). Precipitation at this location is even higher (approximately 1200 mm/y) and evaporation lower (300-400 mm per year) (Wang et al., 2013). This test field also had a configuration with an infiltration control layer on top of the CBS.

Moreover, current legislation in the Netherlands requires the breakthrough of alternative liner systems to be equal or less than the seepage through the current liner system, which is assumed to be 5 mm per year (Ministerie van VROM, 1991). In comparison, German legislation demands the breakthrough through a liner system constructed from mineral materials to be less than 20 mm per year over a period of five years (Deponieverordnung, 2009)

Compared to these studies and regulations, the breakthrough at the test field in the Wieringermeer is relatively high. This can be attributed to the difference in cover soil. The MOL has much higher saturated hydraulic conductivity (up to a factor of 10^3) than the infiltration control layers in the studies mentioned above. This can result in a higher infiltration rate, which is one of the controlling factors of CBS performance (Aubertin et al., 2009; Berger, 2018). The flow pattern of the CL and CB in this study change faster and are of higher magnitude than observed by Giurgea et al. (2003). In other words, the CBS in this study is more affected by the (variance in) precipitation as the cover soil buffers and dissipates the infiltration input less.

Furthermore, the high number of days with small CB flows indicate that there is always a little breakthrough. This is in line with what was found in the laboratory where uniform seepage through the CB was observed (Kämpf et al., 2003). Also, Scarfone (2020) discovered the importance of liquid film flow at ranges of high suction head. Liquid film flow is the flow of water through the thin liquid films that cover the soil particles and the meniscus water bridges between them. Another reason for the low amounts of breakthrough might be heterogeneities in the CL, caused by the formation of soil structure, clogging by iron precipitates (Appendix B.6.3) or construction errors. These induce preferential flow and can significantly increase breakthrough (Ho & Webb, 1998). Lastly, dissipation of the CBE due to ingress of sand into the CB can also be a cause (see section 6.4). These reasons for small CB flows are hard to prevent. As these flows yield 35% (on average 20 mm per year) it is unlikely that breakthrough could be reduced below that amount.

On a seasonal time scale, the outflow from the CL and CB follow a pattern opposite to the evaporation. The outflows are highest in the season with the least evaporation (winter) and lowest in the season with highest evaporation (summer). This is in line with what others stated: the performance of a CBS depends on both the evaporation (in this case from the layers on top) and the diversion capacity (Khire et al., 2000; Stormont, 1996). In a climate with a seasonal

trend in evaporation, lateral diversion is most dominant in seasons with low evaporation. A similar pattern with high CL and CB flow in winter was observed by Giurgea et al. (2003). Aubertin et al. (2009) explain the high breakthrough during this period by the accumulation of moisture in the CL which decreases the diversion length.

After winter, the season with the highest CB flow is autumn. This season is characterised by the largest spread in precipitation and initial storage. Also, most of the years with breakthrough of more than average had also high breakthrough in autumn (2012, 2015, 2017 and 2019) with 2011 and 2014 being the exception to this rule. Accordingly, autumn can be described as the most critical season due to its spread in hydrological conditions and potential to influence the yearly breakthrough amount.

6.3. Water balance components driving CBS flow

As described in the previous paragraph, both CB and CL flows decrease with increasing evapotranspiration, both on seasonal and daily time scale. For CL flow the spread in possible seasonal and daily flows for a given evaporation rate is still high, however, especially at lower rates. Concerning CB flow, there seems to be a threshold around an evaporation rate of 1 mm/d or 50 mm per season after which CB outflow can become larger than 1 mm/d or 40 mm per season.

Regarding precipitation, the relation is less obvious. On a yearly scale the CL outflows have an approximate linear relation with precipitation. A possible explanation is that more than half of the yearly precipitation falls in autumn and winter, which are also seasons with high CL flow. On a seasonal scale the relation between precipitation and CL flow is less evident, although precipitation of more than 200 mm per season is necessary for CL flows of exceeding 100 mm. On a daily scale there is no relation visible. This could partly be explained by the time lag between a precipitation event and an increase in CL outflow which can be multiple days (Figure 24) and the precipitation data that was used. Also on a seasonal level, it takes months for the CL flow to subside after winter, which makes the outflow in spring more related to the precipitation in winter than in spring itself.

The relation between precipitation and CB outflow is similar to its relation with CL flow, with a weak linear relationship on a yearly time scale, a necessity of seasonal precipitation to be more than 150 mm for high CB flows (>20 mm) to occur and decreasing breakthrough with precipitation intensity on a daily scale.

In contrast, Berger (2018), observed a linear increase of CL flow with increasing irrigation rate in a 10 m test setup in a laboratory. After a certain threshold, this outflow remains constant and instead the CB outflow starts to increase linearly with irrigation rate. However, this relationship concerned steady state conditions, where the role of changing moisture storage in the soil is irrelevant. Also, the experiment concerned a bare CBS without a cover soil on top. The latter is also true for what Scarfone (2023) found, using a numerical study, that for a CBS which uses a fine sand as CL as in this study used, the intensity of a rainfall event strongly influences the performance of the CBS. Lastly, Zhan et al. (2014) also observed different breakthrough patterns when comparing a rainfall event of 2 mm/h to 70

mm/h. However, these type of conditions are more likely in a tropical climate and rarely happen in a temperate climate as in this study.

Therefore, under the climatic conditions and cover design in this study, the available storage in the soil cover and CL is more likely to be the determinant if a precipitation event will produce breakthrough, especially on seasonal and daily time scale. This was also observed by Stormont (1996). The correlation plots show clear threshold behaviour where CB flows start to becomes noticeable when the storage in the complete cover exceeds the storage associated with FC conditions on a daily scale. On a seasonal scale the CB behaves similarly, where CB flows of more than 20 mm only occur when the initial storage that season is more than the storage at FC.

The relation between storage and CL outflows is similar but less clear. In general, on a daily scale CL flows higher than 1 mm/d only occur at an average storage of more than the storage of the soil at FC. On the contrary, there can be CL flows even if the available storage is below the storage associated with FC. This phenomenon can be the result of the likely underestimation of the storage by the model or by the difference in storage along the slope. While the average storage might be below FC, the downslope areas might be wetter, producing CL flow. Furthermore, on a seasonal scale initial storages of more than the storage at FC always produce CL outflows of more than 25 mm. However, high outflows can also happen in seasons with low initial storage, which could be attributed to high precipitation during that season.

Therefore, when summing the initial storage, precipitation and negative evapotranspiration on a seasonal scale, a linear relation becomes apparent. For CB flow the relation with these summed water balance components shows a threshold around 400 mm per season, at which the breakthrough is most of the times higher than 20 mm.

High precipitation in seasons with high initial storage can result in high breakthrough amounts. Besides the winter seasons in general, the most notable case of this is the year 2012. Compared to 2017, the annual precipitation amount is similar, but the breakthrough in 2012 is much higher. This can be explained by the exceptionally high precipitation in summer. Consequently, the storage in autumn was well above the storage at FC when autumn started. Combined with the high precipitation the same season, this lead to high breakthrough. 2017 on the other hand, had a dry summer, so the high precipitation in autumn could be stored and did not result in high CB flow.

The reverse is also true. Years with relatively low CB flow like 2010 and 2016 were years with relatively little precipitation in winter, which is the season with generally high initial storage.

On a daily scale, the pattern of the sum of water balance components with CB outflow remains comparable to the storage plot. Unexpectedly, a relatively high sum of water balance components can still produce relatively low CL or CB flows. In general, this might be explained by the model error in storage estimations in autumn and spring which cause these high storages in situations with no flow (Appendix D.4). Alternatively, as shown in Figure 24, the distribution of precipitation over a day with a similar storage can lead to different CBS

responses. If the same daily precipitation falls in a shorter timeframe, CB flows can be much higher than the CL flows. Conversely, if the precipitation pattern is more uniform over a day, CL flow is higher than CB flow.

6.4. Difference measured and design diversion capacity

The diversion capacity for the CBS under study was designed as 20 mm/d. The daily outflow data, however, suggest that the maximum CL outflow is approximately 4 mm/d. This discrepancy might be explained by the ingress of sand from the CL into the CB as was observed in 2017 which decreases the CBE. Its possible impact is presented in Figure 22, showing that the deposition of sand particles decreased the WEV of the CB with a factor of 10, making it similar to the WEV of the CL. This is unlikely however and might be caused by the assumed contact angle of 0°. When taking a higher contact angle all suction heads of the SWRC estimations are multiplied by a factor of $\cos(\alpha)$, with α the contact angle between the water meniscus and the soil particles, effectively moving the graph downwards. However, the factor 10 difference between WEV of the situation in 2009 and 2017 remains. Many studies on the performance of CBSs stress the importance of the WEV as it controls the point of breakthrough (e.g. Khire et al., 2000; Stormont & Anderson, 1999; Yang et al., 2004). Moreover, Rahardjo et al. (2013) state that there should be at least a factor of 10 difference between the WEV of the CB and the CL. Furthermore, the performance is also extremely sensitive to the SHCC of both layers (Kämpf et al., 2003), which for the CB is also considerably changed by the deposition of sand.

Another reason might be heterogeneities introduced during construction. One of the excavations in 2013 reported that the topsoil at the bottom of the slope was 45 cm deep instead of the designed 20 cm. These kind of errors might affect the diversion capacity. Since no gradual decrease in diversion capacity was observed, this might be a good explanation as well.

Moreover, the ambient temperature might also be of influence, given that most breakthrough happens in winter and colder temperatures decrease the diversion capacity (Kämpf et al., 2003; Kämpf & Montenegro, 1997). However, this effect is not strong enough to explain the total decrease in diversion capacity.

Lastly, the diversion capacity is similar to the capacity measured at the first test field in Karlsruhe which amounted to approximately 3 mm/d (Giurgea et al., 2003). This CBS was also made from a fine sand on top of a gravel, but details on the GSD were not given.

The fact that there is already breakthrough before the diversion capacity was reached, was also observed by other researchers (Kämpf et al., 2003). Flow from the CL in the CB happens preferentially, which is dependent on the local soil properties. Heterogeneities and also the uneven moisture distribution along the slope can therefore induce breakthrough earlier than expected (Ho & Webb, 1998).

7. Conclusion

This study aimed to describe the water balance of a test field located on the landfill in the Wieringermeer, the Netherlands. This test field was constructed to evaluate the design of a landfill cover in which a microbial methane oxidising system (MMOS) and a capillary barrier system (CBS) were combined. This study focuses on its performance regarding the diversion of infiltrating precipitation. The goal was firstly to describe the yearly and seasonal water balance and secondly to describe the composition of the water balance that lead to breakthrough on a seasonal and daily time scale.

Between 2009 and 2023 the precipitation and the outflows from the capillary layer (CL) and capillary block (CB) were measured. These observations, combined with water content and soil properties measurements, were used to simulate the evapotranspiration and the change in water storage over the years. A one-dimensional finite difference model was built using the Python *scipy* library which solved Richards' equation over a cross section of the cover. Soil properties were approximated using the Van Genuchten and Averjanov models. Moreover, evaporation was lumped into transpiration which was estimated using the Makkink potential evapotranspiration estimates, an exponential root model and a function for reduction due to available moisture. The model was calibrated manually by aiming to match the dynamics of the measured outflow and water contents.

Although the model describes the seasonal trend in water contents and outflows reasonably well, it has a relatively high error in its estimations of the evapotranspiration in spring and storage and outflow in autumn. In general, the evapotranspiration in spring and the outflow in autumn are overestimated which results in an underestimation of storage in these seasons. Reasons for this are most likely the missing dynamics of lateral flow in the model, the assumption of three uniform soil layers and the models to predict their soil water retention and hydraulic conductivity curves (SWRC and SHCC, respectively). Moreover, the rather simple model structure cannot accommodate for a change in its parameters over the years or for processes like soil hysteresis. Also, the estimated storage is likely an underestimate of the storage of the complete test field in general, based on the water content observations. Therefore, the models' simulations are a sufficient indication of the water balance of the test field, but improvements are necessary to support strong inferences.

The results show that the yearly precipitation between 2009 and 2013 ranges between 770 and 990 mm. On average, 59% (494 mm) of this precipitation is evaporated, 33% (281 mm) is diverted by the CBS and 7% (63 mm) breaks through. The CBS hence effectively diverts on average approximately 80% of the yearly precipitation surplus. Compared to other test fields and design standards, this breakthrough is high. This can be attributed to two reasons: a weakened functioning of the CBS and the properties of the cover soil.

Concerning the first, the diversion capacity of the CBS (4 mm/d) appeared to be lower than designed for (20 mm/d). The most likely reason for this phenomenon could be the observed ingress of sand from the CL to the CB, which decreased the water entry value (WEV) of the latter. Furthermore, the construction methods in the field might also cause heterogeneities and irregularities in the soil layering, which can also be a reason why the

diversion capacity is different from how it was designed. This would also explain why the diversion capacity was lower already from the beginning of the observation period.

Another reason for the higher breakthrough in this study as compared to other studies is the properties of the cover soil. This soil was optimised for methane oxidation and has consequently a relatively high hydraulic conductivity. Accordingly, infiltration through this soil into the CBS can be high, which leads to overloading of the CBSs' diversion capacity.

Besides these factors in the design and implementation of the CBS, climatic factors also affected the performance of the CBS. The results show that for breakthrough to occur, the storage in the cover soil and the CL should be higher than the storage at field capacity, both on daily and seasonal scale.

This storage is affected by precipitation and evaporation. Evapotranspiration decreases the water contents in the cover soil, which increases the capacity of the soil to buffer precipitation. It shows a clear seasonal cycle where it is low in winter and high in summer. On the other hand, precipitation amounts are similar each season, except for spring, where it is lower. Therefore, the outflows from the CL as well as the CB show a pattern opposite to the evaporation cycle with relatively high flows in winter and low flows in summer.

Therefore, no relationship between precipitation and outflows was found on a seasonal and daily level. It depends on the storage in the cover and whether it is at field capacity. However, even if the soil is at field capacity, precipitation does not necessarily lead to breakthrough. For that to happen, the distribution of precipitation also matters. The results on a daily scale show a typical exponential threshold between the sum of storage, precipitation and negative evaporation on the one hand and the CL and CB outflows on the other hand. However, there are also days where a high sum of these components does not result in high CB or CL outflows. Besides the error in the simulated daily storage, this can also be explained by the distribution of precipitation, as short and intense rainfall produces more relatively more CB than CL outflow. In the case of more evenly distributed precipitation over a day, CL outflows increase much more.

Furthermore, a high annual breakthrough amount can be caused by relatively high precipitation in winter or breakthrough in autumn. The latter can be characterised as the most critical season, as breakthrough amounts can range from practically zero to 80 mm. This depends on the storage available at the beginning of the season, which in turn depends on the precipitation in late summer.

Concluding, the performance of the test field in deviating infiltration is promising and could become satisfactory with some adjustments. These could involve improving the CBS itself or the cover soil, thereby also considering prerequisites for methane oxidation.

8. Recommendations

8.1. Improvements landfill cover design

Although the CBS currently already diverts 80% of the precipitation surplus on a yearly basis, it could be further improved.

Firstly, the design of the CBS could be adjusted. A lower permeable infiltration control layer on top of the CBS would improve its performance as shown by others (Abdolahzadeh et al., 2011b; Giurgea et al., 2003; Melchior et al., 2010). However, besides the tendency of such a layer to deteriorate due to soil cracking, it would also inhibit the functioning of the MOL by limiting oxygen diffusion and uniform upward gas migration because of its high moisture retention. Another option would be a design with a double CBS (Rahardjo et al., 2016; Scarfone et al., 2023). However, moisture retention in a second CL would likely further enhance the observed upward landfill gas migration, which would increase the upslope methane load and emissions. An extra drainage layer on top of the CBS as proposed by Giurgea et al. (2003) and Zhan et al. (2014) would likely produce the same effect because of a potential capillary barrier effect between the cover soil and the drainage layer.

Therefore, a simple solution would be to increase the thickness of the MOL. Aubertin et al. (2009) showed that this can improve the performance of a CBS up to approximately 1.5 m. Increasing the depth of the MOL could increase its storage, provided that it is accessible by plants. The additional storage could prevent the breakthrough events in autumn. Besides, a thicker layer would also dampen infiltration peak loads to the CBS more, although this mostly depends on the hydraulic conductivity of the MOL.

Additionally, the diversion capacity of the CBS could be improved by limiting the ingress of sand into the CB. When designing a CBS, the filter stability should be taken into account more conservatively, especially considering a CBS should be more durable than the current liner system. Nakafusa et al. (2011) tested a CB material consisting of crushed shells that performed well and also showed little ingress of sands in the laboratory. The decrease in diversion capacity could also be explained by inefficiencies introduced by the construction methods at large scale.

In any case, the decrease in diversion capacity shows the sensitivity of a CBS to processes on a larger spatial and temporal scales. These influences would become more important when a CBS would form the liner system of a complete landfill. Therefore, a decrease in diversion capacity as observed in the lab and in this test field could be inevitable, making other design improvements like a thicker cover soil more robust.

8.2. Improvements model

The model could be further improved to more accurately describe the water balance. In particular, improvements in the models' behaviour in spring and autumn could strengthen the inferences made in this study. There are two main improvements that could be done for the model. Firstly, the model used for the SHCC should decrease faster at higher values of suction head. The power variable n in the Averjanov model could be increased or a different model could be used. The Mualem-Van Genuchten model performs better in that regard (van

Genuchten, 1980). However, this model decreases the hydraulic conductivity too much when the soil dries out. This leads to the models' inability to converge to a solution when rain falls on a dry soil. This can partly be solved by decreasing the element size and the time step at the cost of computation time. Another more recently developed model aimed at improving the SWRC at low suction heads by Scarfone et al. (2020) could be also be used.

Secondly, a different modelling approach is necessary to incorporate lateral flow in the CL and CB into the model. This could be done by extending the current 1D model. As the CL and CB outflow show a typical exponential decrease after a flow peak, the current 1D model could be extended by using a simple time lag function over the simulated outflow from the 1D model. Alternatively, as the CL and CB outflows show a typical exponential decline after a peak, outflow from the 1D model could be put into a bucket model where outflow is an exponential function of the storage. These options could more effectively capture lateral flow dynamics and thus reduce the models' error.

Another option is to build a 2D model using the measured soil properties presented here as has been done successfully in other studies (Aubertin et al., 2009; Kämpf & Montenegro, 1997; G. Li et al., 2022; Scarfone et al., 2023; Vachon et al., 2015). This would likely result in better estimates of the storage, since the non-linear distribution of moisture along the slope could also be taken into account. Initially, this study aimed at doing so as well, but too much difficulties were encountered to build such model in the given time.

For example, defining the soil properties of a gravel in the CB is difficult as they need to satisfy two conflicting goals. Firstly it should produce a CBE between the CL and the CB and secondly the downhill flow should be rather swift. The first goal requires the CB to have a low WEV, but this will prohibit downward flow when breakthrough occurs in an otherwise dry CB. Berger (2018) reported similar issues with reproducing the threshold behaviour of the CB flows. The breakthrough flow through a CB happens preferentially (Kämpf et al., 2003) which can be hard to capture using a finite-element model. Increasing the mesh density could help, at the price of computation time.

Furthermore, although it was not it was not found to be as impactful as the two points mentioned before, the model could be further improved by taking into account temperature variations. Beside the effect on viscosity, it can also indicate when precipitation fell as snow. Especially the latter has a significant influence on the water balance (Khire et al., 1999).

9. References

Abdolahzadeh, A. M., Vachon, B. L., & Cabral, A. R. (2011a). Assessment of the Design of an Experimental Cover with Capillary Barrier Effect Using 4 Years of Field Data. *Geotechnical and Geological Engineering*, *29*, 783–802. https://doi.org/10.1007/s10706-011-9417-x

Abdolahzadeh, A. M., Vachon, B. L., & Cabral, A. R. (2011b). Evaluation of the effectiveness of a cover with capillary barrier effect to control percolation into a waste disposal facility. *Canadian Geotechnical Journal*, *48*(7), 996–1009. https://doi.org/10.1139/t11-017

Ahoughalandari, B., Cabral, A. R., & Leroueil, S. (2018). Elements of Design of Passive Methane Oxidation Biosystems: Fundamental and Practical Considerations About Compaction and Hydraulic Characteristics on Biogas Migration. *Geotechnical and Geological Engineering*, *36*(4), 2593–2609. https://doi.org/10.1007/s10706-018-0485-z

Andersen, L. J., & Madsen, B. (1983). Use of "the capillary barrier" as a shield against groundwater pollution from fly-ash deposits. *Water Science and Technology*, *15*(11), 207–212. https://doi.org/10.2166/wst.1983.0086

Ankeny, M. B., Kaspar, T. C., & Horton, R. (1988). Design for an automated tension infiltrometer. *Soil Science Society of America Journal*, *52*, 893–896.

Aubertin, M., Cifuentes, E., Apithy, S. A., Bussière, B., Molson, J., & Chapuis, R. P. (2009). Analyses of water diversion along inclined covers with capillary barrier effects. *Canadian Geotechnical Journal*, *46*(10), 1146–1164. https://doi.org/10.1139/T09-050

Averjanov, S. F. (1950). About permeability of subsurface soils in case of complete saturation. *English Collection*, *7*, 19–21.

Baker, R. S., & Hillel, D. (1990). Laboratory Tests of a Theory of Fingering during Infiltration into Layered Soils. *Soil Science Society of America Journal*, *54*(1), 20–30.

Berger, K. (2018). Operational validation of HYDRUS (2D/3D) for capillary barriers using data of a 10-m tipping trough. *Journal of Hydrology and Hydromechanics*, *66*(2), 153–160. https://doi.org/10.1515/johh-2017-0059

Blume, H.-P., Brümmer, G. W., Fleige, H., Horn, R., Kandeler, E., Kögel-Knabner, I., Kretzschmar, R., Stahr, K., & Wilke, B.-M. (2016). *Soil Science* (1st ed., Vol. 70, Issue 1). Springer.

Brand, E., de Nijs, T. C. M., Dijkstra, J. J., & Comans, R. N. J. (2016). A novel approach in calculating site-specific aftercare completion criteria for landfills in The Netherlands: Policy developments. *Waste Management*, *56*, 255–261. https://doi.org/10.1016/j.wasman.2016.07.038

Bussière, B., Aubertin, M., & Chapuis, R. P. (2003). The behavior of inclined covers used as oxygen barriers. *Canadian Geotechnical Journal*, *40*(3), 512–535. https://doi.org/10.1139/t03-001

Council Directive 1999/31/EC on the landfill of waste, Official Journal of the European Communities L182/1 (1999). https://doi.org/10.1039/ap9842100196

Deponieverordnung, (2009). https://www.gesetze-im-internet.de/depv_2009/DepV.pdf

Feddes, R. A., & Raats, P. A. C. (2004). Parameterizing the soil-water-plant root system. In R. A. Feddes, G. H. de Rooij, & J. C. van Dam (Eds.), *Unsaturated-Zone Modeling: Progress, Challenges, and Applications* (Vol. 6, pp. 95–141). Kluwer Academic Publishers. https://doi.org/10.2136/vzj2006.0162br

Fredlund, D. G., & Xing, A. (1994). Equations for the soil-water characteristic curve. *Canadian Geotechnical Journal*, *31*(4), 521–532. https://doi.org/10.1139/T94-061

Gebert, J., Huber-Humer, M., & Cabral, A. R. (2022). Design of Microbial Methane Oxidation

Systems for Landfills. *Frontiers in Environmental Science*, *10*. https://doi.org/10.3389/fenvs.2022.907562

Geck, C., Scharff, H., Pfeiffer, E. M., & Gebert, J. (2016). Validation of a simple model to predict the performance of methane oxidation systems, using field data from a large scale biocover test field. *Waste Management*, *56*, 280–289. https://doi.org/10.1016/j.wasman.2016.06.006

Giurgea, V. I., Hötzl, H., & Breh, W. (2003). Studies on the long-term performance of an alternative surface-sealing system with underlying capillary barrier. In T. H. Christensen, R. Cossu, & R. Stegmann (Eds.), *Ninth International Waste Management and Landfill Symposium*. CISA Publisher.

Heimovaara, T. (2022). *CIE4365 Modelling Coupled Processes. Lecture 03: Unsaturated Flow*. TU Delft.

Ho, C. K., & Webb, S. W. (1998). Capillary barrier performance in heterogeneous porous media. *Water Resources Research*, *34*(4), 603–609. https://doi.org/10.1029/98WR00217

Johnson, K. H., & Panders, J. L. (2003). How do modern landfills leak? In T. H. Christensen, R. Cossu, & R. Stegmann (Eds.), *Ninth International Waste Maangement and Landfill Symposium* (Issue October). CISA Environmental Sanitary Engineering Centre.

Kämpf, M., Holfelder, T., & Montenegro, H. (2003). Identification and parameterization of flow processes in artificial capillary barriers. *Water Resources Research*, *39*(10), 1276–1285. https://doi.org/10.1029/2002WR001860

Kämpf, M., & Montenegro, H. (1997). On the performance of capillary barriers as landfill cover. *Hydrology and Earth System Sciences*, *4*, 925–929.

Khire, M. V., Benson, C. H., & Bosscher, P. J. (1999). Field data from a capillary barrier and model predictions with UNSAT-H. *Journal of Geotechnical and Geoenvironmental Engineering*, *125*(6), 518–527.

Khire, M. V., Benson, C. H., & Bosscher, P. J. (2000). Capillary Barriers: Design Variables and Water Balance. *Journal of Geotechnical and Geoenvironmental Engineering*, *126*(8), 695–708.

KNMI. (2022). *Verdamping in Nederland*. https://www.knmi.nl/kennis-en-datacentrum/achtergrond/verdamping-in-nederland

KNMI. (2023a). *Daggegevens van het weer in Nederland*. https://www.knmi.nl/nederland-nu/klimatologie/daggegevens

KNMI. (2023b). *Uurgegevens van het weer in Nederland*. https://www.knmi.nl/nederland-nu/klimatologie/uurgegevens

Kuang, X., Jiao, J. J., Zheng, C., Cherry, J. A., & Li, H. (2020). A review of specific storage in aquifers. *Journal of Hydrology*, *581*. https://doi.org/10.1016/j.jhydrol.2019.124383

Li, G., Zhan, L., Zhang, S., Feng, S., & Zhang, Z. (2022). A dual-porosity model for coupled rainwater and landfill gas transport through capillary barrier covers. *Computers and Geotechnics*, *151*. https://doi.org/10.1016/J.COMPGEO.2022.104966

Li, K. Y., Jong, R. De, & Boisvert, J. B. (2001). An exponential root-water-uptake model with water stress compensation. *Journal of Hydrology*, *252*, 189–204.

Lu, N., & Likos, W. J. (2004). *Unsaturated Soil Mechanics*. John Wiley & Sons, Inc.

Melchior+Wittpohl. (2009). *Versuchsfelder Deponie Wieringermeer Bauüberwachung und Prüfung mineralische Baustoffe Abschlussdokumentation*.

Melchior+Wittpohl. (2011). *Versuchsfelder Deponie Wieringermeer Aufgrabung 2011 Ergebnisbericht*.

Melchior+Wittpohl. (2014a). *Versuchsfelder Deponie Wieringermeer Aufgrabungen 2013 Ergebnisbericht*.

Melchior+Wittpohl. (2014b). *Versuchsfelder Deponie Wieringermeer Wissenschatliche Betreuung Datenauswertung Nov 2009 bis Okt 2013*.

Melchior, S., Sokollek, V., Berger, K., Vielhaber, B., & Steinert, B. (2010). Results from 18 Years of In Situ Performance Testing of Landfill Cover Systems in Germany. *Journal of Environmental Engineering*, *136*(8), 815–823. https://doi.org/10.1061/(asce)ee.1943-7870.0000200

Ministerie van VROM. (1991). *Richtlijnen voor dichte eindafwerking op afval- en reststofbergingen*.

Myhre, G., Shindell, D., Bréon, F.-M., Collins, W., Fuglestvedt, J., Huang, J., Koch, D., Lamarque, J.-F., Lee, D., Mendoza, B., Nakajima, T., Robock, A., Stephens, G., Takemura, T., & Zhang, H. (2013). Climate Change 2013: The Physical Science Basis. Contribution of Working Group I to the Fifth Assessment Report of the Intergovernmental Panel on Climate Change. In T. F. Stocker, D. H. Qin, G. K. Plattner, M. M. B. Tignor, S. K. Allen, J. Boschung, A. Nauels, Y. Xia, V. Bex, & P. M. Midgley (Eds.), *Climate Change 2013: The Physical Science Basis. Contribution of Working Group I to the Fifth Assessment Report of the Intergovernmental Panel on Climate Change.* (pp. 659–740). Cambridge University Press.

Nakafusa, S., Kobayashi, K., Morii, T., & Nishimura, T. (2011). Alternative employment of crushed shell particles in capillary barrier of soil. *International Journal of GEOMATE*, *1*(1), 50–55. https://doi.org/10.21660/2011.1g

Nyhan, J. W., Hakonson, T. E., & Drennon, B. J. (1990). A Water Balance Study of Two Landfill Cover Designs for Semiarid Regions. *Journal of Environmental Quality*, *19*(2), 281–288. https://doi.org/10.2134/jeq1990.00472425001900020014x

Ogorzalek, A. S., Bohnhoff, G. L., Shackelford, C. D., Benson, C. H., & Apiwantragoon, P. (2008). Comparison of Field Data and Water-Balance Predictions for a Capillary Barrier Cover. *Journal of Geotechnical and Geoenvironmental Engineering*, *134*(4), 470–486. https://doi.org/10.1061/(asce)1090-0241(2008)134:4(470)

Oldenburg, C. M., & Pruess, K. (1993). On numerical modeling of capillary barriers. *Water Resources Research*, *29*(4), 1045–1056. https://doi.org/10.1029/92WR02875

Rahardjo, H., Santoso, V. A., Leong, E. C., Ng, Y. S., & Hua, C. J. (2012). Performance of an Instrumented Slope Covered by a Capillary Barrier System. *Journal of Geotechnical and Geoenvironmental Engineering*, *138*(4), 481–490. https://doi.org/10.1061/(asce)gt.1943-5606.0000600

Rahardjo, H., Santoso, V. A., Leong, E. C., Ng, Y. S., Tam, C. P. H., & Satyanaga, A. (2013). Use of recycled crushed concrete and Secudrain in capillary barriers for slope stabilization. *Canadian Geotechnical Journal*, *50*(6), 662–673. https://doi.org/10.1139/cgj-2012-0035

Rahardjo, H., Satyanaga, A., Harnas, F. R., & Leong, E. C. (2016). Use of Dual Capillary Barrier as Cover System for a Sanitary Landfill in Singapore. *Indian Geotechnical Journal*, *46*(3), 228–238. https://doi.org/10.1007/s40098-015-0173-3

Rançon, D. (1972). Structures Seches et Barrieres Capillares en Milieux Poreux. - Application On Stockage Dans le Sol. Rapport CEA-R-4310. *Centra d'Etudes Nucleares de Cadarche*.

Ross, B. (1990). The Diversion Capacity of Capillary Barriers. *Water Resources Research*, *26*(10), 2625–2629.

Röwer, I. U., Streese-Kleeberg, J., Scharff, H., Pfeiffer, E.-M., & Gebert, J. (2016). Optimized Landfill Biocover for CH4 Oxidation II: Implications of Spatially Heterogeneous Fluxes for Monitoring and Emission Prediction. *Current Environmental Engineering*, *3*, 94–106. https://doi.org/10.2174/2212717803666160804150 3

Scarfone, R., Wheeler, S. J., & Lloret-Cabot, M. (2020). A conceptual hydraulic conductivity model for unsaturated soils at low degree of saturation and application to the study of

capillary barrier systems. *Journal of Geotechnical and Geoenvironmental Engineering*, *146*(10).
Scarfone, R., Wheeler, S. J., & Smith, C. C. (2023). Numerical modelling of the application of capillary barrier systems for prevention of rainfall-induced slope instability. *Acta Geotechnica*, *18*(1), 355–378. https://doi.org/10.1007/s11440-022-01582-w
Scheutz, C., Kjeldsen, P., Bogner, J., De Visscher, A., Gebert, J., Hilger, H., Huber-Humer, M., & Spokas, K. (2009). Microbial methane oxidation processes and technologies for mitigation of landfill gas emissions. *Waste Management and Research*, *27*(5). https://doi.org/10.1177/0734242X09339325
Shampine, L. F., & Reichelt, M. W. (1997). The MATLAB ODE suite. *SIAM Journal on Sciencific Computing*, *18*(1), 1–22.
Spieksma, J. F. M., Dolman, A. J., & Schouwenaars, J. M. (1995). *De parameterisatie van de verdamping van natuurterreinen in hydrologische modellen*.
Steenhuis, T. S., Parlange, J.-Y., & Kung, K.-J. S. (1991). Comment on "The Diversion Capacity of Capillary Barriers" by Benjamin Ross. *Water Resources Research*, *27*(8), 2155–2156.
Steinert, B. (1999). *Kapillarsperren für die oberflächenabdichtung von deponien und altlasten - Bodenphysikalische grundlagen und kipprinnenuntersuchungen -*. Universität Hamburg.
Stormont, J. C. (1996). The effectiveness of two capillary barriers on a 10% slope. *Geotechnical and Geological Engineering*, *14*(4), 243–267. https://doi.org/10.1007/BF00421943
Stormont, J. C., & Anderson, C. E. (1999). *Capillary barrier effect from underlying coarser soil layer*. *125*(8), 641–648.
Stormont, J. C., & Morris, C. E. (1998). Method to Estimate Water Storage Capacity of Capillary Barriers. *Journal of Geotechnical and Geoenvironmental Engineering*, *124*(4), 297–302. https://doi.org/10.1061/(asce)1090-0241(1998)124:4(297)
Stortbesluit bodembescherming, (1993). https://wetten.overheid.nl/BWBR0005858/2016-07-01#HoofdstukIV
Tami, D., Rahardjo, H., Leong, E. C., & Fredlund, D. G. (2004). A physical model for sloping capillary barriers. *Geotechnical Testing Journal*, *27*(2), 173–183. https://doi.org/10.1520/gtj11431
Uitvoeringsregeling Stortbesluit bodembescherming, (1993). https://wetten.overheid.nl/BWBR0005877/2018-12-04#Hoofdstuk4
Vachon, B. L., Abdolahzadeh, A. M., & Cabral, A. R. (2015). Predicting the diversion length of capillary barriers using steady state and transient state numerical modeling : case study of the Saint-Tite-des-Caps landfill final cover. *Canadian Geotechnical Journal*, *52*, 2141–2148.
van Genuchten, M. T. (1980). A Closed-form Equation for Predicting the Hydraulic Conductivity of Unsaturated Soils. In *Soil Science Society of America Journal* (Vol. 44, Issue 5, pp. 892–898). https://doi.org/10.2136/sssaj1980.03615995004400050002x
van Genuchten, M. T., Leij, F. J., & Yates, S. R. (1991). *The RETC Code for Quantifying the Hydraulic Functions of Unsaturated Soils* (Issue Report IAG-DW12933934).
van Turnhout, A. G., Oonk, H., Scharff, H., & Heimovaara, T. J. (2020). Optimizing landfill aeration strategy with a 3-D multiphase model. *Waste Management*, *102*, 499–509. https://doi.org/10.1016/j.wasman.2019.10.051
van Verseveld, C. J. W., & Gebert, J. (2020). Effect of compaction and soil moisture on the effective permeability of sands for use in methane oxidation systems. *Waste Management*, *107*, 44–53. https://doi.org/10.1016/j.wasman.2020.03.038
Verseveld, C. J. W. Van. (2018). *Gas flow through methane oxidation systems: A laboratory and numerical study for optimising*. Delft University of Technology.
Virtanen, P., Gommers, R., Oliphant, T. E., Haberland, M., Reddy, T., Cournapeau, D.,

Burovski, E., Peterson, P., Weckesser, W., Bright, J., Walt, S. J. van der, Brett, M., Wilson, J., Millman, K. J., Mayorov, N., Nelson, A. R. J., Jones, E., Kern, R., Larson, E., … SciPy 1.0 Contributors. (2020). SciPy 1.0: Fundamental Algorithms for Scientific Computing in Python. *Nature Methods*, *17*(3), 261–272. https://doi.org/10.1038/s41592-019-0686-2

Wang, S., Yang, Y., Luo, Y., & Rivera, A. (2013). Spatial and seasonal variations in evapotranspiration over Canada's landmass. *Hydrology and Earth System Sciences*, *17*(9), 3561–3575. https://doi.org/10.5194/HESS-17-3561-2013

Waskom, M. L. (2021). seaborn: statistical data visualization. *Journal of Open Source Software*, *6*(60), 3021. https://doi.org/10.21105/joss.03021

Wawra, B., & Holfelder, T. (2003). Development of a landfill cover with capillary barrier or methane oxidation - the capillary barrier as gas distribution layer. In T. H. Christensen, R. Cossu, & R. Stegmann (Eds.), *Ninth International Waste Management and Landfill Symposium*. CISA Publisher.

Yanful, E. K. (1993). Oxygen diffusion through soil covers on sulphidic mine tailings. *Journal of Geotechnical Engineering*, *119*(8), 1207–1228.

Yang, H., Rahardjo, H., Leong, E. C., & Fredlund, D. G. (2004). A study of infiltration on three sand capillary barriers. *Canadian Geotechnical Journal*, *41*(4), 629–643. https://doi.org/10.1139/T04-021

Zhai, Q., Rahardjo, H., Satyanaga, A., & Dai, G. (2020). Estimation of the soil-water characteristic curve from the grain size distribution of coarse-grained soils. *Engineering Geology*, *267*(January), 105502. https://doi.org/10.1016/j.enggeo.2020.105502

Zhan, T. L. T., Li, H., Jia, G. W., Chen, Y. M., & Fredlund, D. G. (2014). Physical and numerical study of lateral diversion by three-layer inclined capillary barrier covers under humid climatic conditions. *Canadian Geotechnical Journal*, *51*, 1438–1448. https://doi.org/10.1139/cgj-2014-0548

Zornberg, J. G., Bouazza, A., & McCartney, J. S. (2010). Geosynthetic capillary barriers: Current state of knowledge. *Geosynthetics International*, *17*(5), 273–300. https://doi.org/10.1680/gein.2010.17.5.273

Appendices

A. Theoretical background

A.1. Soil water potential and capillarity

Unsaturated soil, which is located above the groundwater table, is a multiphase medium (Figure 26). It contains minerals, water, air and biological substances. This subsection focuses on the thermodynamic state of water in unsaturated soil.

The state of water is best described by the term potential or suction (ψ). This concept originates from thermodynamics and describes the working capacity of water in a soil as a result of many different forces that act on it. Potentials are commonly expressed in units of energy per unit volume, which is pressure (Pa), or in units of energy per unit weight, which is head (m). In the case of soil water, these two are related by Equation 23.

$$p = \rho_w g h \qquad \text{Equation 23}$$

Potential is defined with respect to a certain reference potential, which is in this case free water without any influences of dissolved solutes and other phases. It is common to locate this reference potential at groundwater level. At this level the pressure in the water is equal to the air pressure.

Potential components

The total potential of water in a soil (ψ_t) is comprised of several components of which the gravimetric and matric potential fit within the scope of this thesis. Gas potential, which is a situation where the air pressure in the soil is different from the pressure at the point of reference, is also important for water flow but not considered in this study (van Turnhout et al., 2020).

Gravimetric potential (ψ_z) is the amount of work needed to lift a volume of water from the point of reference to the location of the soil water.

Matric potential (ψ_m), also called suction, entails the influence of the soil matrix on the soil water. The soil matrix binds the water to itself by adhesive and capillary forces. Adhesive forces are the result of electrostatic and Van der Waals forces between the soil grains and the water molecules, resulting in the formation of water films around the soil particles. Adhesive forces are more relevant for soils at higher matric potentials and for soils with a high specific surface area or surface charge (clays or soils containing organic matter). On the other hand, capillary forces dominate the matric potential at lower matric potentials and for soils with a coarse grain size. This mechanism is the most dominant in the functioning of a capillary barrier.

Summarizing, the soil water potential is the sum of the gravitational and the matric potential (Equation 24). The matric potential (suction in the remainder of this thesis) is commonly defined as negative.

$$\psi_t = \psi_z + \psi_m \qquad \text{Equation 24}$$

This can also be defined in units of head:

$$h_t = h_z + h_m \qquad \text{Equation 25}$$

With h_t, h_z and h_m the total, gravimetric and suction head [m].

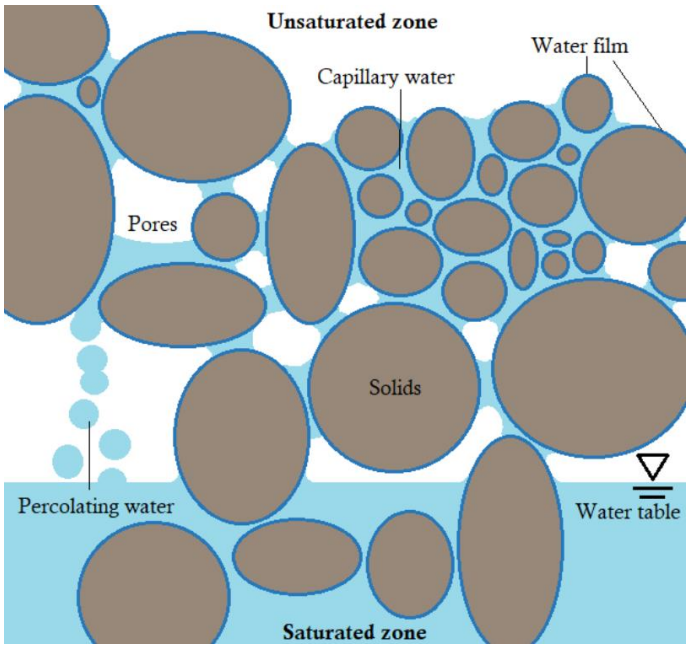

Figure 26: Conceptualisation of the unsaturated zone at particle scale (Adopted from Verseveld (2018, p. 13)*)*

Capillary forces

Capillary forces are the result of adhesive forces of water molecules with a solid particle and the cohesion between water molecules. Because of that, there is pressure difference over the interface of water and air. This can be described by the Young-Laplace equation:

$$u_a - u_w = \frac{2T_s \cos \alpha}{r} \qquad \text{Equation 26}$$

With u_a and u_w the air- and water pressure respectively [Pa], T_s the surface tension of the air-water interface, α the contact angle between the tube and the water surface and r the radius of the tube. The capillary tube model, as illustrated in Figure 27, is often used to explain the capillary forces in a soil. This difference in air and water pressure is compensated by an increase in water level height. With the reference air pressure taken as 0, this leads to:

$$-u_w = \frac{2T_s \cos \alpha}{r} = -h_w \rho_w g \qquad \text{Equation 27}$$

Which can be rewritten as:

$$h_w = \frac{2T_s \cos \alpha}{r \rho_w g} \qquad \text{Equation 28}$$

with h_w the height of the water above the reference water level, also called the height of the capillary rise [m].

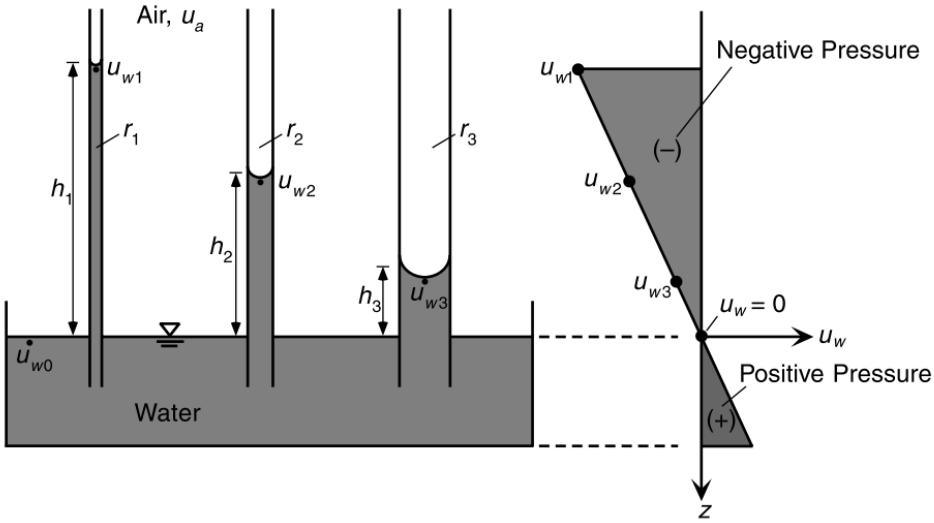

Figure 27: Capillary tube model (Adopted from Lu&Likos (2004, p. 132))

Equation 28 can be used to quantify the suction head in a potential range where adhesive forces can be neglected ($h_w = h_m$). Pores in soils have irregular shapes, however. Therefore, often an effective radius is used. Furthermore, soils contain a range of pore sizes. Their pore size distribution (PSD) depends on the grain size distribution (GSD) and the density of the soil.

A.2. Soil hysteresis

The main causes for soil hysteresis are a change in wettability or the contact angle (α in Equation 28[5]), blockage of water flow by air inclusions and most importantly pore bottlenecks (Figure 28b). This results in a SWRC following different paths depending on how far a soil was wetted or drained called scanning curves (Figure 28a).

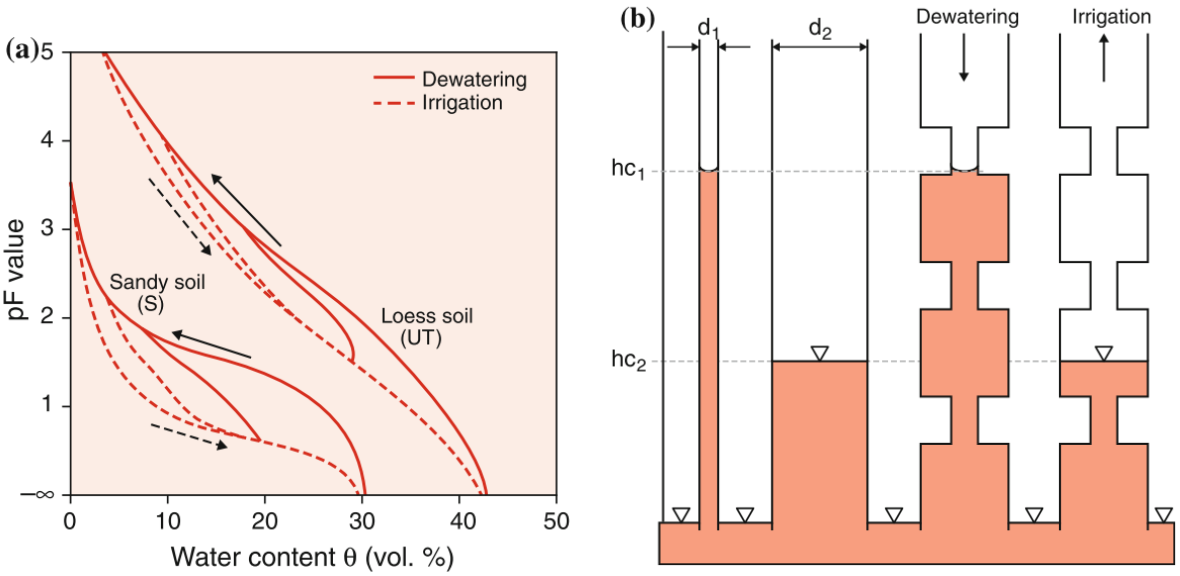

Figure 28: (a): Soil hysteresis for a sandy and loess soil. (b): Visualisation of pore bottlenecks; The difference in diameter between a small pore bottleneck and the bigger pores around it results in a higher capillary force (Equation 28), which prevents the water to drain from the bigger pore beneath, resulting in a higher water content compared to wetting the tubes where water will only rise to the level defined by the radius of the bigger pore. Adopted from Blume et al. (2016, p. 238).

[5] α typically take values around 0° when drying and between 0° and 90° when wetting A high organic content in a soil can increase even more between 90° and 180° (Lu & Likos, 2004).

A.3. Explanation of capillary barrier effect using a capillary tube model

Lu and Likos use a conceptual tube model for the interface between the fine and coarse soil layer as shown in Figure 29. The fine and coarse soil are conceptualised as a small and large tube respectively with a radius r corresponding to their average pore sizes with a transition between the two different tube diameters in between. Furthermore, they simplify the Young-Laplace equation (Equation 26), assuming a 0° contact angle and taking u_a as 0 Pa:

$$u_w = -\frac{2T_s}{r} \qquad \text{Equation 29}$$

Next, the hydrostatic condition for an increasing water lens thickness is considered. At initial conditions when the soil is completely dry, an infinitesimal water lens exists where the water pressure is equal at the bottom and at the top of the water lens (Figure 29a):

$$u_{wt} = u_{wb} = -\frac{2T_s}{r_{fine}} \qquad \text{Equation 30}$$

The water lens thickness increases as the water content in the fine layer increases. This causes the buildup of hydraulic pressure. Consequently the water pressure at the bottom becomes less negative which is compensated by the bottom water lens moving into the transitional regime:

$$u_{wb} = -\frac{2T_s}{r_{tran}} = u_{wt} + \rho_w g h_{wl} \qquad \text{Equation 31}$$

With h_{wl} the thickness of the water lens. The thickness of the water lens can increase until the pressure at the bottom of the water lens reaches the capillary tension corresponding to the radius of the coarse layer:

$$u_{wb} = -\frac{2T_s}{r_{coarse}} \qquad \text{Equation 32}$$

The corresponding hydraulic pressure is equal to the difference in water pressure at the top and bottom of the water lens which are determined by their effective radii:

$$h_b \rho_w g = u_{wb} - u_{wt} = 2T_s \left(\frac{1}{r_{fine}} - \frac{1}{r_{coarse}} \right) \qquad \text{Equation 33}$$

Any increase in hydraulic pressure will result in breakthrough.

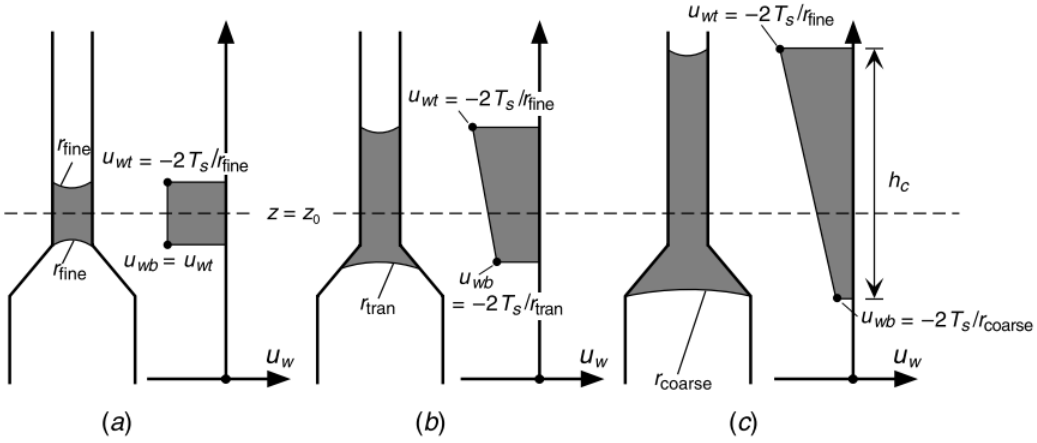

Figure 29: Conceptual model of the interface between fine and coarse textured soil under increasing saturation. Adopted from Lu & Likos (2004, p. 342).

B. Test field

B.1. Construction of test field

Figure 30: Bottom and side walls of test field

Figure 31: Construction of the capillary block, which drains through the most upslope drain. The capillary layers drains at the bottom drain.

Figure 32: Bridge for drains to the measurement container

Figure 33: Construction of the capillary layer.

Figure 34: Construction of MOL. The white mat is a drainage mat above the drain for the CL, to prevent additional precipitation to be collected.

Figure 35: View at end of construction. The boxes and tubes emerging from the field were used by the landfill gas experiments.

B.2. Reconstruction

These photos are actually not from the reconstruction in 2013 but from the construction of another test field beside the test field with the CBS and MOL in 2009. However, the same method was used in the reconstruction of the CBS+MOL test field.

Figure 36: Construction of top 60 cm of the MOL with a bulldozer.

Figure 37: Loosening of the soil using a tractor with spades.

B.3. Construction plan cross section

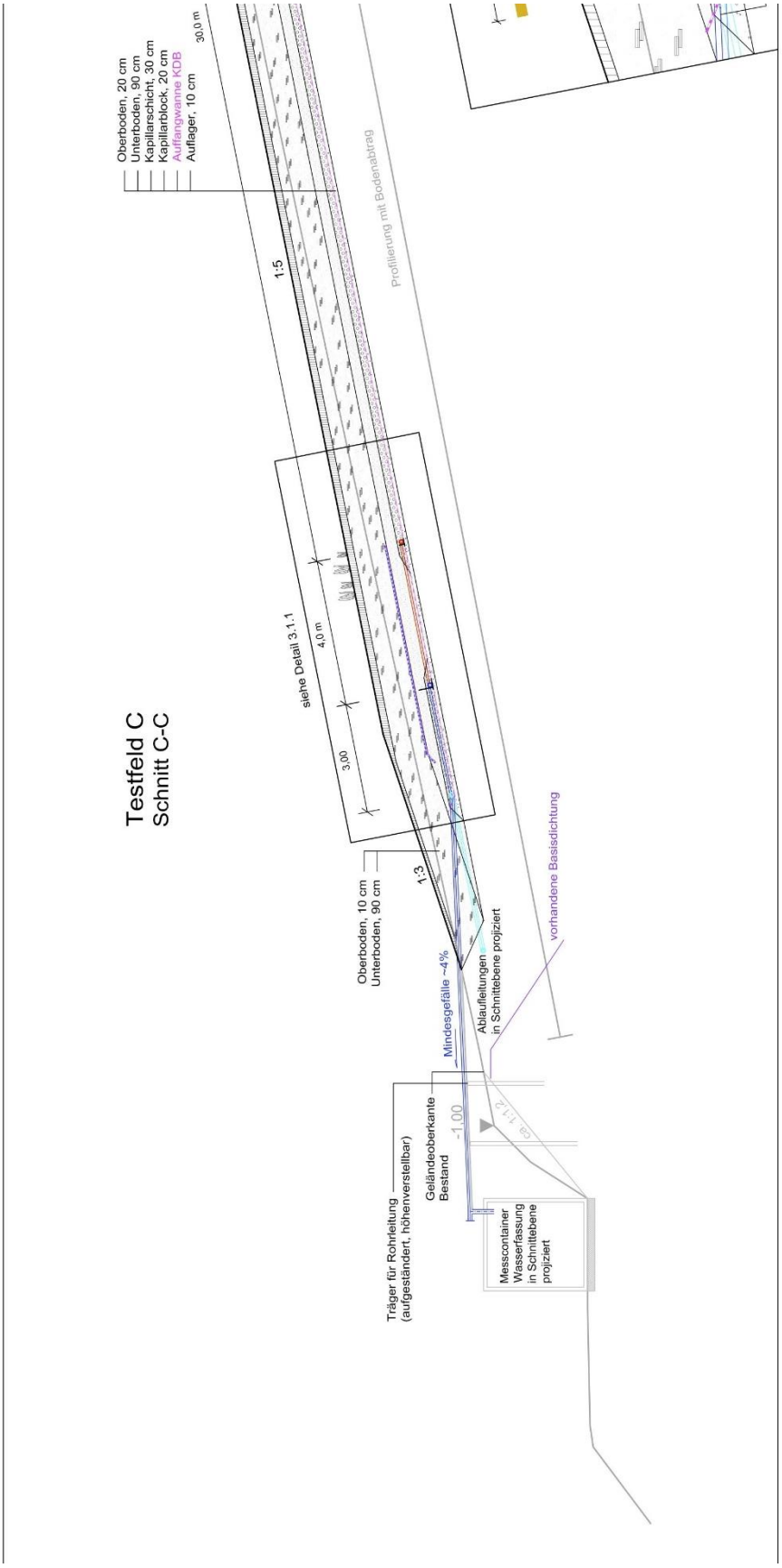

Figure 38: Construction plan cross section part 1

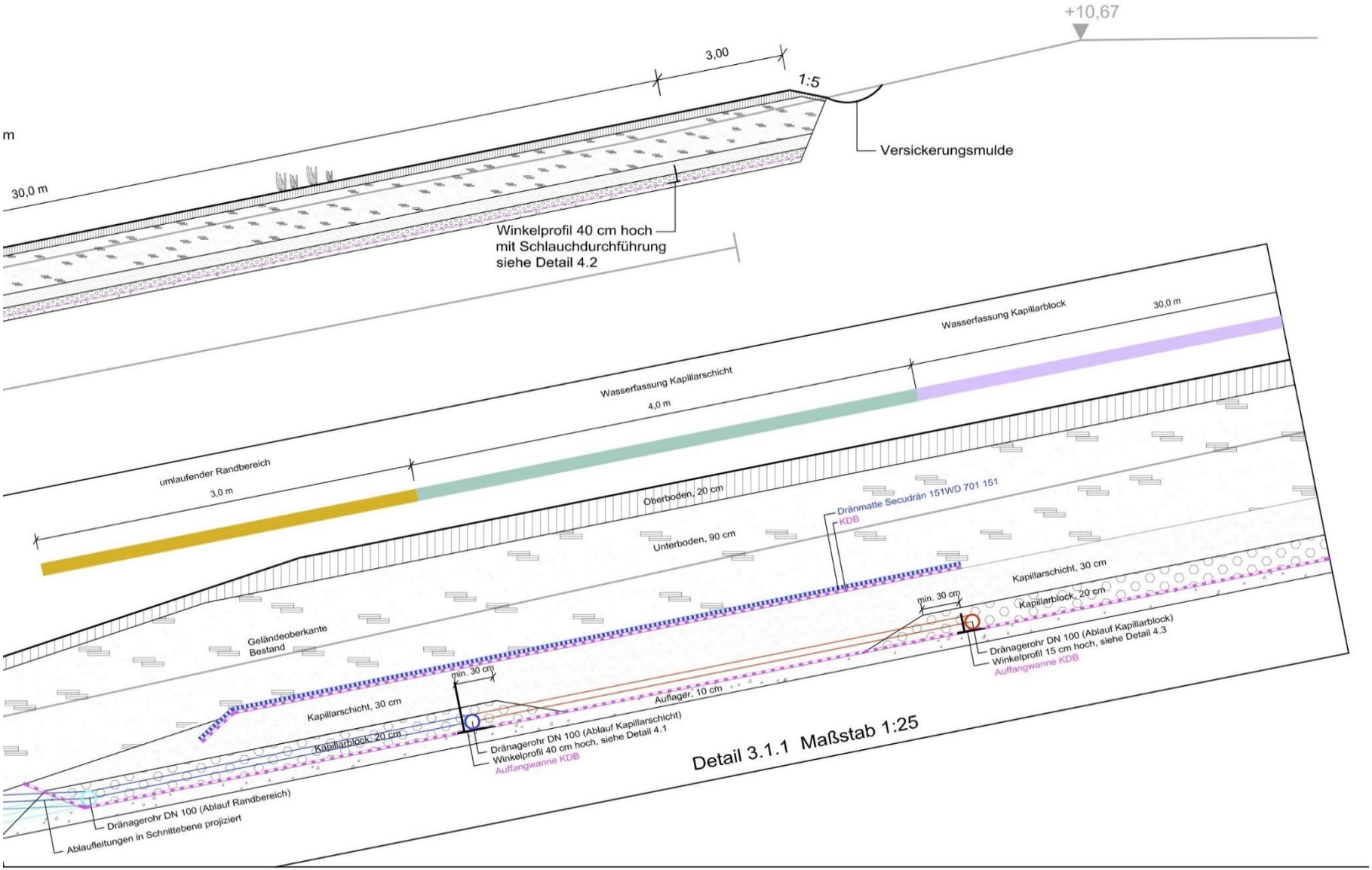

Figure 39: Construction plan cross section part 2

B.4. Measurement devices

Figure 40: Three rain gauges at the test field as seen from the top of the field. In front the white Pluvio-2 rain gauge, to its left at the wooded stick the manual rain gauge at ground level and to its right the manual rain gauge at 1 meter height.

Figure 41: The insulated drainage pipes of the capillary layer and block (left two pipes) leading to the measurement container.

Figure 42: Inside the measurement container the tipping buckets and the IBC water storage tanks.

Figure 43: The tipping bucket of the capillary block.

B.5. Data gathering, logging and storage procedure

B.5.1. Tipping bucket volume measurement procedure

The procedure for measuring the volume of the tipping bucket is as follows. The tipping buckets have two sides. The volume of each side is measured thrice, by measuring the amount of water that fits in it until it tips. After that the average value of the six measurements is used as final measurement. Especially in the beginning of the measurement period there was formation of iron precipitates in the tipping buckets. Therefore, the same procedure was repeated before and after cleaning the tipping bucket to quantify the influence of this precipitation.

B.5.2. Manual precipitation measurement procedure

The accumulated rain in the manual rain gauges was measured in principle every week but especially at the beginning and between 2020 and 2022 there were times with larger time intervals (Figure 44).

The rain gauge consists of a steel casing with a collection pan inside. The precipitation is measured by pouring the water from the collection pan into a measurement cylinder. Their capacities are 60 mm and 10 mm respectively, so it should be done multiple times if the precipitation amount exceeds 10 mm. Additionally, when the accumulated precipitation exceeded the capacity of the collection pan it would accumulate in the steel casing. If so, this water was measured as well.

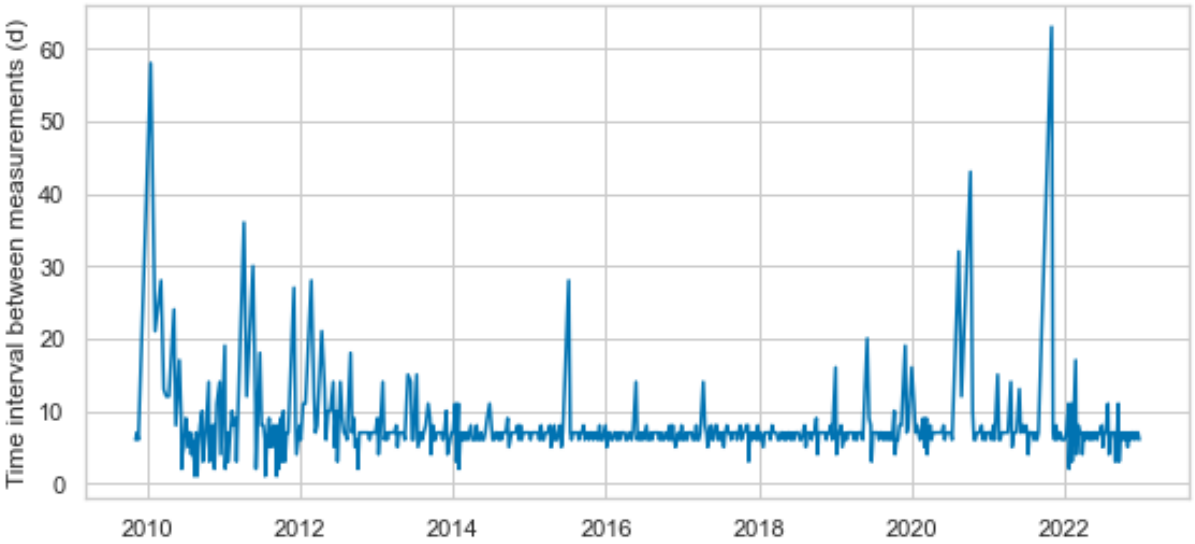

Figure 44: Time interval between measurements

B.5.3. Measurement data logging and storage

Figure 45 shows the overall procedure of the data logging and storage. The weather station, tipping buckets and the automatic rain gauge all send their analog/digital signals to the Programmable Logical Controller (PLC) which converts this signal to a value between 0 and 8000. A central data monitoring system CARS (Centraal Alarmering en Registratie Systeem) translates these PLC values to physical meaningful variable at regular time intervals. This data is sent to a database at a central server (BeNbase). Manual measurements like the tipping

bucket volume, precipitation measurements and logbooks are directly stored in this database. The software Oxidata can be used to analyse and correct the data in BeNbase.

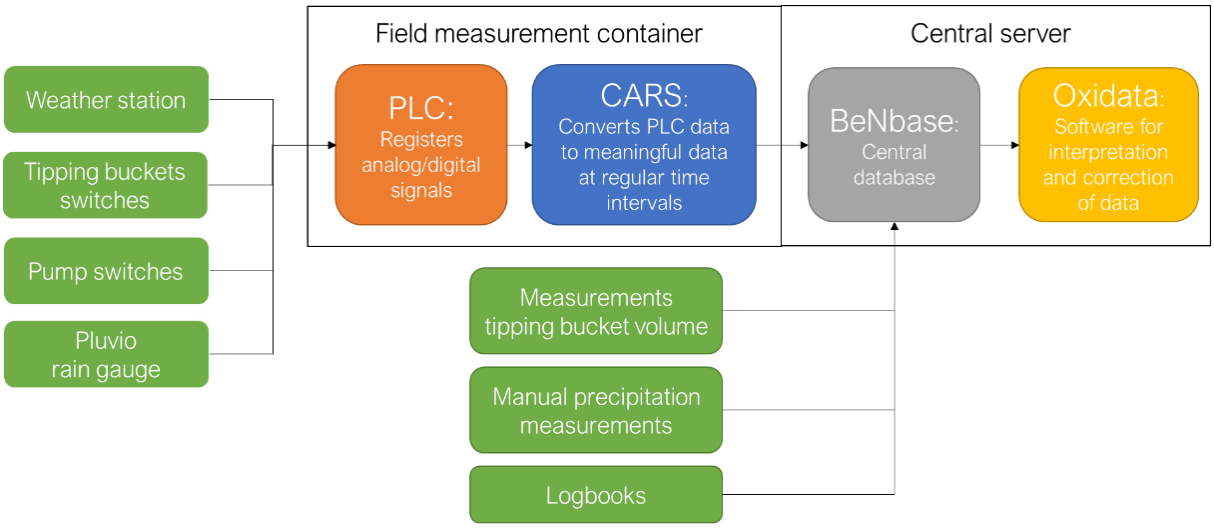

Figure 45: Visualisation of the data logging and storage procedure. The green boxes are sensors.

This research will use the raw data stored in BeNbase. The corrected Oxidata data is used as a reference for any errors in the raw data and in the processing of it.

B.6. Soil excavations

B.6.1. Sampling locations

Figure 46: Locations of soil excavations

B.6.2. Rooting density

Table 3: Qualitative measure of density of roots measured at April 2011.

Depth below surface [m]	Rooting density
0.0-0.1	Strong to filled with roots
0.1-0.2	Strong to filled with roots
0.2-0.3	Strong
0.3-0.4	Middle
0.4-0.5	Weak
0.5-0.6	Weak
0.6-0.7	Very weak
0.7-0.8	Very weak
0.8-0.9	Very weak

B.6.3. Photos

Figure 47: Soil profile excavation 2011 (Melchior+Wittpohl, 2011)

Figure 48: Excavation August 2013: Soil profile (Melchior+Wittpohl, 2014a). *Clear signs of soil aggregation, especially in the top 40 cm.*

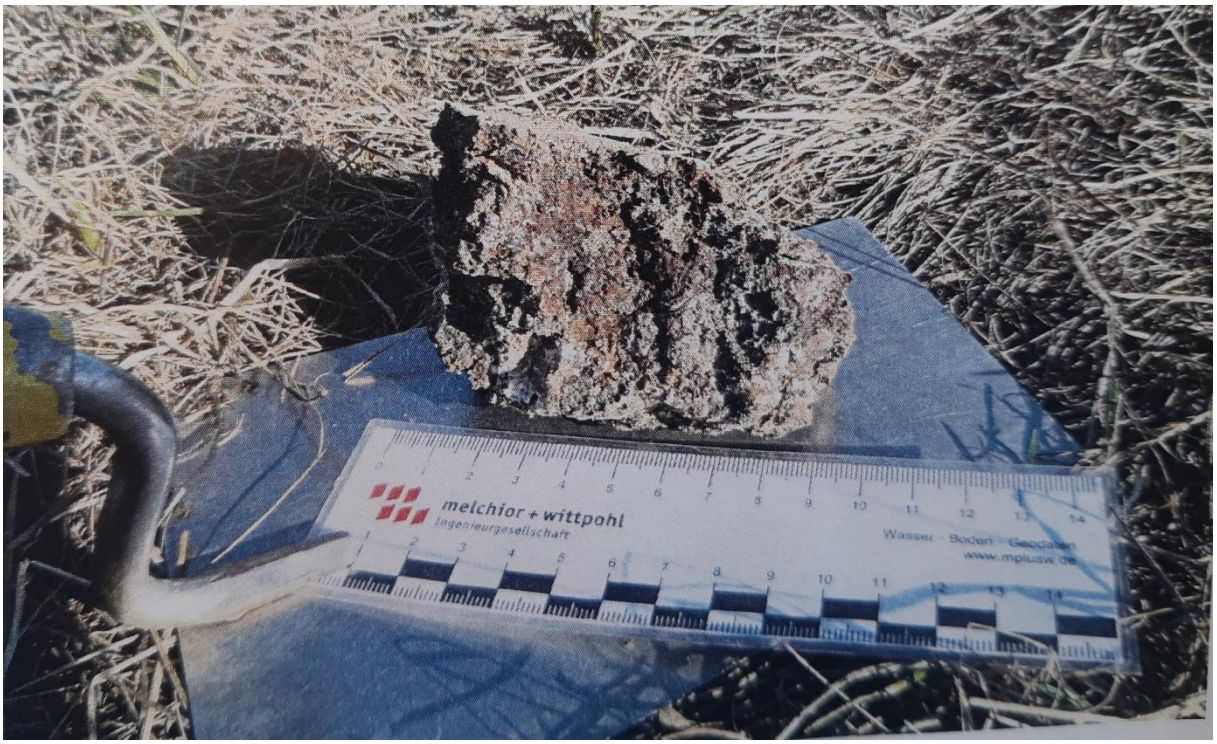

Figure 49: Excavation August 2013: soil aggregate (Melchior+Wittpohl, 2014a)

Figure 50: Excavation September 2013: Soil profile. Rooting of newly growing grass is strongest to 20 cm depth (Melchior+Wittpohl, 2014a)

Figure 51: Excavation November 2017: the rooting is still strongest in the top 20 cm, but also reaches into the CL (Verseveld, 2018).

Figure 52: Excavation November 2017: formation of most likely iron precipitates at the bottom of the CL (Verseveld, 2018). *As there were also iron precipitates in the outflow of the CL and CB, it is most likely that most of the CL flow happened at the bottom 3-4 cm.*

B.7. Soil measurements

This section gives an overview of the measurements performed in 2009, 2011, 2013 and 2017 (Melchior+Wittpohl, 2009, 2011, 2014a; Verseveld, 2018).

B.7.1. Grain size distribution

The procedure for measuring the GSD in 2009 followed the German standard DIN 18123, for which one sample per soil layer was sieved wet to remove all particle with a diameter smaller than 0.125 mm. The diameter of these particles was then determined by their settling velocity. The particles larger than 0.125 mm were dried and afterward sieved (Melchior+Wittpohl, 2009). The measurement of the CB in 2017 followed the British standard 1377-4 using a dry sieving test (Verseveld, 2018)

Table 4: Results of sieving tests: Values are the cumulative mass percentage of the total sample mass.

Particle diameter (mm)	CB	CL	SS	TS	CB_2017
63	100	100	100	100	
31.5	100	100	100	100	
16	100	100	100	100	
11.2	100				
8	97.7	100	98.2	98.8	100
4	29.8	99.9	97.7	97.9	
2.8		98.9			
2	1.4	96	96.9	97	33.85
1	0.6	81.4	96	96	
0.5	0.4	49.6	94.6	94.1	
0.25	0.3	12.8	83.1	88.2	
0.125	0.2	1.2	19.9	69	
0.0745			19.3		
0.063	0.1	0.3			1.77
0.0604				53.2	
0.0531			18.5		
0.0461				43.8	
0.0376			18.3		
0.0345				35.9	
0.0241			17.1		
0.0226				30.4	
0.0141			15.6		
0.0133				27.2	
0.0082			14.6		
0.008				22	
0.0051			12.4		1.77
0.005				18.9	
0.003			11.1	15.7	
0.0015			9.4	12.1	
0	0	0			0
Total sample mass (g)	**934.42**	**358.58**	**352.81**	**370.35**	**unknown**

B.7.2. Soil water retention measurements

A pressure plate or axis translation test was used to measure water contents and suction heads, following the standard DIN ISO 11274. This test measures these variables along a drying path. Its results are more uncertain as the soil approaches saturation or complete dryness (Lu & Likos, 2004, Chapter 10).

Table 5 and Table 6 contains the measured values for the excavations up to 2013. The measurements of 2017 are too large to present in this report. Instead, these can be found in the Excel sheet "SoilData.xlsx".

Table 5: Soil water contents (vol.-%) for different suctions measured by a pressure plate experiment. Locations are upslope (US) and downslope (DS)

date	Layer/ location	depth (m)	Suction (hPa)								
			3	**20**	**40**	**60**	**100**	**300**	**1000**	**3000**	**15000**
01/09/2009	CB	1.3	0								
	CL	1.05	32.77	28.91	22.35	18.86	9.1	5.08			0.93
	?	0.3	43.1			32.15		23.42			11.19
	?	0.5	42.33			31.34		25.06			15.42
	?	0.8	47.44			28.22		19.45			11.93
	?	0.05	50.27			39.79		31.77			18.94
13/04/2011	DS	0.05	49.33	45.33		41.42		36.45			22.57
	DS	0.3	51.73	46.07		42.39		35.78			20.98
	DS	0.5	45.39	38.07		25.38		19.29			14.57
	DS	0.8	44.23	36.67		26		19.26			11.3
12/08/2013	US	0.05	50.31			43.03		40.89	37.48	24.79	20.92
	DS	0.05	52.16			41.27		36.18	32.16	24.59	14.91
	DS	0.35	47.67			32.43		29.72	28.2	24.6	16.16
	US	0.35	45.69			20.62		19.04	15.86	13.21	10.31
	US	0.5	44.6			26.5		23.17	21.3	15.45	8.86
	US	0.68	43.83			23.75		20.77	17.86	13.55	8.94
	DS	0.5	46.67			19.95		17.57	15.1	10.56	7.46
	DS	0.68	44.87			26.32		21.7	18.6	15.77	10.68
23/09/2013	DS	0.05	45.96			42.5		39.72	36.49	30.01	25.74
	US	0.05	46.4			42.02		38.66	35.84	30.21	23.99
	US	0.35	44.2			26.19		20.43	18.86	17.87	14.08
	DS	0.35	45.52			29.41		24.55	21.78	14.36	11.57
	DS	0.5	44.14			23.7		19.74	17.58	13.25	9.62
	DS	0.68	47.1			25.49		20.36	18.26	14.17	10.86
	US	0.5	46.32			26		23.03	20.43	13.14	9.21
	US	0.68	39.51			18.72		16.02	13.85	12.97	9.15

Table 6: Dry densities and porosities. Locations are upslope (US) and downslope (DS)

date	Layer /location	depth (m)	dry density (g/cm3)	Porosity (dry)	Porosity (wet)	Porosity (?)
01/09/2009	CB	1.3	1.433			46
	CL	1.05	1.534			42
	?	0.3	1.391			46.6
	?	0.5	1.354			48
	?	0.8	1.296			50.4
	?	0.05	0.998			61
13/04/2011	DS	0.05	1.237			51.7
	DS	0.3	1.185			53.9
	DS	0.5	1.33			49.2
	DS	0.	1.257			52
12/08/2013	US	0.05	1.092	57.8	50.3	
	DS	0.05	1.152	55.5	52.2	
	DS	0.35	1.255	51.5	47.7	
	US	0.35	1.248	52.4	45.4	
	US	0.5	1.299	51.4	44.46	
	US	0.68	1.308	50.1	43.8	
	DS	0.5	1.23	53	46.7	
	DS	0.68	1.268	51.6	44.9	
23/09/2013	DS	0.05	1.376	46.9	46	
	US	0.05	1.288	50.3	46.4	
	US	0.35	1.403	45.8	44.2	
	DS	0.35	1.343	48.7	45.5	
	DS	0.5	1.357	48.2	44.1	
	DS	0.68	1.318	49.7	47.1	
	US	0.5	1.319	49.7	46.3	
	US	0.68	1.351	48.4	39.5	

B.7.3. Soil hydraulic conductivity measurements

The measured saturated hydraulic conductivities are shown in Table 7. These were found by using the falling head method on soil samples in the lab. For the CB the constant head method was used. The measurements followed the standard DIN 18130.

Table 7: Measured saturated hydraulic conductivities of the soils in m/s. Locations are upslope (US) and downslope (DS) (: These are three measurements of the CB and CL at the same depth)*

date	**Layer / location**	**Depth (m) / # measurement**			
		0.05	0.35	0.5	0.68
01/09/2009	CB	3.10E-02*	2.50E-02*	2.50E-02*	
	CL	1.20E-04*	3.19E-05*	6.17E-05*	
12/08/2013	US	4.70E-05	5.90E-05	2.20E-05	5.20E-05
	DS	4.30E-05	9.10E-05	3.50E-05	5.70E-05
23/09/2013	US	2.20E-07	1.50E-05	2.80E-05	4.40E-05
	DS	1.40E-08	1.60E-05	2.10E-05	3.00E-05

Furthermore, measurements of the hydraulic conductivity at an unsaturated state are given in Table 8. These were measured in the field using an automated tension infiltrometer (Ankeny et al., 1988).

Table 8: Measured saturated hydraulic conductivities of the soils in m/s. Locations are upslope (US) and downslope (DS) (: These are three measurements of the CL at the same depth)*

date	**Layer / location**	**Suction (hPa)**	**Depth (m)**						
			0.05	0.1	0.3	0.35	0.5	0.68	0.8
01/09/2009	CL	-10.2	4.74E-04*	3.42E-04*	3.35E-04*				
	?	-10.2	5.53E-06		3.97E-05		1.03E-05		1.58E-05
13/04/2011	DS	-10.2	4.30E-06		4.00E-06		4.70E-06		3.20E-06
12/08/2013	US	-11	7.10E-06			8.30E-06	2.80E-06	3.40E-06	
	DS	-11	3.20E-06				1.90E-06	3.30E-06	
23/09/2013	US	-10							
	DS	-10	1.60E-06			4.30E-06	3.50E-06	2.80E-06	

B.7.4. Pore size development over time

Each suction head corresponds to an effective pore diameter when using the Young-Laplace equation (Equation 3). Using that approach, the pore size distribution at each depth over time can be derived, averaged for up- and downslope (Figure 53). It can be seen that at a depth of 0.05 m the amount of medium pores decreased while the percentage of fine pores increased. However, this change was most likely negated over time by the influences of bioturbation and soil aggregation (Melchior+Wittpohl, 2014a). For the other depths the share in volume of the pores remained stable except for the wide coarse pores. However, their decrease is most likely of little influence on the flow of water as the medium and fine coarse pores are the most important for that (Blume et al., 2016).

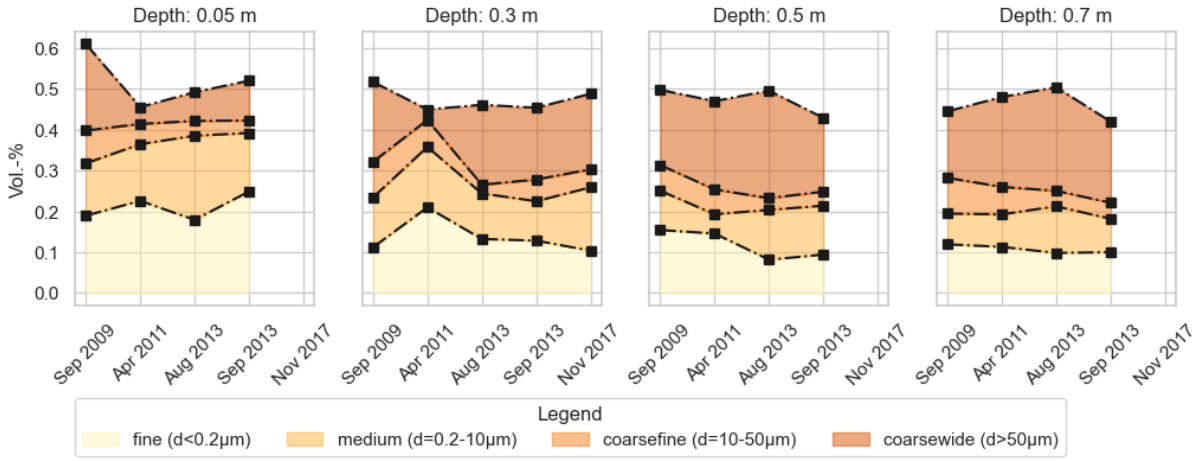

Figure 53: The derived pore size distribution at each depth over time. The measurements of August and September 2013 are the average of the up- and downslope measurements.

C. Methodology

C.1. Data cleaning

This appendix gives a detailed description of the steps taken to clean the precipitation, pump and tipping bucket switches and water content datasets.

C.1.1. Manual precipitation measurements

The logbook of the manual measurements mentions several sources of errors in the dataset. This subsection will treat differences between the two datasets and also indicate which values have been removed from the dataset.

For some readings there is a notable difference between the measurements of the gauge at ground level and at 1 meter height. The gauge at ground level was sometimes overgrown with grass (12-06-2019, 09-10-2022 and 02-08-2022) or occupied by insects (11-09-2013). On the contrary, the gauge at 1 meter height has lower values for days with snow precipitation (21-02-2012, 28-01-2013). Snowfall is highly sensitive to wind and at 1 meter height the influence of wind is much stronger. Commonly this results in lower readings.

Moreover, four data points have been removed from the dataset. Two values (11-02-2013, 21-01-2019) were unreliable because the logbook mentioned the precipitation to be frozen. In the period before 06-12-2021 the gauge at 1 meter height had fallen, making this measurement unreliable too. Lastly, the measurement at 09-10-2022 is identical for both gauges but the logbook mentions grass blockage for the ground level gauge and indicated that its value is uncertain. Therefore, this values was removed as well.

C.1.2. Pluvio-2 precipitation measurements

This subsection describes the errors found in the precipitation timeseries of the Pluvio-2 rain gauge. The raw precipitation data was registered cumulatively from which discrete precipitation was calculated. The discrete precipitation was calculated as the difference between two subsequent data points. There was one machine reset at 11-10-2021 where the cumulative rainfall was reset to zero. For this data point the discrete precipitation is zero as well.

Unreliable zero measurements

There are several periods where Pluvio, in contrast to the manual and KNMI rain gauges, measures no rainfall. There are listed in Table 9. The data range for which Pluvio data were deleted was chosen based on where it ended and started again matching the manual and KNMI data.

During 2018 the Pluvio rain gauge was damaged because of water coming into the mother board, which caused the large zero data period from August to December. After this the Pluvio rain gauge was replaced.

Table 9: Periods of unreliable zero measurements of Pluvio.

Period	Data deleted from	Data deleted to	Figure
April 2010	11-04-2010 12:00:00	05-05-2010 13:00:00	Figure 54
September 2013	02-09-2013 10:00:00	24-09-2013 08:30:00	Figure 54
June – August 2017	14-06-2017 13:00:00	31-08-2017 14:00:00	Figure 55
August – December 2018	24-08-2018 12:00:00	15-12-2018 00:00:00	Figure 55

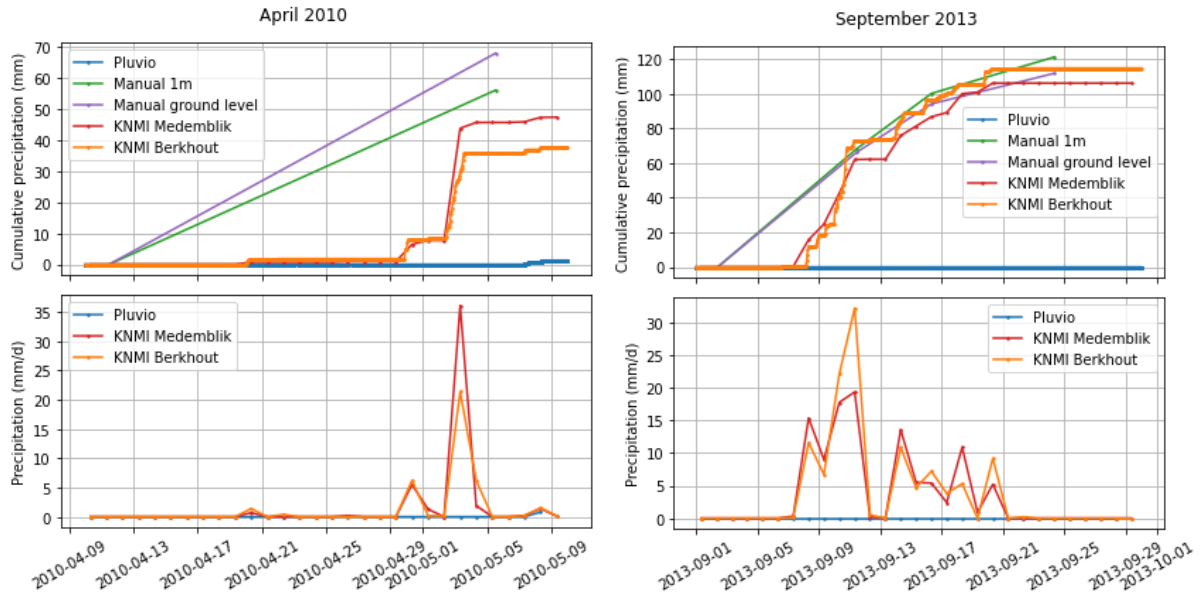

Figure 54: Unreliable zero measurements of the Pluvio rain gauge at the end of April 2010 (left) and September 2013 (right).

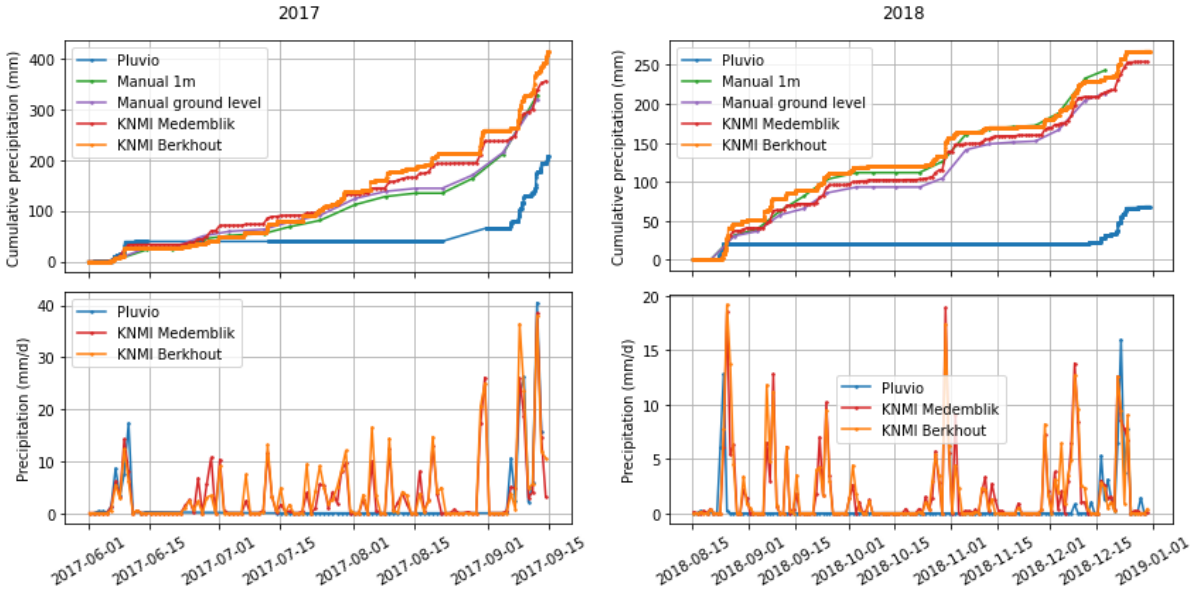

Figure 55: Unreliable zero measurements of the Pluvio rain gauge from June to August 2017 (left) and August to December 2018 (right).

Negative duplicate data

Between October 2011 and February 2012 the raw data shows an unexpected pattern where there are duplicate data in some measurement intervals. When calculated to discrete values the second reading is always negative. This happens for the tipping bucket and pump switches as well. These data are all registered by CARS so it was assumed that CARS corrects itself after counting too much in the first measurement. Therefore, the first data point is removed from the cumulative dataset, which also prevents the negative discrete values when recalculating the discrete data from the cumulative measurements.

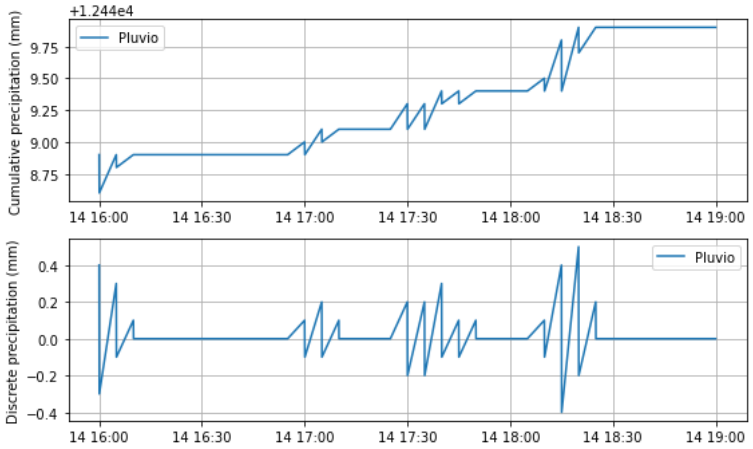

Figure 56: Example of unexpected behavior between October 2011 and February 2012 on 14-12-1011 where some measurement intervals contain duplicate measurements where the second values is a decrease (cumulative data) or negative value (discrete data).

Data jumps and other outliers

At the beginning of the measurement period between 01-10-2009 and 22-10-2009 the gauge measures a constant discrete precipitation of 7.5 mm every 5 minutes. These values were discarded as they are not realistic and probably a machine error.

Additionally, there are two measurements where there is a jump in the cumulative data (Table 9 and Figure 57). These are likely to be an error in the CARS registering because their magnitude is unrealistic and they are not registered by reference gauges. Therefore, they have been removed from the dataset.

Table 10: Data jumps in Pluvio data

Year	Discrete value (mm/5min)	Date of data jump
2014	132.4	12-09-2014 10:50:07
2022	838860.8	04-04-2022 04:09:20

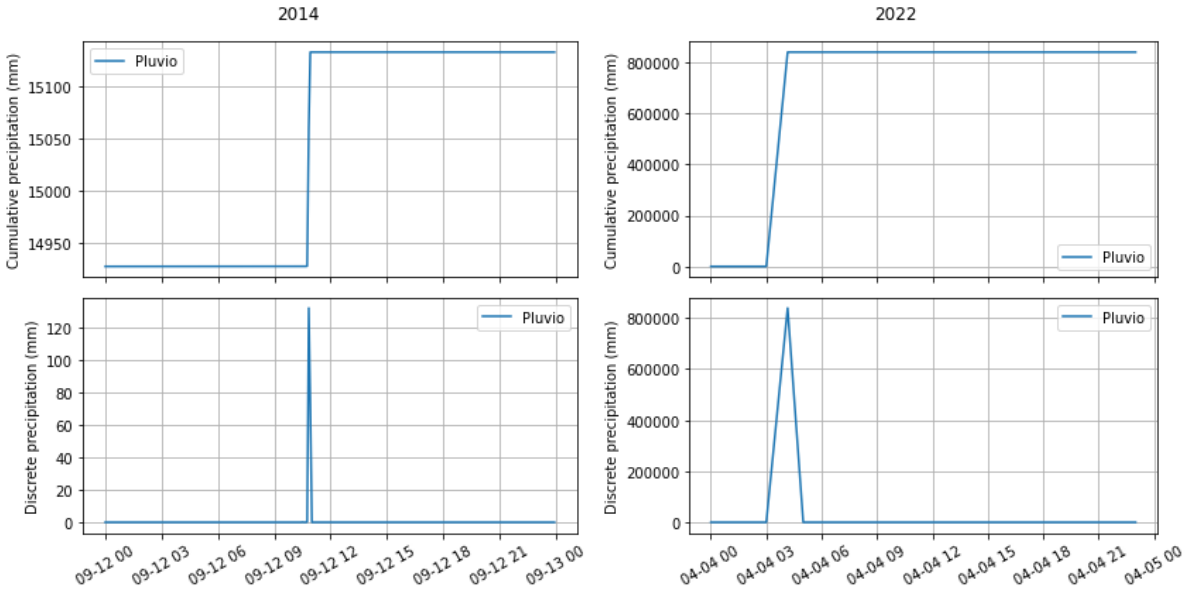

Figure 57: Outliers in Pluvio data in 2014 (left) and 2022 (right)

C.1.3. Tipping bucket switches

This subsection describes the errors found and removed from the two (CL and CB) tipping bucket switches timeseries. Similarly to the Pluvio precipitation data the data was registered cumulatively (Figure 58). This data was cleaned by calculating discrete values from the cumulative measurements and removing any invalid discrete measurements as described in the following subsections. After this, the cleaned cumulative data was recalculated from the clean discrete data.

The discrete values were calculated by computing the difference between two subsequent data points. For the CL, the counter resets at 22-09-2010, 29-01-2012, 07-10-2013, 15-01-2015, 20-01-2016, 30-11-2017, 16-03-2019, 08-03-2020, 14-06-2021, 11-10-2021 and 11-11-2021. For CB this happens at 20-01-2015, 17-06-2021, 11-10-2021 and 11-11-2021. For these data points and for the first data point of the whole series the cumulative value itself was used as discrete value, assuming that it started counting from 0 again. Because the value at which the counter resets is not constant, any switches measured before the counter resets in the time intervals containing a counter reset were lost.

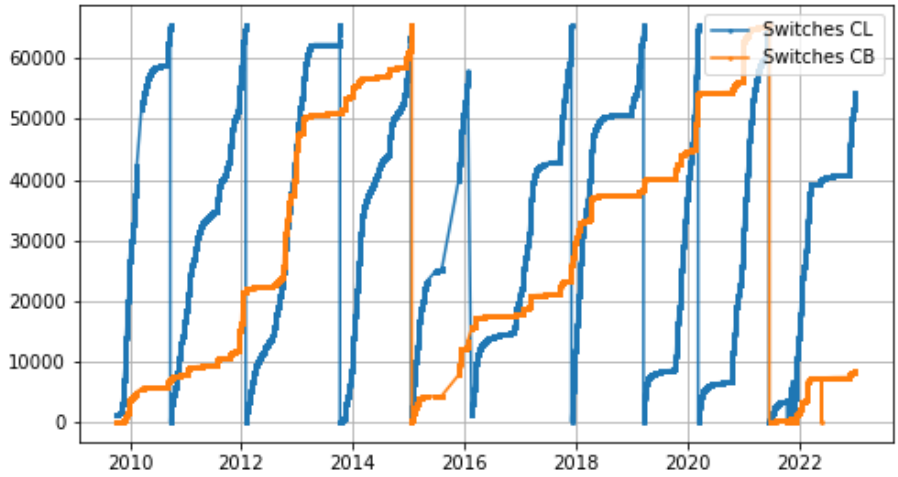

Figure 58: Tipping bucket switches raw data

Unreliable zero measurements

There are some periods in which the measurement of zero tipping bucket switches is unreliable. These are listed in Table 11 and shown in Figure 59 and Figure 60. In the period of August 2011 there is a sudden stop in the registering of switches both for the CL and the CB, whereas before and after this period there is a regular pattern of counted switches. As this is unlikely behaviour for subsurface flow these zero measurements were deleted.

The switches counted for the CL between March and October 2013 also shows unexpected behaviour. No switches were recorded except for some small time frames with sudden relatively large peaks (April and beginning of October). These zero measurements seem unlikely because there has fallen considerable precipitation in the same period and were deleted accordingly. The small peaks were also regarded as non-valid because small sudden peaks are non-typical measurements for the CL.

Lastly, in 2022 the switches of the CL showed a typical exponential decrease which was suddenly interrupted by a zero-measurement period. The logbook mentions that around this period the sensors measuring the amount of switches were replaced, which might be the cause for this unlikely data. These measurements were removed from the dataset. The peak at the end of this period is not high enough to be the accumulation of the switches of this entire period, so it was discarded as well.

Data jumps and other outliers

The tipping bucket switch data sometimes shows a sudden jump in cumulative count. This results in unrealistically large values when calculating to discrete values. Table 12 lists those occurrences. These have been removed from the dataset.

Furthermore, as explained for the Pluvio rain data in Subsection C.1.2, the tipping bucket switches also shows negative duplicate data. These have been removed in the same way as described for the precipitation data.

Table 11: Periods of unreliable zero measurements of tipping bucket switches.

Period	Layer	Data deleted from	Data deleted to	Figure
August, 2011	CL, CB	26-08-2011 10:00:00	29-08-2011 10:00:00	Figure 59
March to October, 2013	CL	23-03-2013 17:00:00	05-10-2013 04:30:04	Figure 59
March to May, 2022	CL	19-03-2022 01:00:00	04-05-2022 14:00:00	Figure 60

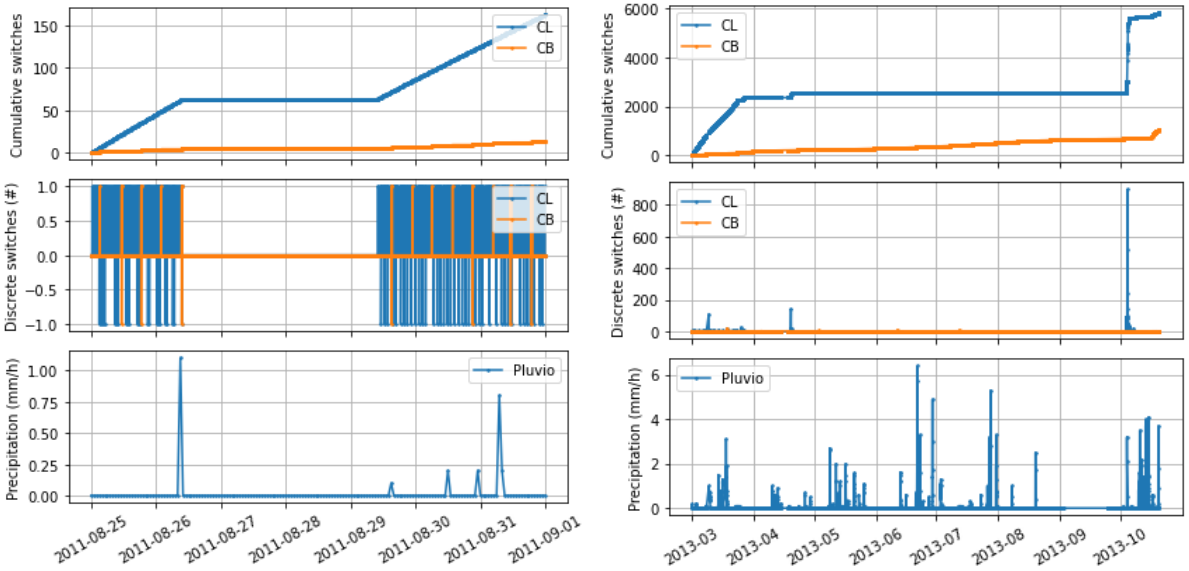

Figure 59: Cumulative and discrete switches together with the precipitation for unreliable zero measurement periods: August 2011 (left) and March-October 2013 (right).

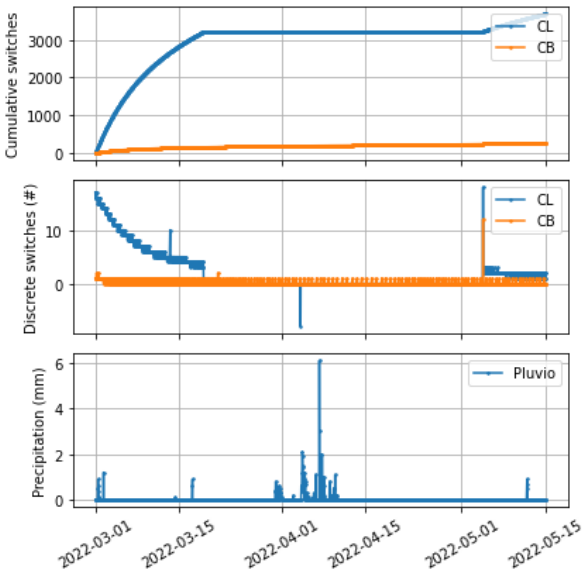

Figure 60: Cumulative and discrete switches together with the precipitation for the unreliable zero measurement period from March to May 2022.

Table 12: Data jumps in tipping bucket switches

Year	Date of data jump	Layer	Discrete value	Figure
2016	24-03-2016 14:00:09	CL, CB	CL: 10, CB: 9	Figure 61
	12-10-2016 12:00:02	CL, CB	CL: 7, CB: 14	
2018	09-11-2018 10:00:07	CL, CB	CL: 8, CB: 10	Figure 62
2022	04-05-2022 13:00:05	CB	16	Figure 62
	25-05-2022 14:00:00		41	
	25-05-2022 16:00:00		7197.3	

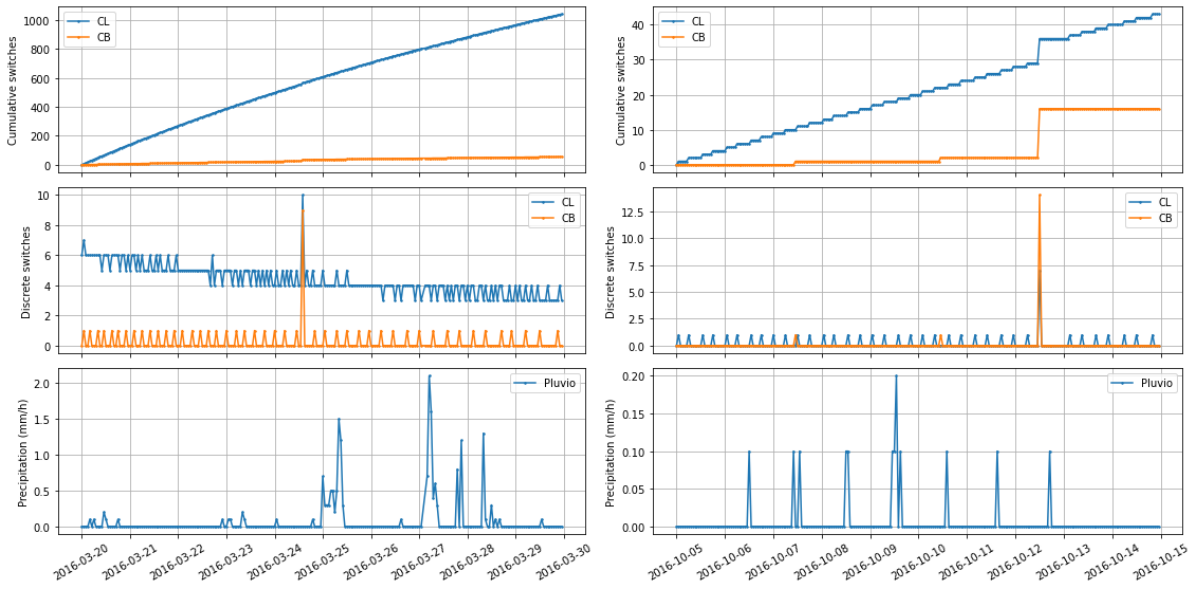

Figure 61: Data jumps of tipping bucket series CL and CB in 2016.

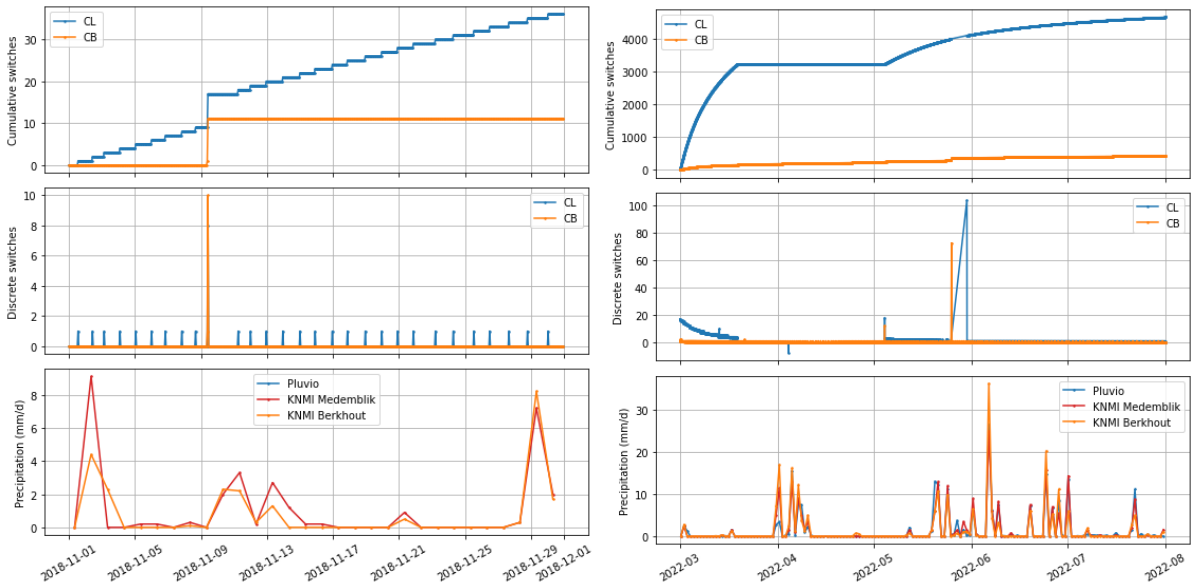

Figure 62: Data jumps of tipping bucket series for CL and CB in 2018 (left) and CB in 2022 (right).

C.1.4. Pump switches

Similarly to the Pluvio and tipping bucket switches data, the pump switches were also measured cumulatively (Figure 63). The procedure to arrive at cleaned data was done similarly by calculating discrete values from the cumulative measurements, removing any invalid discrete measurements and recalculating the cumulative data from the clean discrete data.

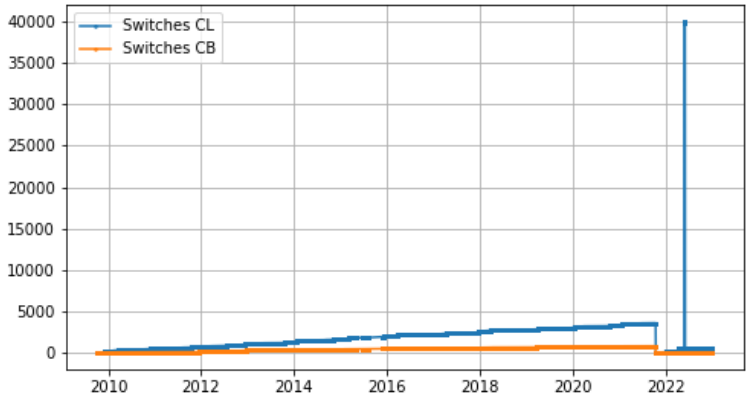

Figure 63: Raw pump switch data

The counter of cumulative pump switches resets at 11-10-2021 and 11-10-2021, similar to the other data registered by CARS.

The pump switch timeseries also contained the negative duplicate values as explained under subsection C.1.2. The same approach to remove them was used.

Furthermore, both timeseries contain a few data jumps. Firstly, between 13:00 and 16:30 on 25-05-2022 a non-integer value was logged after which there was a large jump in switches for both CL and CB (Figure 64). For CL the cumulative count stays at this elevated levels until it returns to its original value on 30-05-2022 11:00. Additionally, on 04-04-2022 another data jump occurred for the CL pump switches (Figure 64). These values were likely to be a machine error and were removed from the timeseries.

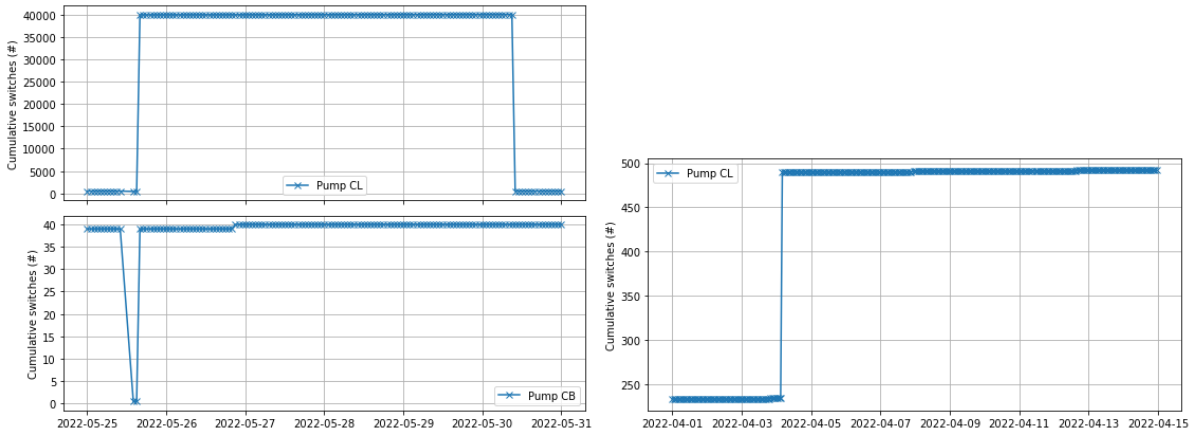

Figure 64: Machine error between 25-05-2022 and 30-05-2022 for CL and CB (left) and on 04-04-2022 for CL.

C.1.5. Water content

The raw water content data is shown in Figure 65. Negative water content measurements have been removed from the dataset.

Additionally, there is a small period in the first half of February 2012 where an unexpected temporary dip in water contents at 5 cm depth is registered. As this happened gradually and there was also a drying of the toil soil at the other locations these readings were not deleted.

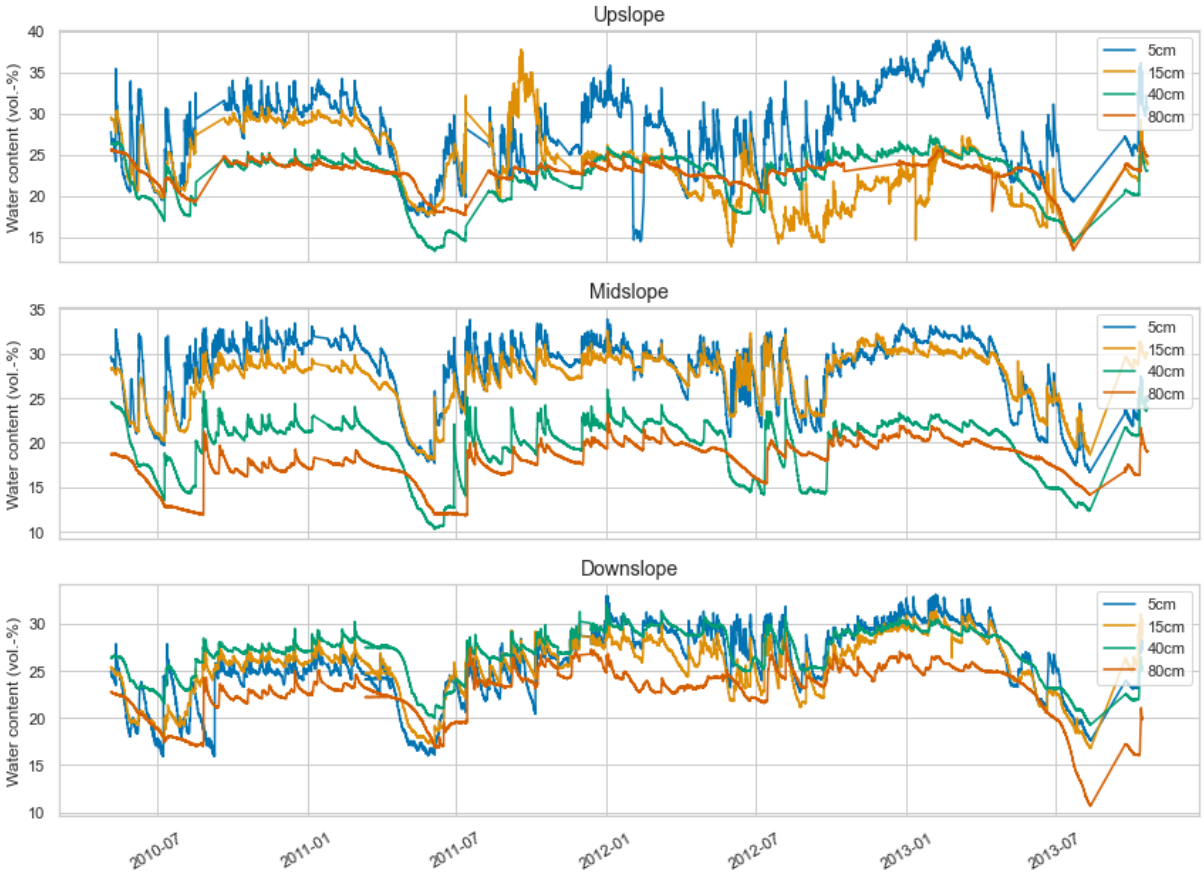

Figure 65: Raw water content data

C.2. Final outflow series

The final discharge timeseries used in the analysis consists of tipping bucket data where pump data has been inserted in case the tipping bucket data were unreliable. The periods for which this was done are shown in Table 13.

Table 13: Periods for which the pump outflow data was inserted in the tipping bucket outflow data to compensate for missing data.

Layer	Period start	Period end
CL	10:00 26-08-2011	10:00 29-08-2011
	17:00 23-03-2013	05:00 05-10-2013
	01:00 19-03-2022	14:00 04-05-2022
CB	10:00 26-08-2011	10:00 29-08-2011

C.3. Data validity

C.3.1. Tipping bucket volume

The measurements of the tipping bucket volume were done approximately monthly (Figure 66). The bucket volume was measured before and after cleaning it. Especially in the beginning of the measurement period this resulted in different volumes because the tipping buckets would be filled with (iron) precipitates forming in the outflow. These measurements contain errors, however, as for some measurements the volume of the dirty bucket would be higher than the cleaned bucket.

Also there are systematic biases visible in the measurement volume. These are likely the result of many different people performing the measurements. The measured volume is for instance sensitive to the speed of filling the bucket, which can very per person.

Because of these errors the mean of all measurements was used for the complete measurement period. The measured values vary between 4% of this value for both layers.

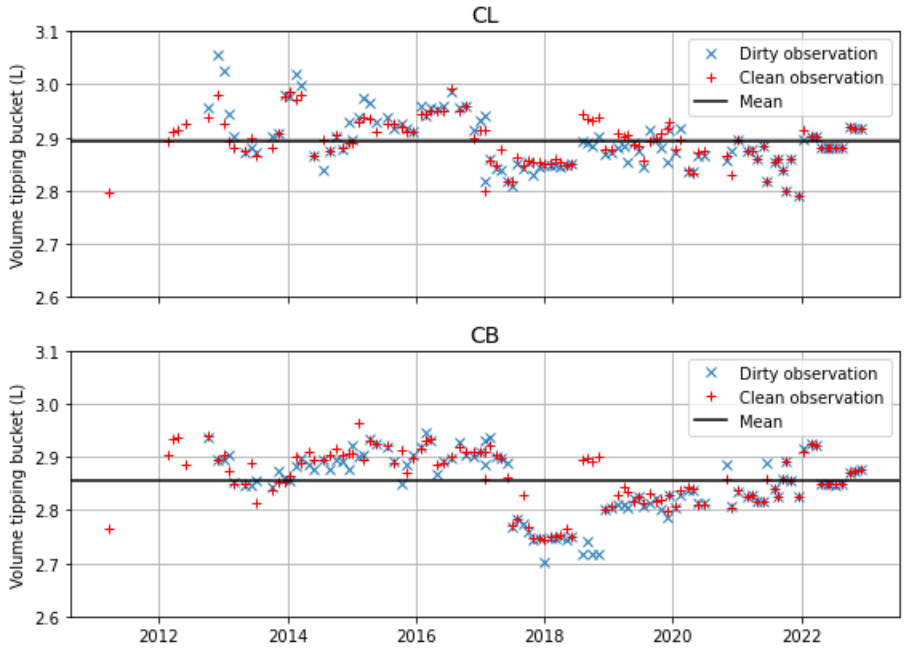

Figure 66: Measurements of the tipping bucket volumes

C.3.2. Comparison pump and tipping bucket outflow

The cumulative outflow calculated with the pump and tipping bucket switches for the CL and CB are shown in Figure 67. In general, they are in good agreement. For the CL there is a discrepancy between the two outflows at the end of 2013. This could be caused by the reconstruction of the top of the test field that was carried out at that time. Moreover, between October and December 2012 there is a difference between the two flows for the CB which cannot be explained.

There is uncertainty in both outflows, since the tipping of the tipping bucket depends not only on the volume inside the bucket, but also on the outflow speed. During high outflow events this might result in an overestimation of the CB outflow.

Similarly, the assumed volume per pump switch was not verified. Additionally, as emptying the IBM tank takes approximately 5 minutes. Any additional tipping bucket

volumes discharged within this time enlarge the actual pumped volume. At an outflow rate of 1 mm/h this could result in an underestimate of the flow by 10%.

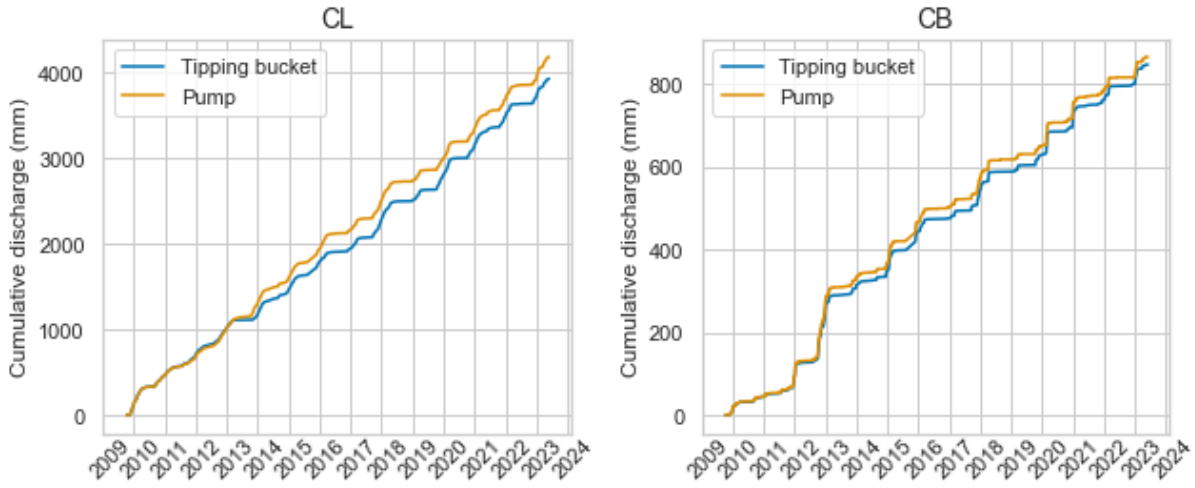

Figure 67: Cumulative outflow calculated using the pump and tipping bucket switches for the CL and CB.

C.3.3. Comparison precipitation datasets

Figure 68 shows the yearly precipitation of the three local rain gauges and the KNMI stations of Berkhout and Medemblik. These are located in the proximity of the landfill Wieringermeer. The station in Medemblik (~1 km away) measures daily precipitation amounts between 08.00 the preceding day and 08.00 on the current day. The station at Berkhout is located approximately 15.5 km away but measures precipitation on an hourly time scale automatically

In general, the two manual rain gauges have similar values with the rain gauge at ground level measuring more. The Pluvio-2 automatic rain gauge has some years with similar precipitation as the manual rain gauges, but in some years is differs greatly (e.g. 2010, 2013, 2018, 2021). Both KNMI stations have similar yearly rainfall amounts. Most of the years the manual rain gauge at ground level measures more rainfall than the KNMI stations. The manual rain gauge at 1 meter height has similar values, but can also be much higher (2010, 2018, 2020) or much lower (2021, 2022). In years like 2011, 2014, 2015, 2019 and 2022 the Pluvio-2 rain gauge measures very similar amounts as the KNMI stations, but in the other years it has much different values.

Figure 69 shows the correlation between the two manual rain gauges and between them and the automatic rain gauge respectively. The values are the accumulated rainfall at the time of the manual measurement, which was done with a time interval of a week or a month. The manual precipitation meters well correlated. In contrast, there is still correlation between the automatic and manual rain gauges but it is less well pronounced. There are some occurrences of no precipitation at the one gauge while the other measures rain up to 50 mm. In general, the manual rain gauges measure more rain than the automatic rain gauge.

When plotting the correlation between the manual rain gauges and the KNMI station at Medemblik, there is some correlation (Figure 70). However, there are some observations where the manual rain gauges measures no precipitation whereas the KNMI station measures up to 50 mm of rainfall.

The correlation of the Pluvio rain gauge with the KNMI station in Medemblik is quite strong (Figure 71). Compared to the Berkhout station there is the biggest difference in measurements of extreme precipitation (>30 mm). Those events can happen at small scale and thus this difference might be due to randomness. Considering that the correlation between Berkhout and Medemblik is stronger and does not have this difference, reinforces the idea that the Pluvio measurements are biased.

As the local precipitation measurements seem to contain error and inconsistencies when compared to each other and to KNMI measurements, instead the KNMI data will be used for modelling the water balance of the test field.

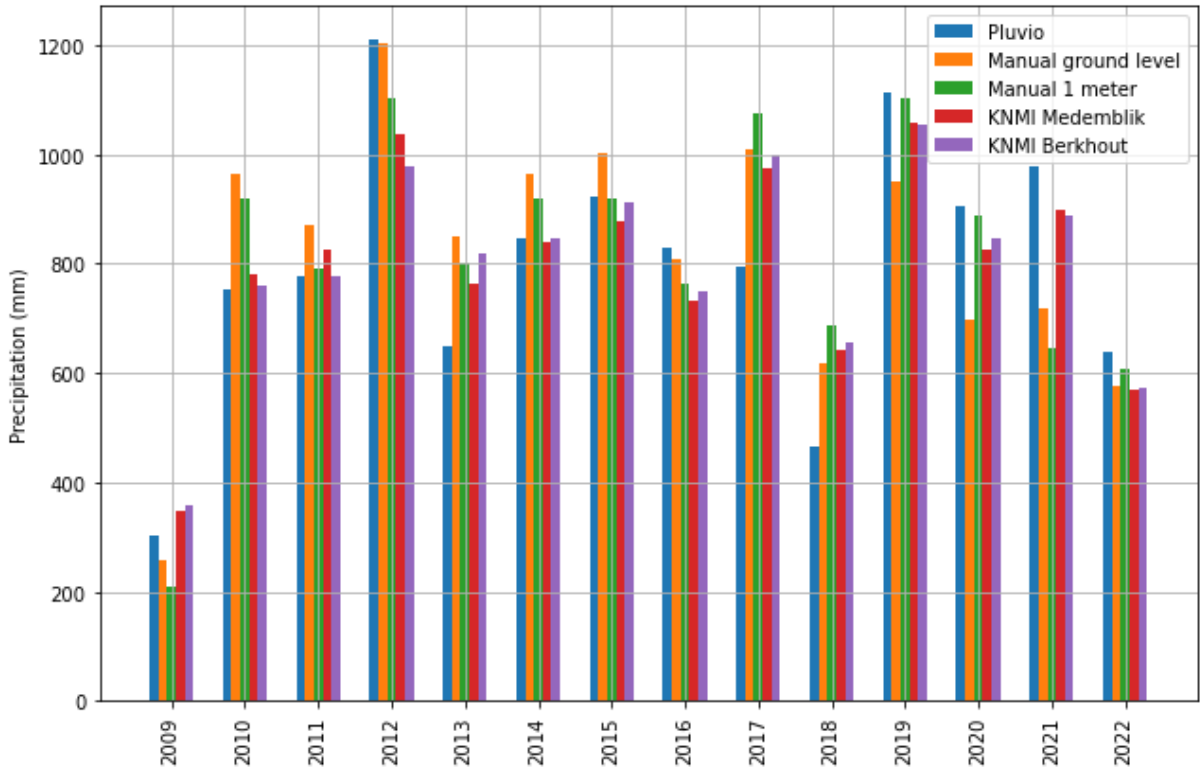

Figure 68: Yearly rainfall of the three rain gauges on the test field of Wieringermeer and of KNMI stations Medemblik and Berkhout.

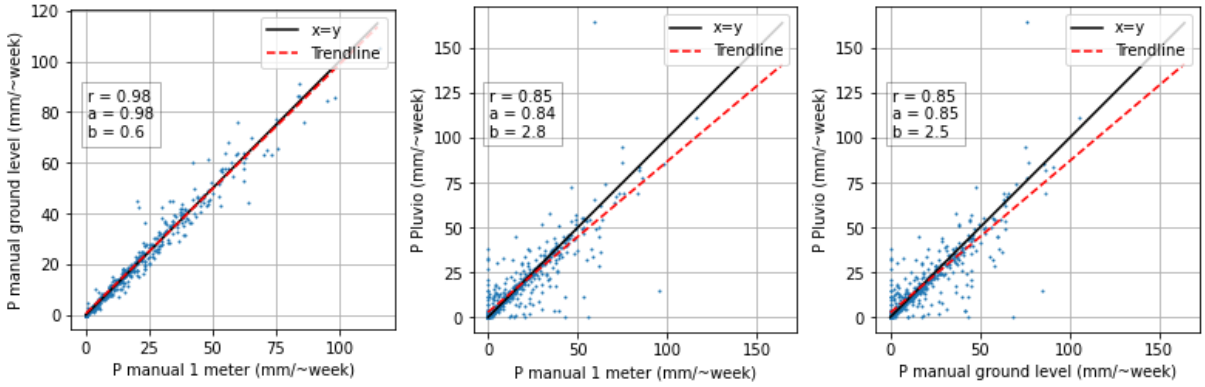

Figure 69: Correlation of accumulated precipitation on times of manual measurements for the rain gauge at ground level against the gauge at 1 meter height an the Pluvio-2 rain gauge.

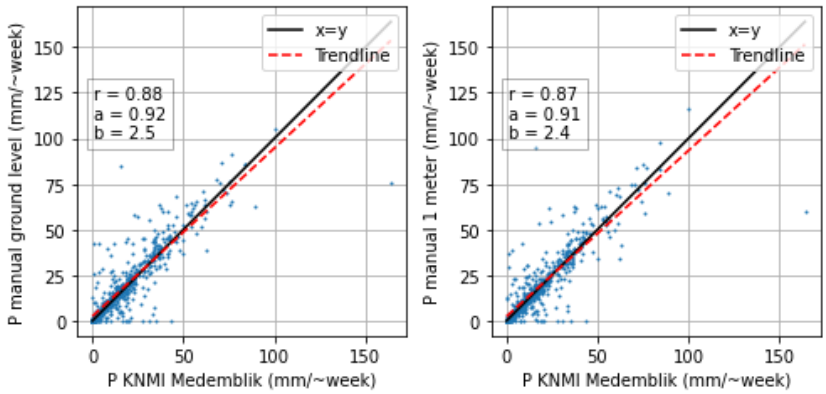

Figure 70: Correlation of the manual rain gauges with the KNMI Medemblik station.

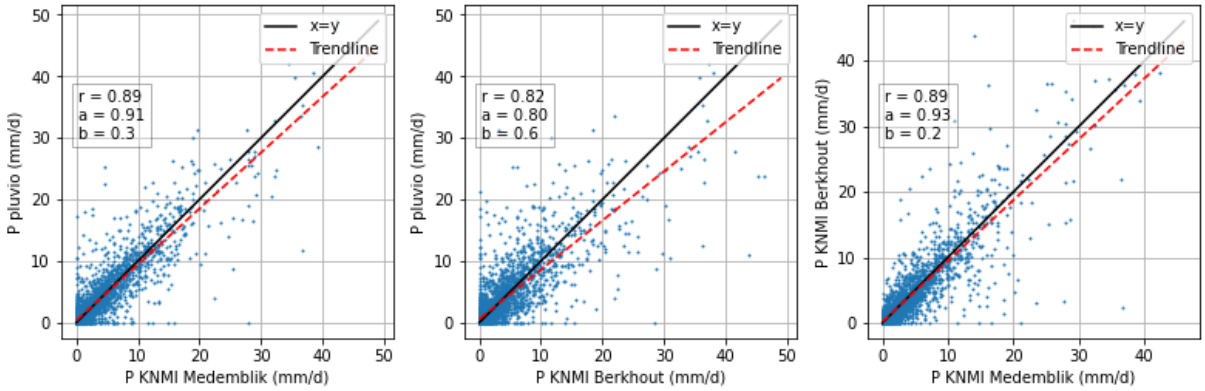

Figure 71:Correlation of the Pluvio-2 rain gauge with the Berkhout (left) and Medemblik (center) KNMI stations and the correlation between the two KNMI stations (right) on daily scale.

C.4. Derivation of Richards' equation solved by the model

Flow through soils is commonly described by Darcy's law:

$$\boldsymbol{q_w} = -\boldsymbol{k}\nabla h_t \qquad \text{Equation 34}$$

Richards' equation is derived by combining this law with the principle of the conservation of mass. The latter enforces that the net outflow is equal to the change in storage in a finite soil volume:

$$\frac{\partial(\theta_w \rho_w)}{\partial t} = -\rho_w \nabla \boldsymbol{q_w} \qquad \text{Equation 35}$$

When only considering vertical flow and inserting Darcy's law this simplifies to:

$$\frac{\partial(\theta_w \rho_w)}{\partial t} = -\rho_w \frac{\partial q_w}{\partial z} = -\rho_w k \frac{\partial h_t}{\partial z} \qquad \text{Equation 36}$$

Next we insert Equation 2 and Equation 6:

$$\frac{\partial(\theta_w \rho_w)}{\partial t} = -\rho_w k_s k_r(h_m) \frac{\partial(h_m + h_z)}{\partial z} = -\rho_w k_s k_r(h_m) \left(\frac{\partial h_m}{\partial z} + 1\right) \qquad \text{Equation 37}$$

The left hand side of the equation above can be extended to account for the compressibility of the soil matrix and water (Heimovaara, 2022). First we write $\theta_w = S_e n$ with n the porosity of the soil [-]. The left hand side can then be written as:

$$\begin{aligned} \frac{\partial(\theta_w \rho_w)}{\partial t} = \frac{\partial(S_e n \rho_w)}{\partial t} &= n\rho_w \frac{\partial S_e}{\partial t} + S_e \rho_w \frac{\partial n}{\partial t} + S_e n \frac{\partial \rho_w}{\partial t} \\ &= \rho_w \frac{\partial \theta_w}{\partial t} + S_e \left(\rho_w \frac{\partial n}{\partial t} + n \frac{\partial \rho_w}{\partial t}\right) \end{aligned} \qquad \text{Equation 38}$$

Using the chain rule and by defining the differential water capacity $C(h_m) = \frac{\partial \theta_w}{\partial h_m}$, the first term can be rewritten as:

$$\rho_w \frac{\partial \theta_w}{\partial t} = \rho_w \frac{\partial \theta_w}{\partial h_m} \frac{\partial h_m}{\delta t} = \rho_w C(h_m) \frac{\partial h_m}{\partial t} \qquad \text{Equation 39}$$

The second term can be written as:

$$S_e \left(\rho_w \frac{\partial n}{\partial t} + n \frac{\partial \rho_w}{\partial t}\right) = S_e \left(\rho_w \frac{\partial n}{\partial h_m} + n \frac{\partial \rho_w}{\partial h_m}\right) \frac{\partial h_m}{\partial t} \qquad \text{Equation 40}$$

With p_w the water pressure [Pa].

The change in porosity is the compressibility of the soil matrix and is defined as:

$$C_v = \frac{dn}{dh_m} \qquad \text{Equation 41}$$

With C_v the compressibility of the soil matrix [1/m].

The relative change in density is the compressibility of water which reads as:

$$\beta_w = \frac{1}{\rho_w} \frac{d\rho_w}{dh_m} \qquad \text{Equation 42}$$

With β_w the compressibility of water [1/m].

Putting Equation 40, Equation 41 and Equation 42 together gives:

$$S_e(\rho_w C_v + n\rho_w \beta_w) \frac{\partial h_m}{\partial t} \qquad \text{Equation 43}$$

Which simplifies to when defining $S_s = (C_v + n\beta_w)$:

$$S_e \rho_w S_s \frac{\partial h_m}{\partial t} \qquad \text{Equation 44}$$

With S_s the specific storage [1/m].

To complete the expansion of the left hand term we combine Equation 37, Equation 38, Equation 39 and Equation 44:

$$\rho_w C(h_m) \frac{\partial h_m}{\partial t} + S_e \rho_w S_s \frac{\partial h_m}{\partial t} = -\rho_w k_s k_r(h_m) \left(\frac{\partial h_m}{\partial z} + 1 \right) \qquad \text{Equation 45}$$

Assuming the density of water doesn't change significantly results in:

$$(C(h_m) + S_e S_s) \frac{\partial h_m}{\partial t} = -k_s k_r(h_m) \left(\frac{\partial h_m}{\partial z} + 1 \right) \qquad \text{Equation 46}$$

Finally, a source term S_r [m^3 water / m^3 soil / s] is introduced which can be used to incorporate root water uptake (Feddes & Raats, 2004):

$$(C(h_m) + S_e S_s) \frac{\partial h_m}{\partial t} = -k_s k_r(h_m) \left(\frac{\partial h_m}{\partial z} + 1 \right) + S_r \qquad \text{Equation 47}$$

C.5. Python model

All the scripts that were used for the analysis and modelling can be found at: https://github.com/markvdb1997/WB_Wieringermeer . Figures were made using the Seaborn Python library (Waskom, 2021).

C.5.1. Concept

The model solves Richards' equation (Equation 10) by linearising it using a finite difference method. The soil is divided into N elements of equal length. All variables and properties are evaluated at the node i in the centre of the layer, except for the first and last element where the evaluation node is located at the edges of the soil profile. The flux is calculated at the edges of the layers, where the edges associated with layer i are j and $j+1$ (Figure 72).

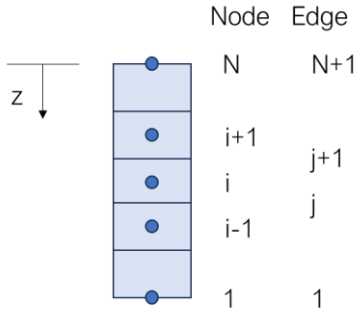

Figure 72: Conceptual visualisation of finite difference scheme

The suction heads are subsequently calculated by solving the system of linear equations:

$$M(t,h_m)\frac{\Delta h_m}{\Delta t} = F(t,h_m) \qquad \text{Equation 48}$$

With M the mass matrix and F the divergent water flux.

The mass matrix M is defined as the diagonal matrix:

$$M(t,h_m) = \begin{bmatrix} C'_{w,1} & 0 & \dots & & \\ 0 & \ddots & & & \\ \vdots & & C'_{w,i} & & \\ & & & \ddots & \\ & & & & C'_{w,N} \end{bmatrix} \qquad \text{Equation 49}$$

With $C'_{w,i} = C(h_{m,i}) + S_{e,i}S_{s,i}$ the storage of moisture in layer i.

The divergent water flux matrix is calculated as:

$$F(t,h_m) = \begin{bmatrix} F_1 & 0 & \dots & & \\ 0 & \ddots & & & \\ \vdots & & F_i & & \\ & & & \ddots & \\ & & & & F_N \end{bmatrix} \qquad \text{Equation 50}$$

With $F_i = -\frac{q_{w,j+1}-q_{w,j}}{\Delta z_i} - S_{r,i}(z_i)$ where $q_{w,j}$ is the flux of water from layer i to $i-1$ (similar for $q_{w,j+1}$) [m T^{-1}] and $S_{r,i}$ the root water uptake in node i [T^{-1}] (Equation 17). The flow between layer i and $i-1$ is calculated as the minimum of the hydraulic conductivity evaluated at both layers multiplied by the difference in total head between the two cells:

$$q_{w,j} = -\min\left(k_{s,i}k_r(h_{m,i}),\ k_{s,i-1}k_r(h_{m,i-1})\right)\left(\frac{h_{m,i}-h_{m,i-1}}{\Delta z_i}+1\right) \qquad \text{Equation 51}$$

Note that upward flow is denoted positively.

C.5.2. Python code

Function that initiates and runs the model

```
#!/usr/bin/env python3
# -*- coding: utf-8 -*-
"""
Created on Sun Apr 23 17:17:49 2017
@author: theimovaara
Modified by Mark van den Brink on 01-06-2023
"""
import numpy as np
import pandas as pd

# Richards flow class
import model.RichardsODEClassMB as rfun


# In[1:] Model domain and soil properties
def run_richard(layers, scale, N,
                alpha, n, thetaS, thetaR, Ksat,
                rL_b, rL_hvals,
                Rb, dHb):

    def modDim(dtot, nIN):
        zIN = np.linspace(-dtot, 0, num=nIN).reshape(nIN, 1)
        zN = np.zeros(nIN - 1).reshape(nIN - 1, 1)
        zN[0, 0] = zIN[0, 0]
        zN[1:nIN - 2, 0] = (zIN[1:nIN - 2, 0] + zIN[2:nIN - 1, 0]) / 2
        zN[nIN - 2, 0] = zIN[nIN - 1]
        nN = np.shape(zN)[0]
        ii = np.arange(0, nN - 1)
        dzN = (zN[ii + 1, 0] - zN[ii, 0]).reshape(nN - 1, 1)
        dzIN = (zIN[1:, 0] - zIN[0:-1, 0]).reshape(nIN - 1, 1)
        # collect model dimensions in a pandas series: mDim
        mDim = {'zN': zN,
                'zIN': zIN,
                'dzN': dzN,
                'dzIN': dzIN,
                'nN': nN,
                'nIN': nIN
                }
        return zN, dzIN, pd.Series(mDim)

    def soilPar(zN, alpha, n, thetaS, thetaR, Ksat, rL_b, rL_hvals):
        def VGparams_layers(zLtopArr, par):
            pArr = np.ones(np.shape(zN))
            for i, zLtop in enumerate(zLtopArr):
                pArr[zN <= zLtop] = par[i]
            return pArr
        # collect soil parameters in a pandas Series: sPar
        sPar = {'vGA': VGparams_layers(zLtop, alpha),  # alpha[1/m]
                'vGN': VGparams_layers(zLtop, n),  # n[-]
                'vGM': 1 - 1 / VGparams_layers(zLtop, n),  # m = 1-1/n[-]
                'thS': VGparams_layers(zLtop, thetaS),  # saturated water content
                'thR': VGparams_layers(zLtop, thetaR),  # residual water content
                'KSat': VGparams_layers(zLtop, Ksat),  # [m/day]
                'vGE': 0.5,  # power factor for Mualem-van Genuchten
                'Cv': np.ones(np.shape(zN)) * 1.0e-8,  # compressibility [1/Pa]
                'rL_b': rL_b,
                'rL_zr': -1.1,
                'rL_lambda': 1,
                'rL_hvals': rL_hvals,  # root water uptake reduction function parameters
                }
        return pd.Series(sPar)

    def bcPar(Rb, Hb):
        def BndqWatTop(t, bPar, scale):
            if np.size(t) == 1:
                t = np.array([t])
            qBnd = np.zeros(len(t))
            for ii in range(len(t)):
                key = 'num_date' if scale == '1D' else 'num_hour'
                xy, md_ind, t_ind = np.intersect1d(bPar.meteo_data[key], np.floor(t[ii]),
                                                   return_indices=True, assume_unique=True)
```

```
                key = 'P_knmiBH' if scale == '1D' else 'P_cars_plv__dis'
                rf = bPar.meteo_data[key].iloc[md_ind].values
                qBnd[ii] = -rf
            return qBnd

        def BndqEvTop(t, bPar, scale):
            if np.size(t) == 1:
                t = np.array([t])
            qEv = np.zeros(len(t))
            for ii in range(len(t)):
                t_conv = t[ii] if scale == '1D' else t[ii]/24
                xy, md_ind, t_ind = np.intersect1d(bPar.meteo_data['num_date'],
np.floor(t_conv),  # Use floor instead of ceil because pandas resamples down instead of up
                                                   return_indices=True, assume_unique=True)
                pEv = bPar.meteo_data['ETp_knmiBH'].iloc[md_ind].values
                qEv[ii] = pEv  if scale == '1D' else pEv / 24
            return qEv
        # Read meteodata
        # meteo_data = pd.read_hdf('input')
        meteo_data = pd.read_hdf('model/input.h5')
        meteo_data['num_date'] = meteo_data.index.astype(np.int64)/(1e9*3600*24) # nr of day
        meteo_data['num_hour'] = meteo_data.index.astype(np.int64)/(1e9*3600) # nr of hour
        if scale == '1D':
            t_range = meteo_data['num_date']
        elif scale == '1H':
            t_range = meteo_data['num_hour']
        else:
            print("Scale not supported: " + scale)
        # Define top boundary condition function
        bPar = {'topBndFuncWat': BndqWatTop,  # topBndFuncWat(t,bPar)
                'topBndFuncpEv': BndqEvTop,
                'meteo_data': meteo_data,
                'bottomTypeWat': 'gravity',  # Robin condition or Gravity condition
                'kRobBotWat': Rb,  # Robin resistance term for bottom
                'hwBotBnd': Hb,  # pressure head at lower boundary
                }
        return t_range, pd.Series(bPar)

    # Geometry definitions
    dL = np.array(layers)  # Layer depth, from top to bottom layer
    dtot = dL.sum()
    zLtop = -np.cumsum(dL) + dL
    nIN = N  # elements number

    # Get parameters
    zN, dzIN, mDim = modDim(dtot, nIN)
    sPar = soilPar(zN=zN,
                   alpha=alpha,
                   n=n,
                   thetaS=thetaS,
                   thetaR=thetaR,
                   Ksat=Ksat,
                   rL_b=rL_b,
                   rL_hvals=rL_hvals
                   )
    t_range, bPar = bcPar(Rb, -dtot-dHb)
    # Initialize class with model domain, soil properties and boundary parameters
    myRC = rfun.RichardsUnsatFlow(sPar, mDim, bPar, scale)
    # Define initial conditions
    # hwIni = np.ones(np.shape(zN)) * (-zN + zN[0])  # hydrostatic
    hwIni = np.ones(np.shape(zN)) * -1  # around FC
    # Time Discretization
    Nt = 24 if scale == '1D' else 4  # day scale per hour, hour scale per 15 min
    tOut = np.linspace(t range[0], t range[-1], (len(t range)-1)*Nt+1)
    dt = np.diff(tOut)[0] if scale == '1D' else np.diff(tOut)[0] / 24

    # Solve
    hwODE = myRC.IntegrateWF(tOut, hwIni)
    return myRC, hwODE, zN, dzIN
```

Class that represents the model

```
#!/usr/bin/env python3
# -*- coding: utf-8 -*-
"""
Created on Sun Apr 23 17:17:49 2017
@author: theimovaara
Modified by MArk van den Brink 01-06-2023
"""
import numpy as np
import scipy.integrate as spi
import scipy.sparse as sp

class RichardsUnsatFlow:
    def __init__(self, sPar, mDim, bPar, scale):
        self.sPar = sPar
        self.mDim = mDim
        self.bPar = bPar
        self.scale = scale

    def SeFun(self, hw):
        hc = -hw
        Se = (1 + ((hc * (hc > 0)) * self.sPar.vGA) ** self.sPar.vGN) ** (-self.sPar.vGM)
        return Se

    def thFun(self, hw):
        Se = self.SeFun(hw)
        th = self.sPar.thR + (self.sPar.thS - self.sPar.thR) * Se
        return th

    def CFunCmplx(self, hw):
        dh = np.sqrt(np.finfo(float).eps)
        if np.iscomplexobj(hw):
            hcmplx = hw.real + 1j*dh
        else:
            hcmplx = hw.real + 1j*dh
        th = self.thFun(hcmplx)
        C = th.imag / dh
        return C

    def CPrimeFun(self, hw):
        # Function for calculating the MassMatrix including compression
        th = self.thFun(hw)
        Sw = th / self.sPar.thS
        Chw = self.CFunCmplx(hw)
        betaW = 4.5e-6  # compressibility of water [1/m]
        Ssw = self.sPar.Cv + self.sPar.thS * betaW
        cPrime = Chw + Sw * Ssw
        nN = self.mDim.nN
        nIN = self.mDim.nIN
        cPrime[nN-1] = 1/self.mDim.dzIN[nIN-2] * (hw[nN-1] > 0) + cPrime[nN-1] * (hw[nN-1]
<= 0)
        return cPrime

    def KFun(self, hw):
        nr, nc = hw.shape
        nIN = self.mDim.nIN
        Se = self.SeFun(hw)
        kN = self.sPar.KSat * Se ** 3
        kIN = np.zeros([nIN, nc], dtype=hw.dtype)
        kIN[0] = kN[0]
        ii = np.arange(1, nIN - 1)
        kIN[ii] = np.minimum(kN[ii - 1], kN[ii])
        kIN[nIN - 1] = kN[nIN - 2]
        return kIN

    def WatFlux(self, t, hw):
        nr, nc = hw.shape
        nIN = self.mDim.nIN
        dzN = self.mDim.dzN
        # Calculate inter nodal permeabilities
        kIN = self.KFun(hw)
        # Top boundary flux (Neumann flux)
        qBnd = self.bPar.topBndFuncWat(t, self.bPar, self.scale)
        qw = np.zeros([nIN, nc], dtype=hw.dtype)
        # Bottom boundary
        if self.bPar.bottomTypeWat.lower() == 'gravity':
```

```
            qw[0] = -kIN[0]
        else:
            qw[0] = -self.bPar.kRobBotWat * (hw[0]- self.bPar.hwBotBnd)
        # Flux in all intermediate nodes
        ii = np.arange(1, nIN - 1)  # does not include last element
        qw[ii] = -kIN[ii] * ((hw[ii] - hw[ii - 1]) / dzN[ii - 1] + 1)
        # Neumann at the top
        qw[nIN - 1] = qBnd
        return qw

    def RootUptakeReduction(self, hW):
        h1 = self.sPar.rL_hvals[0]
        h2 = self.sPar.rL_hvals[1]
        h3 = self.sPar.rL_hvals[2]
        h4 = self.sPar.rL_hvals[3]
        slope1 = 1/(h2-h1)
        slope2 = -1/(h4-h3)
        rwuR = (slope1 * (hW-h1) * (hW >= h1) * (hW < h2) +
                (hW >= h2) * (hW < h3) +
                (1+slope2*(hW-h3)) * (hW >= h3) * (hW < h4))
        return rwuR

    def RootWaterUptake(self, t, hw):
        mask = self.mDim.zN >= self.sPar.rL_zr
        rL = mask * np.exp(self.sPar.rL_b * self.mDim.zN)
        tot_rL = np.sum(rL * self.mDim.dzIN)
        betaR = rL * self.mDim.dzIN / tot_rL
        rwU_alpha = self.RootUptakeReduction(hw)
        pEv = self.bPar.topBndFuncpEv(t, self.bPar, self.scale)
        denom = np.sum(rwU_alpha * betaR**self.sPar.rL_lambda, axis=0)
        denom[denom == 0] = 1  # If 0, make 1 to avoid div by zero. Total rwU is still 0.
        rwU = rwU_alpha**2 * betaR**self.sPar.rL_lambda * pEv / denom
        return rwU

    def DivWatFlux(self, t, hw):
        nr, nc = hw.shape
        nN = self.mDim.nN
        dzIN = self.mDim.dzIN
        massMD = self.CPrimeFun(hw)
        qW = self.WatFlux(t, hw)
        # Calculate divergence of flux for all nodes
        ii = np.arange(0, nN)
        divqW = -(qW[ii + 1] - qW[ii]) / dzIN[ii]
        rwU = self.RootWaterUptake(t, hw) / dzIN
        rhsW = (divqW - rwU) / massMD
        # print(rhsW)
        return rhsW

    def IntegrateWF(self, tRange, iniSt):
        def dYdt(t, hW):
            # solver switches between zeroD and matrix shaped states
            # we need to take this into account to create a rate function that
            # works for every case...
            if len(hW.shape) == 1:
                hW = hW.reshape(self.mDim.nN, 1)
            rates = self.DivWatFlux(t, hW)
            return rates
        def jacFun(t, y):
            if len(y.shape) == 1:
                y = y.reshape(self.mDim.nN,1)
            nr, nc = y.shape
            dh = np.sqrt(np.finfo(float).eps)
            ycmplx = np.repeat(y, nr, axis=1).astype(complex)
            c_ex = np.eye(nr) * 1j * dh
            ycmplx = ycmplx + c_ex
            dfdy = dYdt(t, ycmplx).imag/dh
            return sp.coo_matrix(dfdy)
        # solve rate equation
        t_span = [tRange[0], tRange[-1]]
        int_result = spi.solve_ivp(dYdt, t_span, iniSt.squeeze(),
                                   method='BDF', vectorized=True, jac=jacFun,
                                   t_eval=tRange,
                                   rtol=1e-4
                                   )
        return int_result
```

C.6. Calibration process

C.6.1. Results of fitting van Genuchten curves to measurements

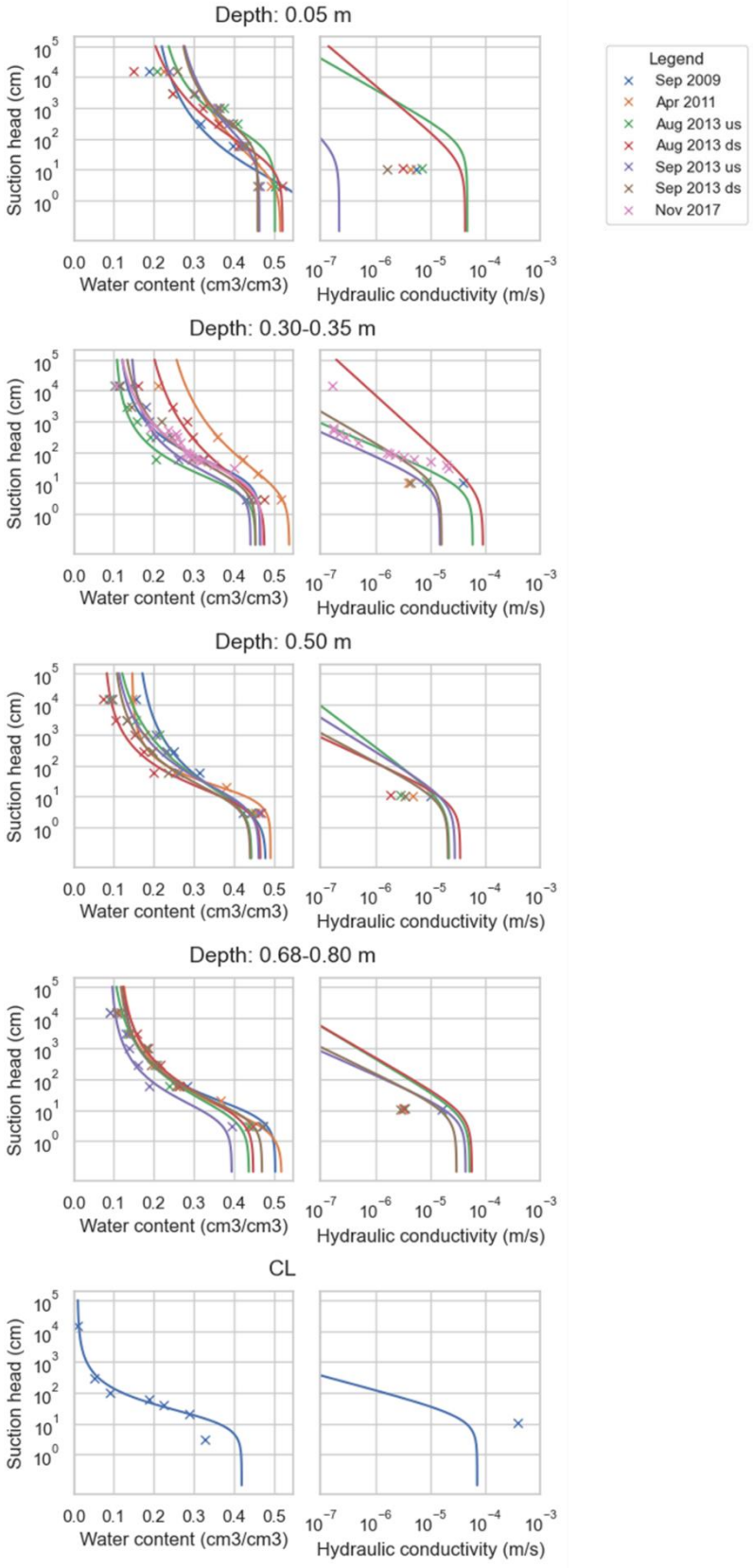

Figure 73: Fitted van Genuchten curves with the measurements. SHCCs were derived from the SWRC.

C.6.2. Initial model values and simulation results

The initial parameter values that were used as starting point for the calibration are shown in Table 14. The simulation results they generate are shown in Figure 13 and Figure 74.

Table 14: Initial values of model parameters.

Transpiration model					
α_w **thresholds [m]** (Feddes & Raats, 2004)	h_1	h_2	h_3	h_4	
	-0.1	-0.25	-5	-80	
***b* [-]**			10		
Soil hydraulic parameters					
	θ_r	θ_s	α [m^{-1}]	n	k_s [md^{-1}]
TS	0.19	0.51	5.0	1.24	3.88
SS	0.12	0.47	13.4	1.37	2.93
CL	0.01	0.42	6.3	1.70	6.15

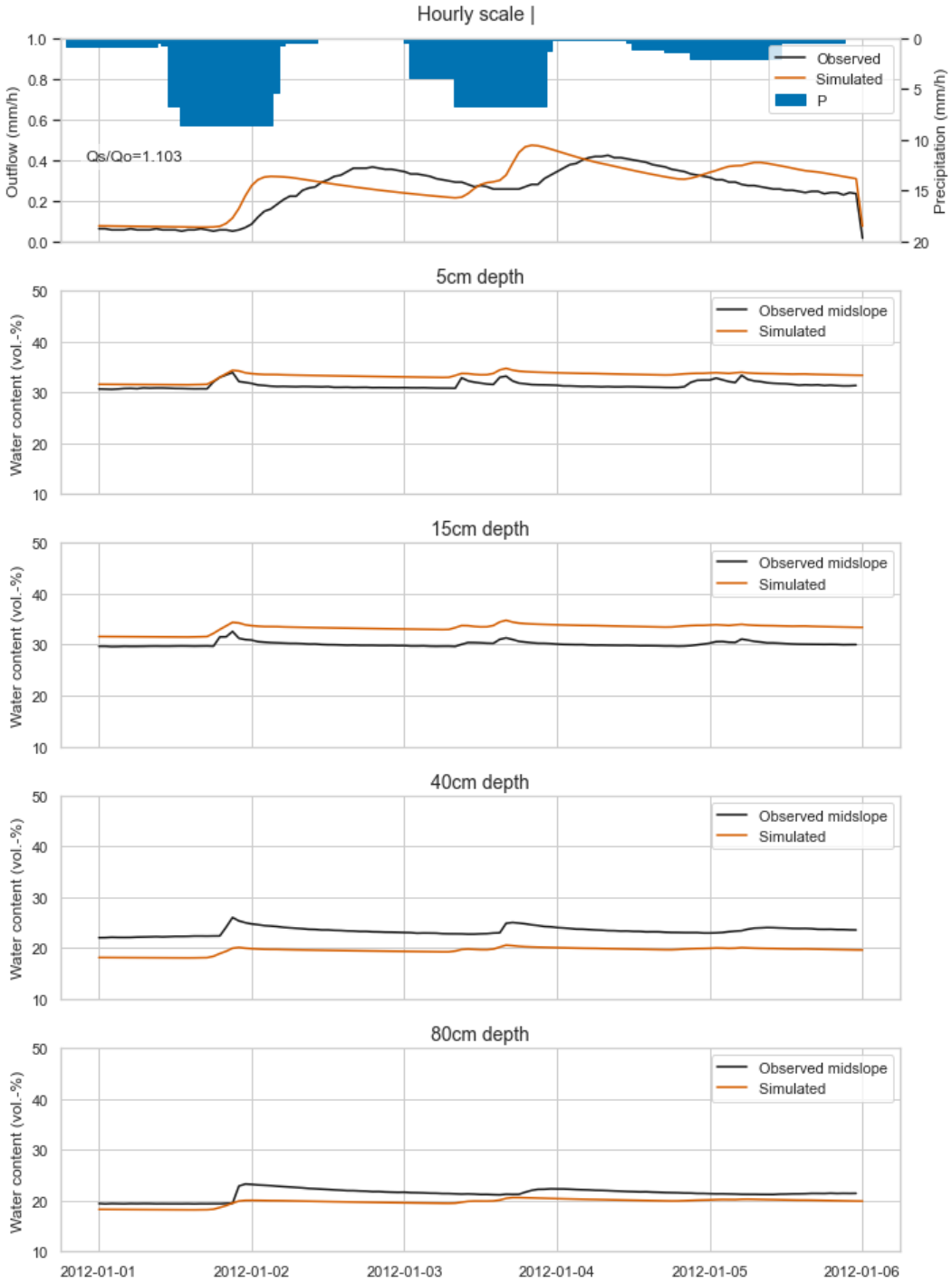

Figure 74: Simulation results for initial parameter values for drainage event in January 2012 at hourly scale.

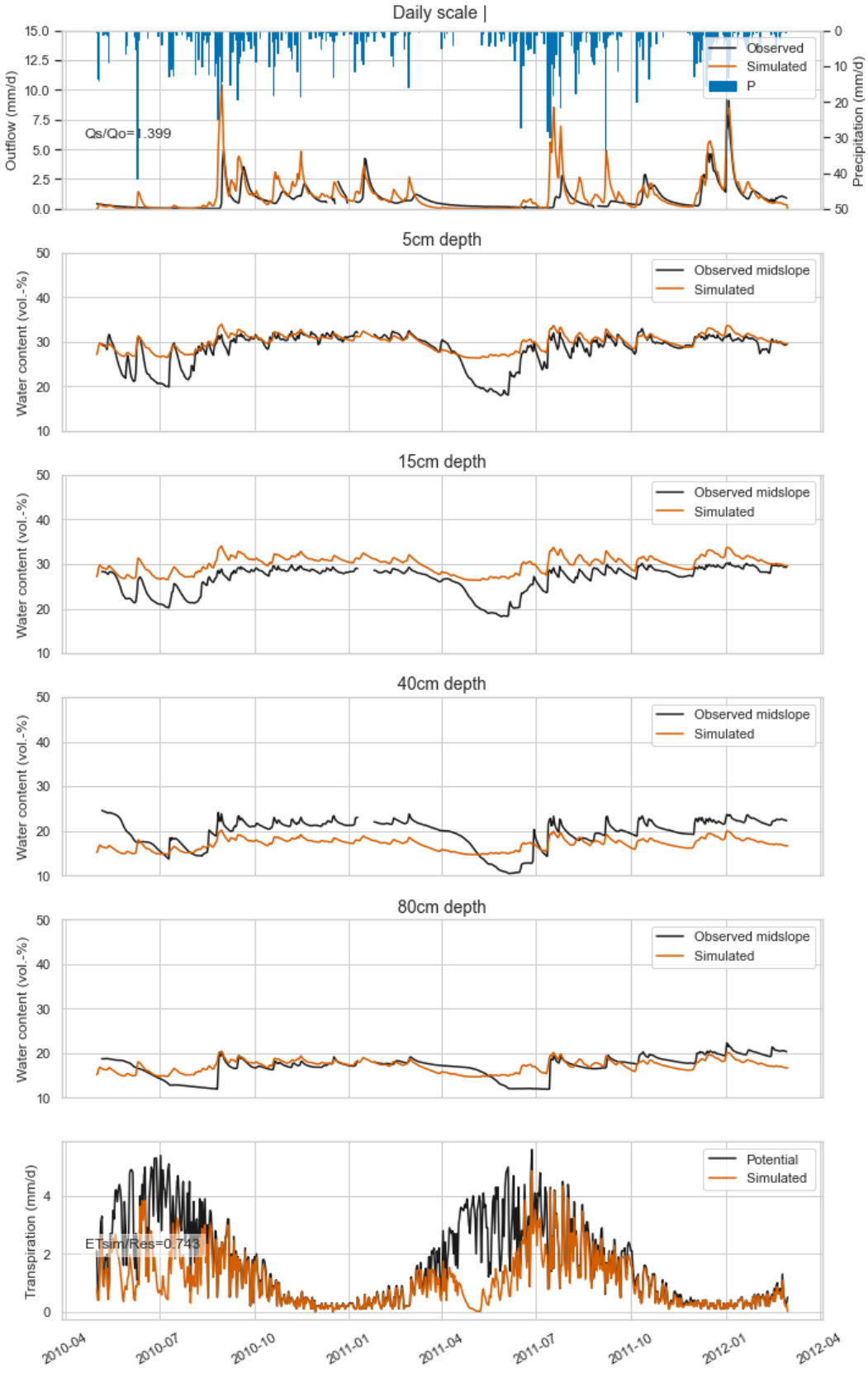

Figure 75: Simulation results for initial parameter values for period between May 2010 and March 2012 at daily scale.

C.6.3. Effect of parameter changing b on root water uptake and water flow

Changing b results in a difference in the location of root water uptake, which is compensated for by water flow. For example, increasing b from 10 to 20 results in a higher capillary rise (Figure 76 and Figure 77).

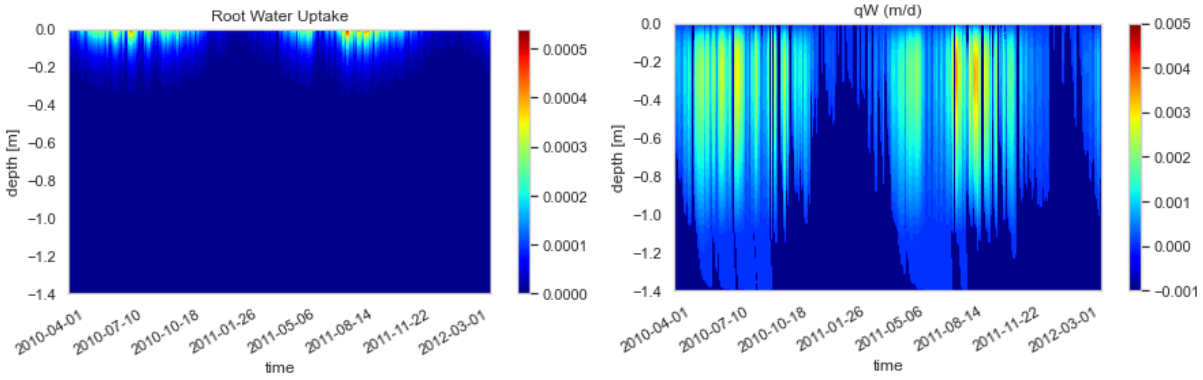

Figure 76: Root water uptake (left) and water flow[6] (right) for b = 10.

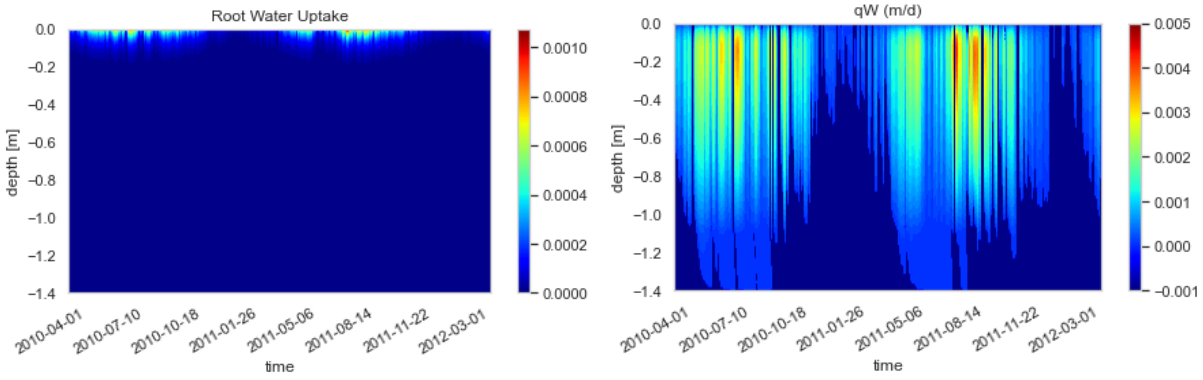

Figure 77: Root water uptake (left) and water flow with (right) for b = 20.

C.6.4. Process of obtaining the final parameter values

Parameters were adjusted according to their function. Changing θ_r and θ_s of a soil layer influences the minimum and maximum between which the water content can vary. Furthermore, decreasing this range results in faster outflow from a layer because the same inflow of water leads to a higher effective saturation and consequently hydraulic conductivity.

The parameter α approximates the inverse of the height of the capillary rise (Equation 3) or the AEV. Decreasing this parameter results in a higher water content in a layer and vice versa. On the contrary, the parameter n controls the shape of SWRC at suctions higher than the AEV. A high value is related to soil with a narrow pore size distribution which results in a rapid change in effective saturation and consequently hydraulic conductivity over a relatively narrow suction range. In other words, increasing n leads to more flashy outflow behaviour and a lower saturation at hydrostatic equilibrium in a layer. Furthermore, increasing k_s increases the flow from a layer and decreases its water content and vice versa.

[6] Upward flow is positive. Negative flow magnitudes not shown here as these are larger than upward flow rates.

Moreover, changing a parameter of a layer also influences the water contents in the other layers depending on the difference between the layers. For example, increasing n of the CL led to an increase of water content in the layers above because of CBE. This also leads to parameter equifinality, as multiple parameters can have the same effect.

The process of adjusting the parameters started with reducing θ_r for the SS and TS to match the measured lowest water contents in July 2011. This led to a reduction in water content of both layers.

Secondly, the measured outflows are the result of not only vertical flow through the soil layer but also lateral flow through the test field. This leads to additional time lag and peak dampening. Therefore, k_s of the CL was decreased to mimic those effects. Furthermore, to increase the time between the start and the peak of an outflow wave n and α were increased. In this way more moisture needs accumulate in the CL for the hydraulic conductivity to become large enough. Additionally, θ_s was decreased to increase the magnitude of the outflow peak. As a consequence of increasing α and n of the CL the water content in the layers above rose, most likely to a capillary break effect between the SS and the CL. To decrease the water contents to the observed level θ_s was slightly decreased and n was slightly increased of both the SS and TS. The increase in n also led to a more flashy behaviour in the water contents which is similar to the observations. The result of these parameter adjustments was a better simulated outflow and water content behaviour.

Thirdly, during adjusting the transpiration parameters it appeared that changing h_1, h_2 and b had no effect on water contents or transpiration rates. As the water content data show that the soil was never close to saturation (θ_s) parameters h_1 and h_2 are indeed irrelevant. Concerning the root density distribution parameter b, changing its value has an effect on where root water uptake takes place but doesn't change the resulting water content because the model compensates a different location of root water uptake by water flow. For example, a value of b of 20 shifts the root water uptake to higher in the soil, but this is compensated for by capillary rise (Appendix C.6.3).

The parameters h_3 and h_4 were not changed as well, although they have significant impact on the models' behaviour. Their initial values resulted in a good fit already. There is a balance between the drying pattern at 40 and 80 cm depth which are approximately equally under- and overestimated respectively. The soil at 5 and 15 cm dries out slightly more than simulated, but the rate of decrease decreases at the same time for both simulated and observed values. Finally, the sum of simulated transpiration was equal to 1.06 time the sum of residual precipitation between March 2011 and 2012, which was considered sufficient seeing the uncertainty in this estimate.

D. Results

D.1. Calibration

D.1.1. Result winter drainage event

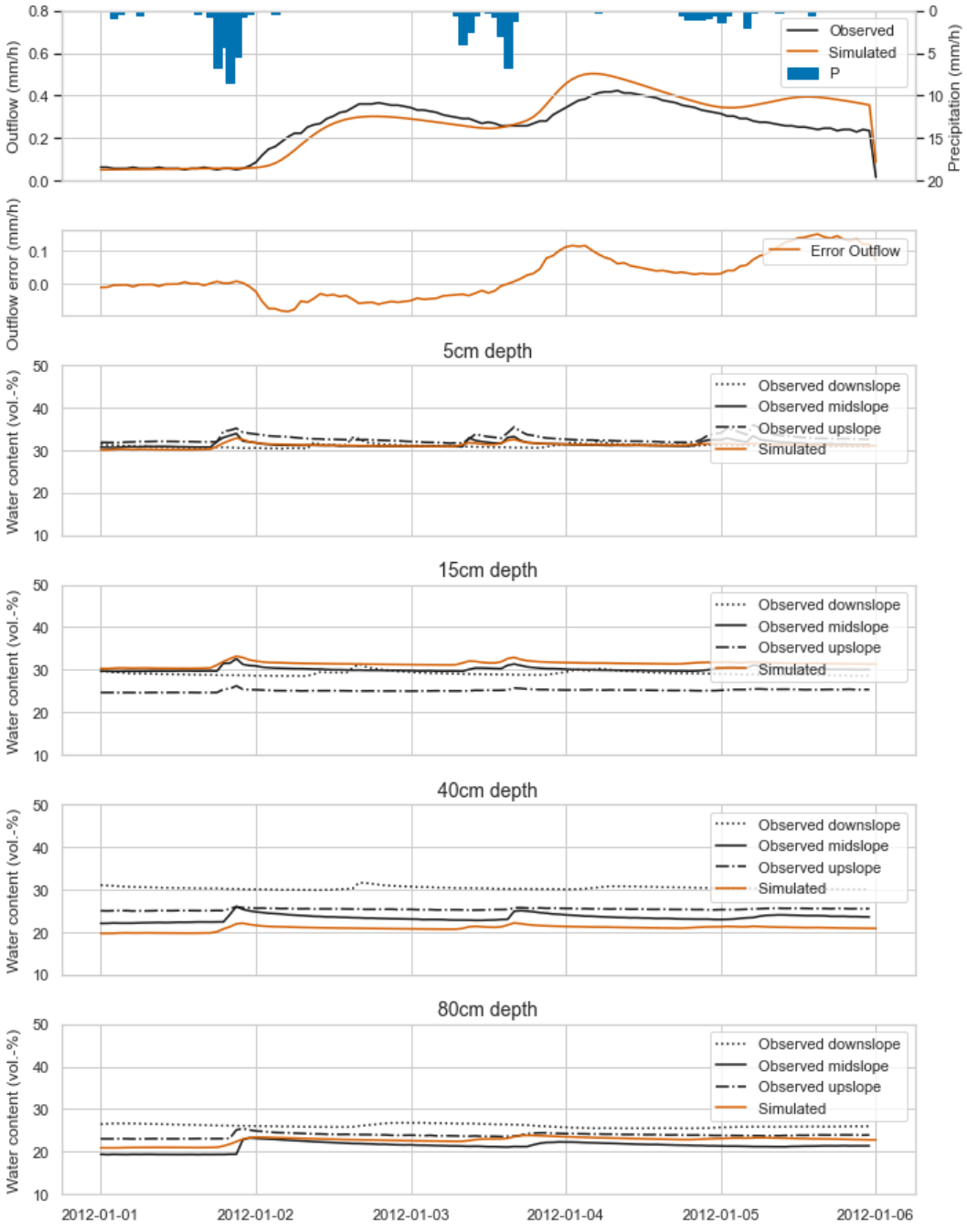

Figure 78: Calibration result of winter drainage event.

D.1.2. Precipitation calibration and testing period

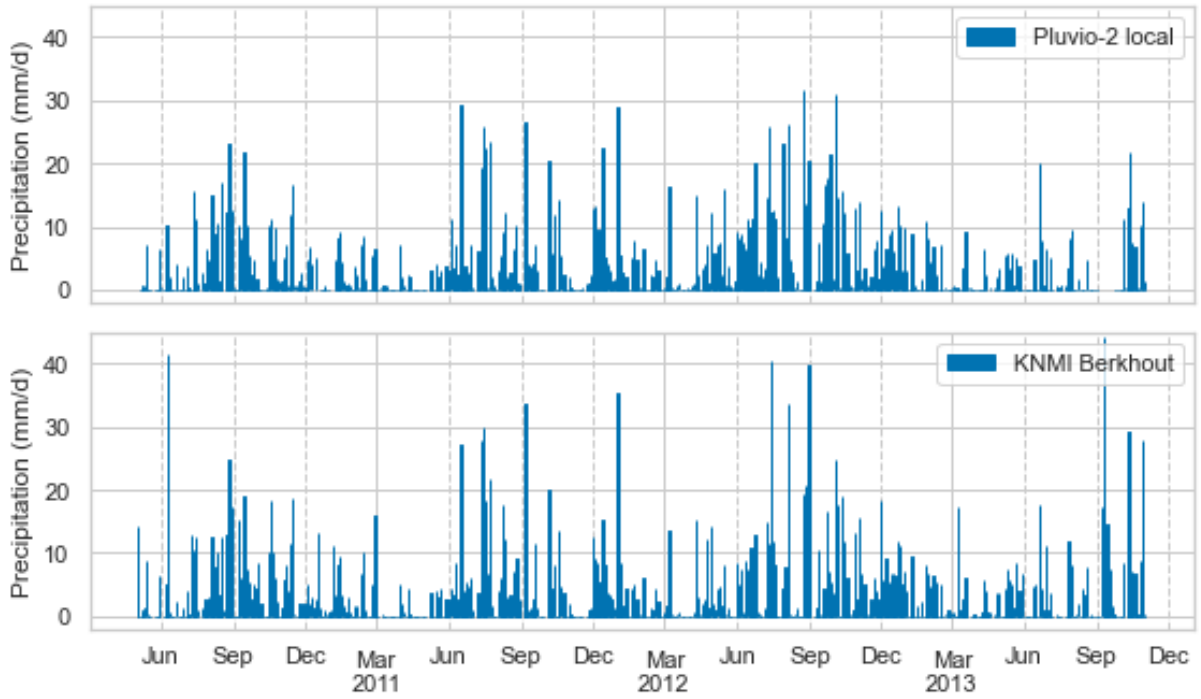

Figure 79: Precipitation of calibration and testing period for Pluvio-2 and KNMI Berkhout stations.

D.2. Yearly water balance

Table 15: Yearly water balance

Year	Precipitation (mm)	Error in simulated ΔS and ET (mm, % of P)		Storage change (mm, % of P)		Outflow CB (mm, % of P)		Outflow CL (mm, % of P)		Evapo-transpiration (mm, % of P)	
2010	689	13	1.8%	-10	-1.4%	20	2.9%	239	34.7%	429	62.3%
2011	852	-5	-0.6%	9	1.0%	75	8.8%	252	29.5%	525	61.6%
2012	981	-56	-5.7%	11	1.1%	162	16.5%	318	32.4%	540	55.1%
2013	887	113	12.7%	57	6.4%	35	4.0%	249	28.0%	437	49.2%
2014	791	-28	-3.6%	-58	-7.3%	73	9.2%	281	35.5%	531	67.1%
2015	966	89	9.2%	18	1.8%	75	7.8%	278	28.8%	500	51.7%
2016	667	0	0.0%	-33	-4.9%	20	3.1%	167	25.0%	517	77.4%
2017	1095	44	4.0%	25	2.2%	93	8.5%	421	38.4%	515	47.0%
2018	612	56	9.1%	-21	-3.4%	16	2.7%	138	22.5%	422	69.0%
2019	975	58	6.0%	-4	-0.4%	81	8.3%	368	37.7%	474	48.6%
2020	968	-16	-1.7%	84	8.6%	63	6.5%	326	33.7%	512	52.9%
2021	803	-60	-7.4%	-67	-8.4%	47	5.9%	322	40.1%	568	70.8%
2022	771	-40	-5.1%	11	1.4%	52	6.7%	294	38.1%	449	58.3%
Mean	**851**	**13**	**1%**	**2**	**0%**	**63**	**7%**	**281**	**33%**	**494**	**59%**

D.3. Seasonal water balance

The seasonal water balance is visualised in Figure 17. The exact values can be found in Table 16.

Table 16: Seasonal water balance

Season	Precipitation (mm)	Error simulated outflow (mm)	Storage change (mm)	Outflow CB (mm)	Outflow CL (mm)	Evapo-Transpiration (mm)
2009 autumn	137.3	-23.6	86.5	4.0	54.5	16.1
2010 winter	220.4		5.0			27.0
2010 spring	109.1		-103.1			180.8
2010 summer	278.2	-6.1	96.4	1.8	8.1	180.5
2010 autumn	222.2	23.7	-5.0	9.7	109.6	86.0
2011 winter	149.6	17.7	14.8	7.5	84.0	25.9
2011 spring	41.5	-22.8	-106.6	1.3	37.5	136.7
2011 summer	351.6	0.8	93.4	7.0	34.9	215.5
2011 autumn	149.1	3.0	-9.5	6.5	61.9	95.2
2012 winter	236.3	22.1	-7.0	59.9	113.7	33.0
2012 spring	120.6	-31.6	-69.1	1.2	41.4	181.3
2012 summer	352.2	-40.5	95.3	4.7	42.1	252.6
2012 autumn	268.1	-19.0	11.0	81.7	114.6	91.2
2013 winter	237.5	28.8	-32.9	74.3	120.1	31.5
2013 spring	114.4	-25.2	-66.3	1.5		164.7
2013 summer	107.2	-11.0	-21.5	2.0		132.6
2013 autumn	368.6	141.7	101.4	14.3		75.0
2014 winter	228.3	11.5	1.8	17.2	165.5	34.2
2014 spring	183.2	-29.5	-23.4	1.6	40.1	196.3
2014 summer	257.7	-29.1	30.2	7.9	41.6	211.1
2014 autumn	140.9	7.3	-0.5	1.4	35.4	99.4
2015 winter	266.2	19.2	12.5	59.5	146.3	34.4
2015 spring	135.4		-90.6			185.7
2015 summer	264.0		82.9			178.4
2015 autumn	306.0	54.7	23.4	31.1	105.7	88.5
2016 winter	205.3	56.7	-24.9	34.3	110.3	35.4
2016 spring	181.5	-12.5	-77.3	9.2	51.8	197.8
2016 summer	214.4	-4.6	-19.1	0.5	4.3	231.8
2016 autumn	204.7	23.6	83.8	1.3	21.6	73.8
2017 winter	150.0	12.0	19.7	8.3	81.0	31.4
2017 spring	97.9	-31.3	-117.2	10.3	60.1	177.2
2017 summer	258.3	-3.0	71.1	0.4	2.7	186.5
2017 autumn	407.0	106.3	53.2	29.4	134.0	87.5
2018 winter	236.6	3.9	-35.9	39.8	195.8	35.5
2018 spring	196.7	-63.6	-56.0	23.7	88.2	207.0
2018 summer	144.7	-5.7	33.1	0.7	5.1	110.3
2018 autumn	130.4	5.2	24.6	0.1	0.8	102.1

Season	Precipitation (mm)	Error simulated outflow (mm)	Storage change (mm)	Outflow CB (mm)	Outflow CL (mm)	Evapotranspiration (mm)
2019 winter	185.7	72.7	2.4	4.2	65.9	37.6
2019 spring	147.6	-16.2	-81.1	11.4	65.9	171.1
2019 summer	220.9	-3.0	4.1	0.3	2.9	217.2
2019 autumn	406.3	82.4	108.6	22.4	117.3	74.1
2020 winter	279.4	0.5	12.4	50.0	188.8	32.2
2020 spring	68.6	-21.8	-123.5	8.4	59.1	148.8
2020 summer	250.0	-2.5	33.6	0.3	2.3	215.3
2020 autumn	259.2	-2.6	77.2	9.4	89.0	88.3
2021 winter	268.6	18.5	-19.0	50.5	181.3	35.5
2021 spring	190.3	-32.3	-10.8	2.6	56.4	178.2
2021 summer	219.6	-33.9	-40.5	2.0	33.3	262.5
2021 autumn	242.7	9.5	97.7	4.0	60.6	77.2
2022 winter	236.0	-8.0	-20.5	39.3	186.5	34.5
2022 spring	109.4	-24.7	-95.6	1.6	23.9	191.0

D.4. Correlation CBS flow to other water balance components per season

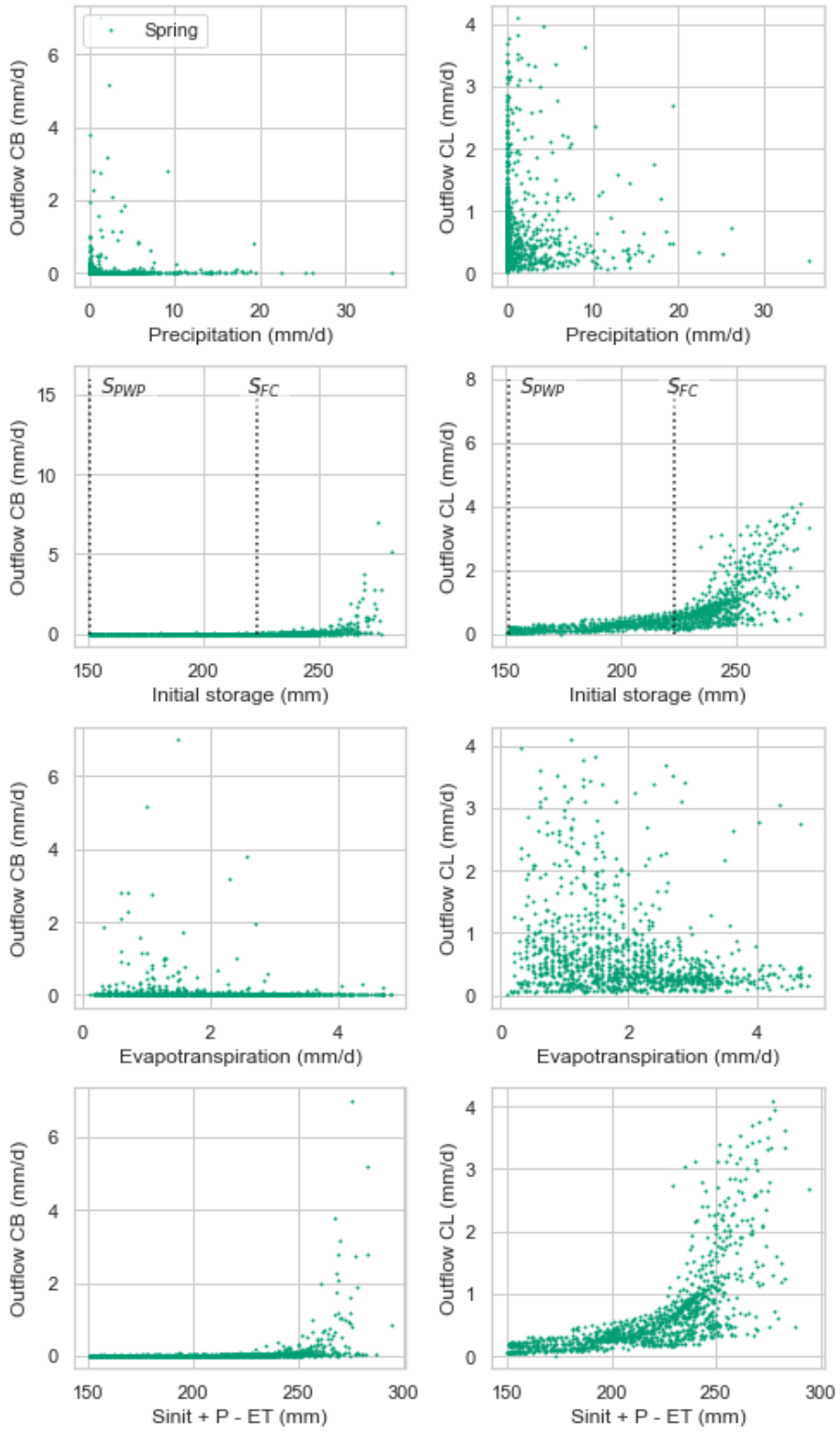

Figure 80: Correlations between daily CL and CB outflows and storage, precipitation, evapotranspiration and their sum on the same day for days in the spring season.

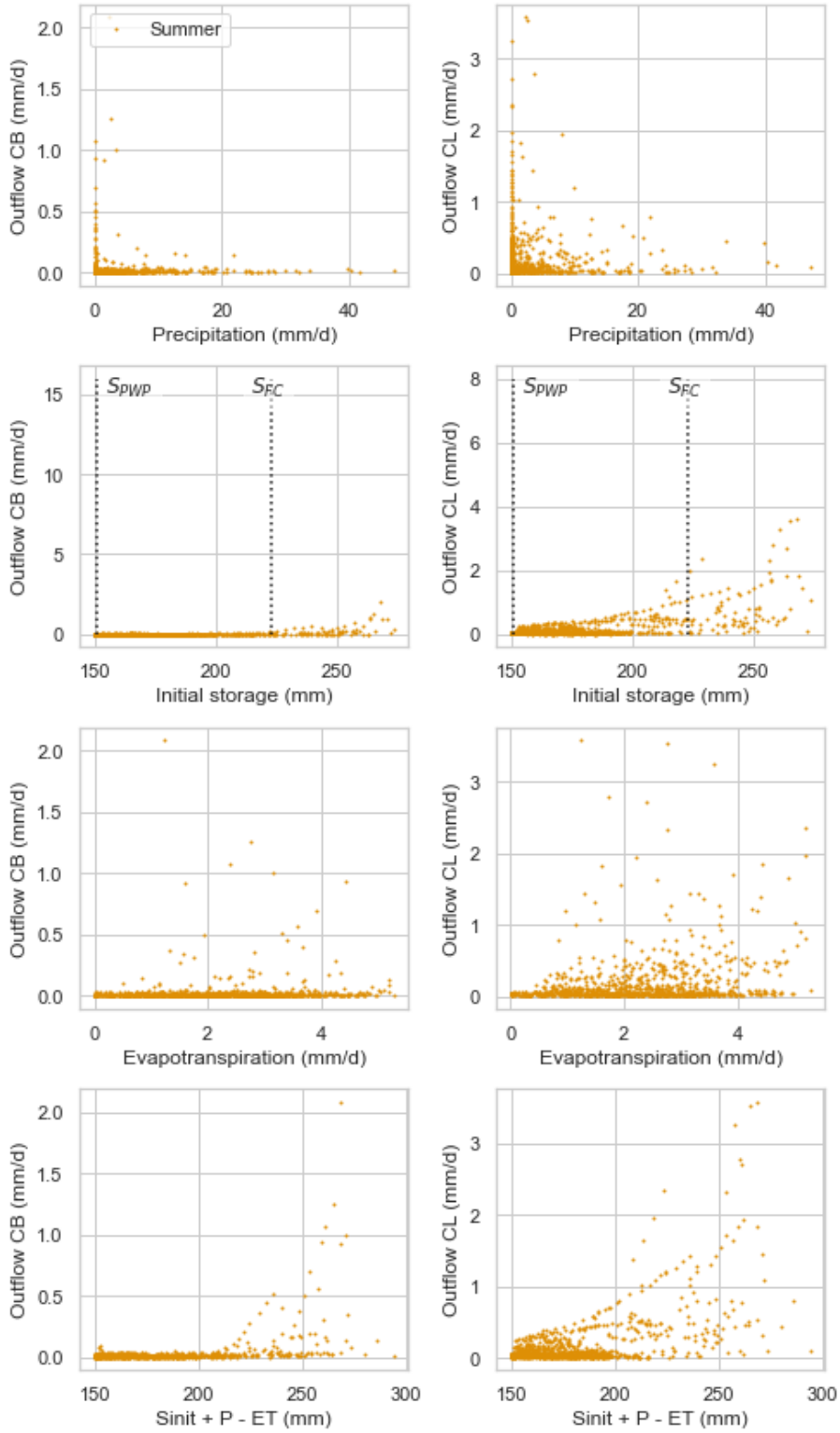

Figure 81: Correlations between daily CL and CB outflows and storage, precipitation, evapotranspiration and their sum on the same day for days in the summer season.

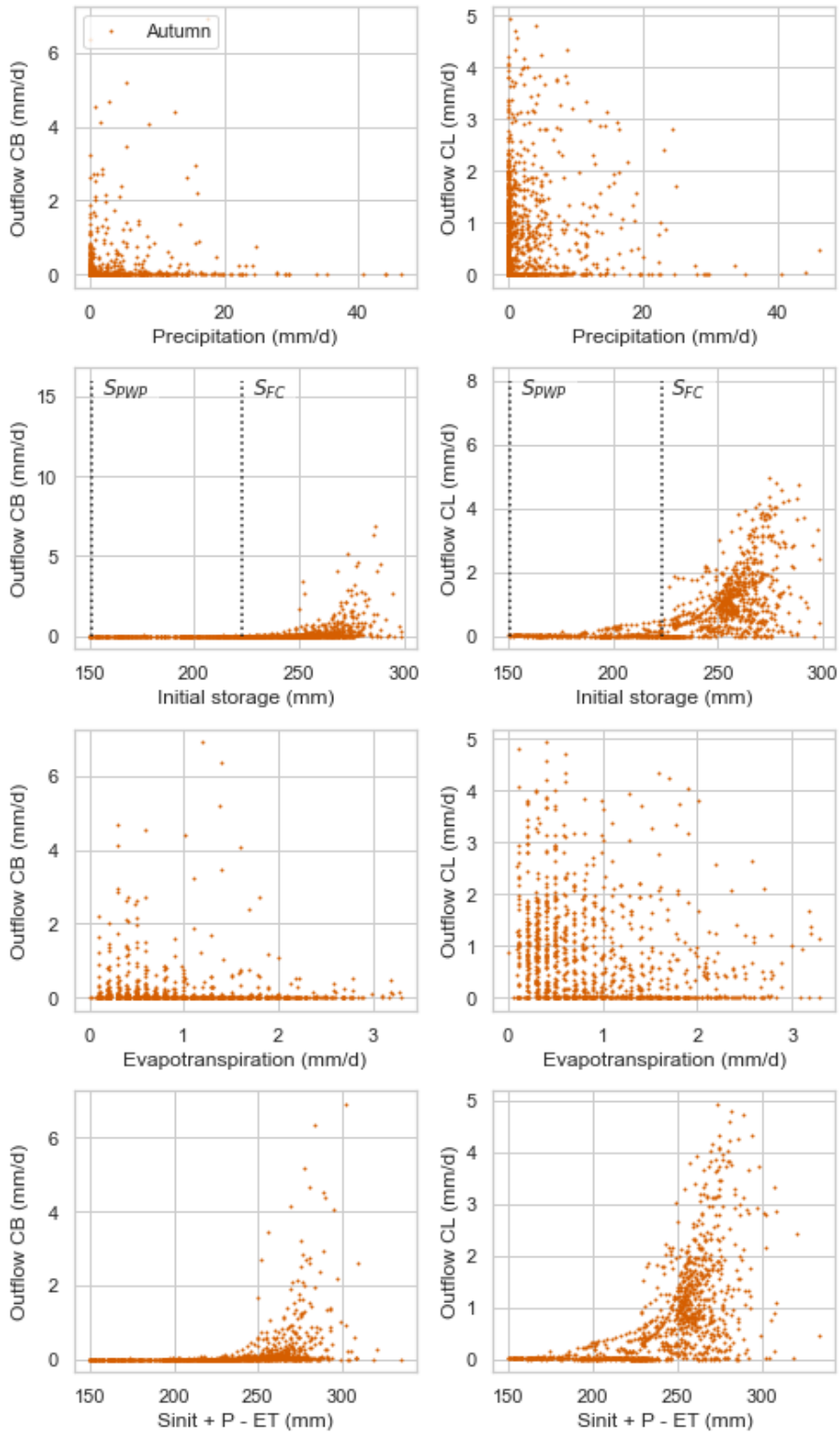

Figure 82: Correlations between daily CL and CB outflows and storage, precipitation, evapotranspiration and their sum on the same day for days in the autumn season.

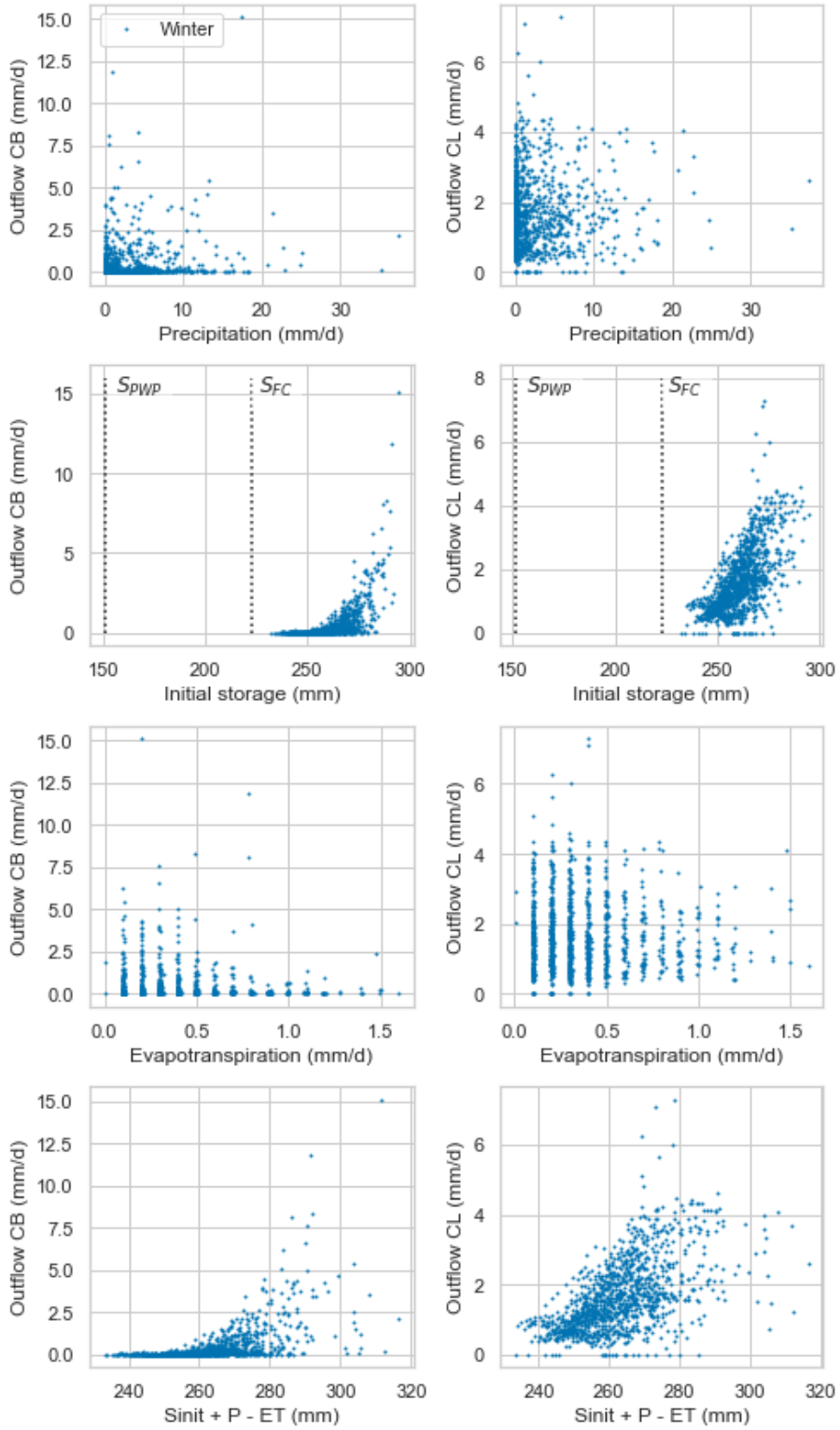

Figure 83: Correlations between daily CL and CB outflows and storage, precipitation, evapotranspiration and their sum on the same day for days in the winter season.

D.5. CBS response to intense precipitation in summer

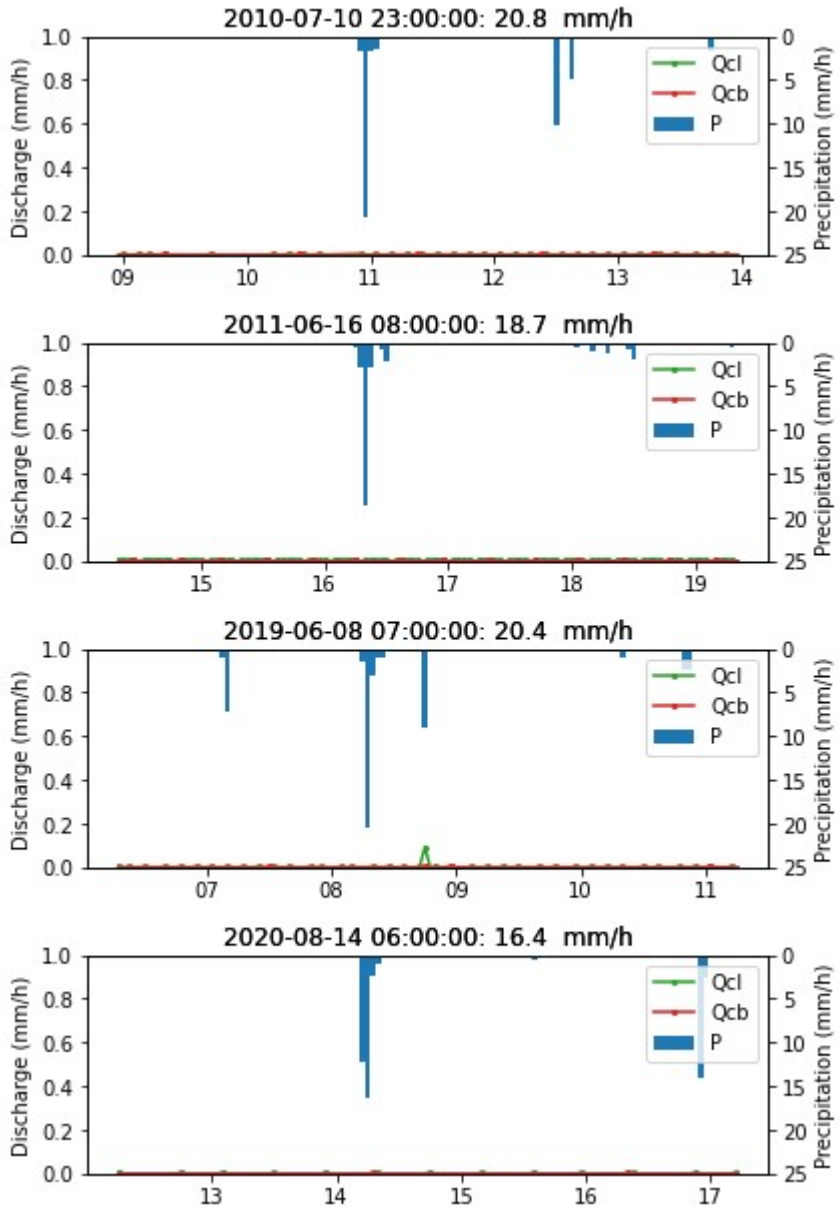

Figure 84: CBS response to intense precipitation events during summer. Precipitation data is local data from the Pluvio-2 measurements.